Mesostructural Characterization and Probabilistic Modeling of the Design Limit States of Parallel Strand Lumber

MESOSTRUCTURAL CHARACTERIZATION AND PROBABILISTIC MODELING OF THE DESIGN LIMIT STATES OF PARALLEL STRAND LUMBER

A Dissertation Presented

by

ALIREZA AMINI

Submitted to the Graduate School of the
University of Massachusetts Amherst in partial fulfillment
of the requirements for the degree of

DOCTOR OF PHILOSOPHY

February 2013

Civil and Environmental Engineering

MESOSTRUCTURAL CHARACTERIZATION AND PROBABILISTIC MODELING OF THE DESIGN LIMIT STATES OF PARALLEL STRAND LUMBER

A Dissertation Presented

by

ALIREZA AMINI

Approved as to style and content by:

Sanjay R. Arwade, Chair

Peggi L. Clouston, Member

Thomas J. Lardner, Member

Richard N. Palmer, Department Chair
Civil and Environmental Engineering

From all mysteries, nothing but an "a" was discovered, and whatever else was stated was to explain that "a", and that "a" was of course not understood.
Shams of Tabriz

ACKNOWLEDGMENTS

I would like to thank warmly my advisors, Dr. Sanjay Arwade and Dr. Peggi Clouston for their guidance throughout this project.

Thanks also go to Dr. Thomas Lardner, my examining committee member, for reviewing my work, Saranthip Rattanaserikiat for her significant contribution to this project and Mohammadreza Moradi for his kind helps.

Finally, I wish to appreciate the firm support, boundless kindness and sympathizing care of my family.

ABSTRACT

MESOSTRUCTURAL CHARACTERIZATION AND PROBABILISTIC MODELING OF THE DESIGN LIMIT STATES OF PARALLEL STRAND LUMBER

FEBRUARY 2013

ALIREZA AMINI

B.Sc., UNIVERSITY OF TEHRAN, IRAN

M.Sc., SHARIF UNIVERSITY OF TECHNOLOGY, TEHRAN, IRAN

Ph.D., UNIVERSITY OF MASSACHUSETTS AMHERST

Directed by: Professor Sanjay R. Arwade

Over recent decades, the public tendency toward using the structural composite lumber (SCL), a common composite of wood made of wood strands or veneers glued and compressed together, as structural members (especially the main load bearing members such as beams and columns) has risen considerably. In contrast to the fast-paced market growth of these products, development is slow. The experimental development is gradual and time-consuming and the computational development is even slower. The objective of this project is to introduce appropriate numerical models for limit state analysis of a certain type of SCL material called PSL.

Parallel strand lumber (PSL), has mesostructures characterized by the presence of voids that renders the mesostructure highly heterogeneous. In addition to material phase aberrations such as grain angle variations and defects, void heterogeneities play an important role in determining the failure modes and strength of PSL. In this study,

virtual void structures were defined to form part of the input to finite element analysis of PSL for the purpose of investigating the sensitivity of strength to the void structure. Assuming the wood phase to be homogeneous and orthotropic, the following 2D and 3D characteristics of voids were investigated: volume fraction, volume, alignment and moments of inertia of voids, as well as second moment properties, lineal path function and chord length functions of the two phase mesostructure. In addition, a method was developed to generate virtual voids in order to simulate PSL and investigate the possible effects of the void distribution on material strength.

An experimental program along with a statistical survey was conducted to quantify the mentioned characteristics of the voids in two 133 mm * 133 mm * 610 mm 2.0 E Eastern Species PSL billets. As expected, most of the voids lie on the longitudinal direction of the specimen and have approximately an ellipsoidal shape. Based on this shape data, the characteristics of the ellipsoids which best fit the voids were calculated. Using the statistical data of the fitted ellipsoids, a random field of virtual ellipsoid shaped voids to simulate the mesostructure of PSL was generated.

In this study, the simulation of PSL material is based on two simplifying assumptions: 1) The wood phase is continuum, homogeneous and orthotropic. While in reality, the wood phase consists of glued wood strands that are heterogeneous due to their mechanical variability and only roughly orthotropic on a macro scale as a result of the varying fiber angle; 2) Voids are the mere source of uncertainty. The linear elastic analysis of carefully defined (in mesostructural aspect) PSL models can be the first step of mechanical study of the material. The effective modulus of elasticity of material in presence of voids and the distribution of conventional, principal and effective stresses considering the effect of volume fraction and shape of the voids are the target of this preliminary study. Linear elastic uniaxial analyses showed good mechanical consistency between the models including actual void shapes and the

models including ellipsoidal void representations. Also, they showed that the stress mutliaxiality at the tip of the voids is negligible.

The study of mechanics of PSL is incomplete unless the question of material anisotropy is taken into consideration. PSL is brittle in tension and ductile in compression. The material heterogeneity increases the complexity of the problem by affecting the stress distribution in the member. A detailed nonlinear approach has been proposed in order to investigate the mechanical behavior of PSL structural members under different uniaxial loading scenarios. This approach introduces proper constitutive models for the wood phase along with good void generation techniques. In other words, this approach suggests what models should be used for the continuum-assumed wood phase to simulate its brittle behavior in tension and ductile behavior in compression; and moreover, tests the applicability and accuracy of ellipsoidal void representation. The models are calibrated using the results of experiments on PSL material.

Because of the brittle behavior, all wood products show significant mechanical dependency to the member's size under tensile loading. Once good constitutive model and mesostructural simulation is found for tensile loading, it is easy to make and analyze PSL models with different sizes and investigate the effect of size on mechanical behavior. The simulation results have been compared to the available results of a previously done experimental study.

TABLE OF CONTENTS

LIST OF TABLES

Table **Page**

LIST OF FIGURES

Figure **Page**

CHAPTER 1

INTRODUCTION

1.1 Problem statement

Structural composite lumber (SCL) has become more and more popular in light-frame construction for the past decades as a reliable replacement for the traditional solid-sawn lumber (SSL). Under axial loading and bending, SCL is stronger than the conventional wood; however, this may not be true for shear strength [30]. As a result of the reduction and dispersion of wood knots and defects in the process of manufacturing, SCL has low uncertainties associated with material properties. The other important advantage of SCL is that the desired length and width of SCL can be economically produced regardless of the size of the trees available. Also, because many species can be used almost interchangeably, more timber harvested from a single stand can be utilized. The other advantages of SCL are its light weight, durability and dimensional stability (in comparison to other building materials).

Two commercially available types of SCL are laminated veneer lumber (LVL) and parallel strand lumber (PSL), both composed of thin laminations of wood compacted and glued together by phenol-resorcinol and phenol-formaldehyde based adhesives. The most common wood species used in SCL are Douglas-Fir, Southern Pine, Yellow Poplar and Aspen [33]. Although the PSL strands are aligned mainly in the longitudinal direction, they are more randomly oriented than the LVL veneers. Therefore, the probabilistic study of PSL seems to be more sophisticated. The mesostructure of PSL consists of wood strands, adhesive and the voids remaining after compaction. This

study will focus on the mesostructural characterization and probabilistic constitutive modeling of PSL.

The market for SCL products is large and growing. North American production of LVL alone is predicted to be more than 3 million cubic meters in 2015, up from 1.5 million cubic meters in 2000, an increase of 100% [3]. Just between 2003 and 2006, the consumption of engineered lumber products increased by 10%[5]. The same report identified substantial rise in consumption of wood products in 2006 by gaining market share from competitive non-wood products. In this gain, the share of engineered lumbers is more than the share of structural panels [5].

In spite of the significant increase in the production and demand of PSL, the development of computational tools for the analysis and design of PSL members has advanced very slowly. Research concerning the structural limit states of SCL is necessary in order to develop accurate computational tools for predicting the strength of engineered structures built of PSL. The commercialization of these tools to predict and simulate the response of PSL members can help to ease acceptance of PSL products in demanding structural applications, foster development of new wood composite products and provide economic and environmental benefits from increased structural and manufacturing efficiency. To this end, a comprehensive statistical characterization of the structural properties of PSL is needed. The mesostructural modeling techniques presented in this dissertation will represent a significant advance in the ability to predict the strength of PSL members based on fundamental mechanics.

1.2 Background and motivation

To the best of author's knowledge, only a handful of studies have concentrated on finite element modeling of the constitutive properties of PSL. Triche and Hunt [48] developed a linear elastic finite element model capable of predicting the tensile strength and stiffness of parallel aligned wood strand composite a simplified version of PSL.

They used multi-axial failure criteria, including maximum stress theory and Tsai-Wu theory, but did not attempt to predict compressive, bending or any multi-axial stress states. In 1998, a study was carried out by Wang and Lam [50] in which a 3D nonlinear stochastic finite element model was used to estimate the probabilistic distribution of tensile strength of an academic wood composite. The model was verified through comparison with experimental data and reported excellent agreement. Later, Clouston and Lam developed a progressive computational model which, for the first time, provided a methodology to analyze multi-axial stress states of small coupons of PSL [18, 22]. The constitutive model was based on nonlinear plasticity theory defined by four basic constitutive regimes: elastic, elastoplastic, post-failure brittle, or post-failure ductile with associative flow and isotropic hardening. Also, orthotropic strength and stiffness parameters were random variables facilitating stochastic and probabilistic analysis of the material. The model successfully predicted cumulative probability distributions and simulated constitutive curves for small coupons of PSL in static compression, tension and bending.

To be reliable, the stochastic computational models of SCL, PSL in particular, should present a probabilistic model for the geometry of the material's mesostructure. AS mentioned before, two dominant features of the PSL mesostructure are wood strands and the voids remaining after compaction and adhesion. No matter whether the analyst tries to explicitly represent the mesostructure in the computational model or include it in continuum finite elements in an averaged sense, the statistics of the void phase geometry must be available. There are not many documents in engineering literature about the characterization of PSL mesostructure. Two important studies should be cited here. Ellis et al. [24] studied the macro-porosity of Parallam ®, a structural wood-based product based on PSL technology, by two optical techniques. They used a video camera and a line scan camera to capture the voids of Parallam ®in transmitted light and then analyzed the images. In an-

other work, Sugimori and Lam [45] used X-Ray computer tomography techniques on a 0.16×0.34×1.28m strand-based wood composite specimen and made a database of distribution of size and position of macro voids in 3D space. On the other hand, there are useful documents regarding the measurement and modeling the microstructure of other materials. The following paragraphs include a brief literature review about microstructural characterization of different materials.

The first step of charcterization is micro/meso-structural measurement. Acoustic microscopy is a popular method to measure the microstructure of materials. This method has been addressed by Knauss et al. [36] for 3D measurement of short fatigue cracks in Al-Li alloys and also by Claire et al. [17] in order to study the local properties of wood. To evaluate the average porosity, pore radius and internal surface area of macroporous silicon structure, the impedance of pores was measured by Chaudhuri et al. [14]. They believe that this method can be extended to meso and microporous silicon if they have a regular columnar structure. Ghadbeigi et al. [26] studied the evolution of local plastic deformation in a dual-phase (DP) steel using Digital Image Correlation (DIC) and in-situ tensile testing inside a scanning electron microscope. They think that this procedure is very applicable for the measurement of local strain distributions. Serial sectioning is another interesting way of microstructure measurement in which the material structure is scanned and then measured section by section (or layer by layer). Matzke and Warren [40] used serial sectioning to follow the crack growth as a function of load in ThO2. Bystrzycki and Perzetakiewicz [13] reconstructed the 3D shapes of annealing twins in FCC metals by serial sectioning. Ye et al. [55] introduced an approach for characterization of the microstructure of cement-based materials by taking environment scanning electron microscopy (ESEM) images and applying a serial sectioning algorithm with an overlapping criterion. Their model provided a promising description of the evolution of cement paste microstructure including pores. Also, Garboczi [25] provided useful information on the geometry of

concrete aggregates measuring the shape of a broad range of actual aggregates and cement particles by X-ray computed tomography.

Modeling the microstructure based on the measurements is the other relevant characterization step that has attracted researchers for years. Graham et al. [28] proposed that the local constitutive properties in random composite microstructure be approximated by applying a moving window micromechanics technique which provides the basis for establishing the probability density function and power spectral density of the randomly varying constitutive properties. In one of the first attempts to model SCL, a nonlinear stochastic model has been formulated by Clouston and Lam [18] to simulate the stress-strain behavior of strand-based wood composites based on the constitutive properties of wood strands which is characterized within the framework of rate independent theory of orthotropic plasticity. Later, Clouston [19] added the length dimension to the model to allow the investigation of spatial variability. Bejo and Lang [10] proposed a probability based model to study the effect of the change in elastic properties on the performance of the product. They also modeled the orthotropic behavior of wood constituents due to their position in composite by theoretical/empirical equations. A model for spatial variation of the elastic modulus of PSL that is based on bending experiments has been described by Arwade et al. [6]. This work also includes a stochastic computational model that incorporates orthotropic elasticity and uncertainty in strand geometry and material properties. The same authors also investigated the variability of compressive strength of PSL by conducting the measurement of compressive strength on specimens of varying size with nominal identical mesostructure [7]. They also developed a computational model including the strand length, grain angle, elastic constants and parameters of Tsai-Hill failure surface. An experimental effort for SCL material characterization was performed by Janowiak et al. [33] applying the five point bending test and torsional stiffness measurement test evaluation methodologies. They also focused on axial test

under tensile and compressive loading condition for determination of longitudinal and transverse elastic moduli combined with in-plane Poisson's ratio.

Although references on microstructural modeling of SCL are limited, one can find considerable number of documents about modeling of the microstructure of many other materials in the literature. A famous numerical model for concrete using spherical aggregates with volumes matching the volumes of actual aggregates has been proposed by Bentz et al [11]. In a comparable work, Bullard and Garboczi [12] proposed a microstructure model of cement hydration which is called Virtual Cement and Concrete Testing Laboratory (VCCTL). The model is able to digitize 3-D cement paste microstructures assuming that the shape of the particles is spherical. This work was utilized by Jennings et al. [34] to document the influence of time and other external factors on porosity and other microstructural changes of cement paste. They investigated the permeability of the cement paste as a function of porosity and used models of hydration to find out that the weight loss as a function of relative humidity affects the size distribution of pores. Gonella et al. [27] introduced a wave propagation simulation methodology based on Mindlin's microelastic continuum theory [41] to study the effect of microstructure on wave propagation modes. A comparative study between the effect of uniform microstructure and pore clusters on elastic properties and fracture toughness of porous materials has been conducted by Cramer and Sevostianov [23]. They concluded that elastic properties are insensitive to the pore distribution but the fracture toughness is highly affected by the position of pores and the cluster shape. They randomly generated the microstructure of a porous material using the 2D version of molecular dynamics (MD) algorithm [47] and compared the results with an experimental study on aluminum sheets.

Asphalt as a heterogeneous and porous material has been under a wide investigation. Sadd et al. [43] used the finite element method to simulate the micromechanical response of the aggregate/binder system. The inter-particle load transfer was simu-

lated by a FE network including a 2D frame type finite element. The simulation was done utilizing the damage model proposed by Ishikawa [32] and the displacements were compared to the experimental results obtained by video imaging. Another study on hot mix asphalt (HMA) has been done by Tashman et al. [46] applying the advances in imaging technology to the characterization of HMA microstructure including aggregate orientation distribution and shape properties, permeability and 3D microstructure reconstruction. They used the non-destructive X-Ray CT system and image analysis techniques to separate the aggregates and quantify the distributions. Weib et al. [51] analyzed the deformation of crystalline structures by means of scanning electron microscopy as well as local orientation analysis using back scatter diffraction. This data can be used to describe the deformation behavior in non-homogeneously deformed crystalline structures.

Focusing on softwood, Qing and Mishnaevsky [42] conducted a computational micromechanical analysis of the influence of moisture, density and microstructure of latewood on its hydroelastic and shrinkage properties. They employed a 3D hexagon-shape hierarchical micromechanical model of softwood. Vasic et al. [49] explored for appropriate and robust models of wood fracture. They think that linear elastic fracture mechanics (LEFM) solutions are asymptotic with true solutions when systems and members are large. While non-linear elastic fracture models such as fictitious crack model, bridge crack model and lattice fracture model are more powerful tools for predicting unconstrained crack initiation, propagation and evolution. Sedighi-Gilani and Navi [44] used a mixed lattice-continuum to consider the heterogeneity and porosity of wood microstructure. The probable crack propagation volume was modeled by defining a 3D lattice which is dimensionally dependent on microstructure of wood and other regions were considered as continuum. Their simulation results matched the experimental results.

In this study, the mesostructure of PSL has been measured based on a serial sectioning experiment done on a PSL billet followed by a computational approach to relate the measurements in each section and modeled by statistical 2D and 3D procedures. All specimens used for the mesostructural characterization studies were machined from 2.0E Eastern Species PSL billets manufactured by iLevel by Weyerhaueser. All specimens were conditioned to ambient laboratory conditions for one month before testing and reached an equilibrium moisture content of 8-11%.

1.3 Objectives and scope

This project seeks two major goals: (1) introduction of an appropriate method for the statistical investigation and characterization of mesostructure of 2.0 E Eastern Species PSL; and (2) development of a stochastic, computational constitutive model for PSL materials.

A series of analytical studies were conducted on the material. The question of material heterogeneity and anisotropy renders the task complicated. To satisfy the problem of heterogeneity, the mesostructural modeling technique should be stochastic. This model has been introduced in this dissertation. Now that the material heterogeneity can be taken into consideration, one should focus on the problem of anisotropy. Beginning with the compressive loading, the plastic behavior of PSL was the target of our next investigation. The data of the compressive experiments presented in the reference [7] were used to calibrate and validate the results of simulations. Since the data in the mentioned reference just included longitudinal compressive tests, an experimental study was also conducted to gather the data about compressive behavior of PSL in transverse and thru thickness directions.

The other important challenge in the study of mechanics of PSL is the size effect. Because of the brittle behavior, the tensile strength of wood and wood composite members is very dependent on their size [39, 9]. The probabilistic model for generation

of virtual mesostructure of PSL which is introduced in this dissertation paves the way to investigate the problem of size effect more precisely. This model enables us to make an arbitrarily sized finite element model of PSL, calculate the tensile strength and consequently study the effect of size of the specimen on the tensile strength. The experimental data listed in references [38, 21] was a good check-point for this study.

CHAPTER 2

CHARACTERIZATION AND PROBABILISTIC MODELING OF THE MESOSTRUCTURE OF PARALLEL STRAND LUMBER

2.1 Experimental approach

Figure 2.1 shows the mesostructure of PSL which is consisted of wood strands, adhesive and voids. Wood strands make PSL anisotropic. The physical and mechanical variability in strands along with the voids cause the heterogeneity. While earlier observations of the void structure [20, 52, 53] resulted in the development of finite element models of single specimens of composite lumber, no statistical characterization has been developed yet for the void phase. Such a characterization is the primary goal of this study along with the explanation of a suitable probabilistic model for the void phase. In this study we focus on the mesostructure of PSL that has a high degree of heterogeneity and geometric randomness. The applied coordinate system has been shown in Fig.2.1 in which L, T and TT axes represent Longitudinal, Transverse and Thru Thicknes directions of PSL respectively.

Beginning with two 133 x 133 x 610 mm billets of PSL (both cut from the same bigger billet) we used a serial sectioning and scanning approach to reconstruct the three dimensional void structure of the billet. T-TT sections were cut using a band saw with a 6 teeth per inch blade. These sections were then painted white to provide high contrast between the void phase and the solid wood phase. Painting the sections in this way eases identification of the void phases but obscures information regarding the strand geometry. Here we present results only regarding the void phase. Each section of the T-TT plane was scanned to a grayscale image at 100 pixels per inch.

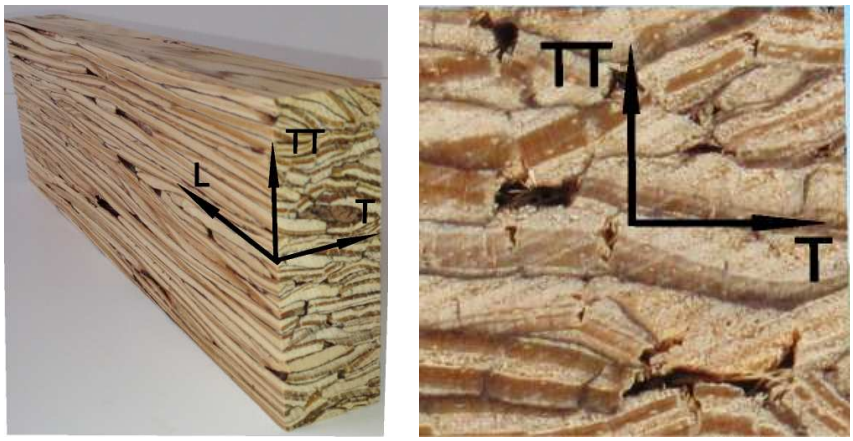

(a) 3D view (b) T-TT section

Figure 2.1. Cross-sectional views of PSL specimen and definition of the member coordinate system. L=Longitudinal, T=Transverse, TT=Thru Thickness

These scans were then digitally stacked in the L direction to reconstruct the full three dimensional void structure of the billet. It was observed that the sections absorbed a small amount of moisture during the painting process, slightly expanding the sample in the T and TT directions by 0.8% in the T direction and 2% in the TT direction. The thickness of each section was measured at the time of cutting, and the sum of the section thicknesses was compared to the original longitudinal length of the specimens to establish the average saw kerf thickness. The average section thickness was found to be 2.75 mm and the average saw kerf thickness was found to be 1.30 mm. Given these measurements, each voxel in the three dimensional mesostructure reconstruction has physical dimensions (T-TT-L) of 0.252 x 0.248 x 4.02 mm. The whole experimental process has been done by research assistant Saranthip Rattanaserikiat.

The process of digitally stacking of the scans and void detection was one the most time consuming parts of the project. The idea was to check if each void voxel neighbors any other void voxel, and if so, consider the neighboring void voxels parts of a long (i.e. more than a voxel long) void. More than 17000 voids were found in the first billet, while the number of voids in the second billet exceeded 20000. Among

these voids, 43% of the voids in the first billet and 49% in the second billet were just one voxel long. Therefore, there are lots of tiny voids in a PSL specimen, but on the other hand, there are considerably large voids that theoretically can influence the mechanical behavior of material. The largest void in the first and second billets have respectively about 44000 and 72000 voxels. The codes written in MATLAB facilitated this data processing procedure.

2.2 Two dimensional Statistical characterization of the void structure

The distinctly anisotropic nature of the void structure is clearly visible in Fig. 2.2. In the T-TT view, voids look rather isotropic and uniformly dispersed; on the contrary, in the L-T and L-TT views, voids are obviously elongated in the L direction. The voids tend to spread correlated to the strand dimension. Therefore, since the wider dimension of the strands is predominantly oriented in T direction, the voids in L-T view apparently have larger size in the T direction than do the voids in L-TT view in TT direction. In other words, the aspect ratio of voids' axes lengths in T-TT view (length of T axis over length of TT axis) is not one, but more (Tab. 2.1). The simplest characterization of the mesostructure is the volume fraction of the void phase, which for the first and second billets was respectively found to be 2.4% and 2.8%. More complete characterizations of the mesostructure would include the voids size distribution and some measure of the void shape. We begin with characterizations of two dimensional cross sections of the mesostructure such as those shown in Fig.2.2.

The basic statistics obtained from the 2D investigation has been presented in Tab. 2.1. The data shows that in both billets, the length aspect ratio in T-TT sections is about 2, while it is about 25 in L-T and L-TT sections. These values match what is observed in Fig.2.2.

Table 2.1. Statistics of the voids properties for three orthogonal sections obtained from 2D investigation

		First Billet			Second Billet		
		T-TT	L-T	L-TT	T-TT	L-T	L-TT
Major Axis Length	Mean (mm)	1.2	9.1	9.6	1.1	9.6	10.2
	Median (mm)	0.6	4.6	4.6	0.6	4.6	4.6
	St. Dev. (mm)	1.4	10.9	11.4	1.4	12.1	12.6
Minor Axis Length	Mean (mm)	0.6	0.8	0.8	0.6	0.8	0.7
	Median (mm)	0.3	0.6	0.6	0.3	0.4	0.4
	St. Dev. (mm)	0.6	1.0	0.8	0.6	1.0	0.8
Aspect Ratio	Mean	1.8	13.5	13.9	1.7	14.8	15.4
	Median	1.6	16.0	16.0	1.5	16.0	16.0
	St. Dev.	0.9	6.4	6.3	0.9	6.6	7.1
Area	Mean (mm^2)	0.87	8.22	7.73	0.78	8.96	7.72
	Median (mm^2)	0.19	2.00	2.00	0.13	2.00	2.00
	St. Dev. (mm^2)	2.28	25.35	21.99	2.23	28.91	22.79

The two point probability function provides the characterization of spatial arrangement of the phases of a heterogeneous material [47]. Considering the heterogeneous material to occupy a domain Ω and to consist of two phases that occupy Ω_1 and Ω_2 such that $\Omega_1 \cup \Omega_2 = \Omega$ and $\Omega_1 \cap \Omega_2 = \phi$. The two point probability function is defined to be:

$$S_1(x_1, x_2) = Pr(x_1 \in \Omega_1 \cap x_2 \in \Omega_1) \tag{2.1}$$

the probability that both points x_1 and x_2 are in phase 1. When $x_1 = x_2$ the value of this function is simply the volume fraction of phase 1. And when x_1 and x_2 are widely separated, their probabilities of occurrence do not affect each other (i.e. the points are uncorrelated and statistically independent), therefore the value of function approaches the product of probabilities that either points are in phase 1 which equals the square of phase 1 volume fraction. This function contains essentially the same information as the spatial correlation function:

$$r(x_1, x_2) = E[1_{x_1 \in \Omega_1} \times 1_{x_2 \in \Omega_1}] \tag{2.2}$$

in which E[.] is the expectation operator and 1[.] is an indicator function. In the case where the heterogeneous material is stationary and statistically isotropic, the two point probability function depends only on $d = ||x_1 - x_2||$. If, on the other hand, the material is stationary but statistically anisotropic the two point probability function can be defined as a function of $d = ||x_1 - x_2||$ and $\theta = \text{atan}(([x_2]_2 - [x_1]_2)/([x_2]_1 - [x_1]_1))$ the distance of separation between the two points and the angle between a line connecting the two points and the x_1 axis ($[x_i]_j$ is the jth component of the position vector x_i). We have estimated the two point probability functions in the T-TT, L-T, and L-TT planes of the first billet, treating phase 1 as the void phase (Fig. 2.3) which clearly show the anisotropy present in the L-T and L-TT planes. The T, L and L directions correspond to $\theta = 0$ in the three figures showing that the voids are elongated in the L direction, and perhaps very slightly in the T direction for the T-TT plane. A mild anisotropy in the T-TT plane is supported by the deviation of the mean aspect ratio from unity in the T-TT plane. One can observe that the decay lengths of the two point probability functions correspond to the average dimensions of the voids in the various material directions on the various planes.

Another useful statistical measure for void 2D characterization is the lineal path function. For statistically isotropic media, lineal path function is defined as probability that a line segment of length z lies wholly in void phase when randomly thrown into the sample [47]. Naturally when the length of the line is zero, the lineal path function is equal to the void volume fraction; and when the line length is infinite, the lineal path function equals zero. Figure 2.4 illustrates the lineal path function evaluated in the T-TT, L-T, and L-TT planes of the first billet. The results are similar to the two point probability function. This similarity shows the fact that the voids in

PSL do not have wry and crooked shapes; therefore, when two points are in the void phase, the line connecting them is most probably in the same phase.

The last measure to obtain the 2D characteristics of voids is the chord length density function which is defined as the probability of finding a chord of length between z and $z + dz$ in void phase [47]. This measure is useful for the estimation of average void length. Based on the definition, when the chord length is zero, the chord length density function is equal to 1 and when the length is infinite, the function equals zero. Figure 2.5 displays the chord length density functions in the TT, T, and L directions in the first billet. The results clearly show that the longitudinal direction contains larger void lengths and that the voids in the L-T and L-TT sections are elongated, with average aspect ratios of approximately 10, in L direction.

Because 1) too many figures related to billet one have been put in this dissertation, and 2)our investigation showed that the statistics of these two billets are not significantly different, it is efficient not double the number of figures and just display the statistics of the first billet. This method has also been kept in the other sections throughout this dissertation. The tables, nevertheless, contain the data of both billets.

2.3 Three dimensional characterization of the voids structure

2.3.1 Direct characterization

The voids occupy 2.4% and 2.8% of the volume of first and second billets. Although in both billets the mean value of individual void's volume is 11 mm^3, the median of void volume is much less (0.5 mm^3 that equals the volume of two voxels). This fact illustrates that the void volume distribution is highly skewed. Figure 2.6 along with the calculated values of skewness (40 in the first and 60 in the second billet), kurtosis (2250 in the first and 5100 in the second billet) and standard devia-

tion (150 mm^3 in the first and 180 mm^3 in the second billet) confirm this conclusion. Another sign of the skewness: although 43%/49% of voids in the first/second billet are one-voxel voids, in both billets they form just 1% of the whole void volume. While the largest void in the first/second billet represent 6%/8% of the void volume; i.e. the volume of one void is 6/8 times of the sum of the volumes of thousands of voids.

To get a sense about the three dimensional shape of the voids, one can employ the mass moment of inertia. The main difference between mass moment of inertia and area moment of inertia (the parameter that is widely used in solid mechanics) is that the term of length appears by the power of 5 in the equation of mass moment of inertia while it has the power of 4 in the equation of area moment of inertia. The other difference is that the density of the material affects mass moment of inertia but does not have any influence on area moment of inertia. Here, since the shape of voids is of interest, the density of voids was arbitrarily set to be 1 when calculating the moments of inertia. The values of each void's principal mass moments of inertia has been calculated and studied. If the void's mass moment of inertia is equal about all principal axes, the void has a spherical shape. But if the mass moment of inertia about one principal axis is larger than its value about another principal axis, the length of the first principal axis is less than the second one's length. The statistical study shows that the distributions of void principal mass moments of inertia are significantly skewed. Table 2.2 and Fig. 2.7 show the statistical data and normalized distributions of the principal moments of inertia respectively. In this paper, I_{11} is the moment of inertia about the major principal axis of void; hence it is the smallest principal moment of inertia, while I_{33} which is the moment of inertia about the minor principal axis is naturally the largest one. Considering the values stated in Tab. 2.2 one can conclude that the length, shape and distribution of the voids are similar in the tested billets. All the corresponding statistical data of moments of inertia are of

the same order; hence the void statistics is homogeneous inside the billets that are cut from a bigger PSL billet.

Table 2.2. Statistical data of the voids principal mass moments of inertia in both billets

		Mean (mm^5)	Median (mm^5)	St. Deviation (mm^5)	Skewness	Kurtosis
First Billet	I_{11}	300	0.10	15000	75	6100
	I_{22}	36000	0.63	1540000	75	6300
	I_{33}	36300	0.63	1550000	75	6300
Second Billet	I_{11}	750	0.10	81000	140	19300
	I_{22}	43000	0.63	2270000	110	13500
	I_{33}	43600	0.63	2280000	110	13200

The other important parameter that can help us to detect the shape of the voids is the aspect ratio of the principal moments of inertia. Figure 2.8 displays how the aspect ratios are distributed.

It is clear in the three figures above that in most of the voids, I_{11} is much smaller than the two other almost equal principal moments of inertia, I_{22} and I_{33}. Therefore, in most of the voids, one of the principal axes is much larger than the other two almost equal axes. This conclusion is in agreement with the results taken from chord length density functions (Fig. 2.5).

Since the ultimate goal of this study is to generate random voids virtually and use them in the study of mechanics of PSL for making arbitrarily sized PSL models, the correlation coefficients of principal moments of inertia are as important as their distribution. Here are the matrices of correlation coefficients of principal moments of inertia for both billets:

$$\rho_{I_{first}} = \begin{bmatrix} 1 & 0.96 & 0.96 \\ 0.96 & 1 & 1 \\ 0.96 & 1 & 1 \end{bmatrix} \tag{2.3}$$

$$\rho_{I_{second}} = \begin{bmatrix} 1 & 0.27 & 0.30 \\ 0.27 & 1 & 1 \\ 0.30 & 1 & 1 \end{bmatrix} \tag{2.4}$$

The major and second major moments of inertia (i.e. I_{33} and I_{22}) are perfectly correlated. This is because of the fact that most of the voids grow just in longitudinal direction and have the aspect ratio in the order of 1 in T-TT sections.

Histograms of the coordinates of each void's centroid along the transverse, thru thickness and longitudinal directions have been shown in Fig. 2.9. The distribution of coordinates along the transverse and thru thickness directions is uniform, but there is a little doubt about the longitudinal direction. Figure 2.9(c) shows that the frequency of the presence of the centroids at the longitudinal edges is more than the other locations. One possible explanation is that the distribution has been disturbed at the edges due to the process of cutting the billet; and since the voids are much longer in longitudinal direction, this effect is more tangible for the distribution of centroids in this direction. To test this hypothesis, a 10000×1000 mm rectangular domain containing 10000 uniformly distributed identical 10×0.5 mm rectangles was assumed (Fig.2.10). Now, if cutting the edges of rectangular domain results in the distortion of distribution of the coordinates of rectangles' centroids, the hypothesis will be confirmed. Figures 2.11 shows the distribution of coordinates of rectangles' centroids after cutting 500 mm from each side of domain's length and 50 mm from each side of domain's width. The hypothesis appears to be true.

The direction of the voids, i.e. their angle with the coordinate axes, is another piece of data required for void characterization. In the bottom right corner of Fig. 2.12, the orientation of major principal axis of each void is depicted by a line with unit length. Figure 2.12 presents the same data in stereographic form. Each point

represents the projection of intersection of the lines shown in the figure at the corner with a sphere with unit radius centered at the origin in T-TT plane. Obviously, almost all of the voids are aligned along the interval of -30° to 30° of the longitudinal direction. A few voids have made larger angles with the longitudinal direction; these voids are either very short or spherical. Therefore, it is reasonable to accept that all voids in PSL are aligned in the longitudinal direction or make small angles with this direction.

Finally, Fig. 2.13 shows the distribution of angles that the projections of voids major axis in x-z (T-L) and y-z (TT-L) planes make with z-axis (longitudinal direction). These figures confirm that most of the voids are aligned along longitudinal direction. The principal angles were found to be uncorrelated.

2.3.2 Characterization through equivalent ellipsoids

In order to provide a methodology to generate virtual voids, it is reasonably favorable to approximate the actual shape of the voids with ellipsoids. The observations and statistical data show that ellipsoidal shape might be a good approximation for actual void shape. This section is allocated to the verification of this hypothesis. Working with the ellipsoidal shapes instead of the actual arbitrary shapes eases the understanding of void characteristics and simulation of voids by finite element models.

Let a void be modeled by an ellipsoid with centroid c and major axis half-length R_1 and minor axis half-lengths R_2 and R_3. The volume of such an ellipsoid is given by:

$$V = \frac{4}{3}\pi R_1 R_2 R_3 \tag{2.5}$$

Based on the void geometry shown in Figs. 2.6,2.7 and Tab. 2.2, a reasonable initial assumption is that the ellipsoid's major radius R_1 is aligned with the void's major principal axis (based on Fig.2.12, in most cases L direction), the second minor radius

R_2 is aligned with the void's second minor principal axis (in most cases T direction), and the minor radius R_3 is aligned with the void's minor principal axis (in most cases TT direction). Assuming the unit density, the principal moments of inertia of the ellipsoid are then:

$$I_{11} = \frac{V(R_2^2 + R_3^2)}{5} \tag{2.6}$$

$$I_{22} = \frac{V(R_1^2 + R_3^2)}{5} \tag{2.7}$$

$$I_{33} = \frac{V(R_1^2 + R_2^2)}{5} \tag{2.8}$$

The goal of this model would be to calibrate the mean ellipse dimensions R_1, R_2, and R_3 to the statistics of chapter 2 and choose distributions of these parameters to match at least the second moment properties of the void mesostructure. It must be noted that setting Eqs.2.5, 2.6, 2.7 and 2.8 equal to the mean values in Tab. 2.2 results in an over-determined system of equations that may not have an acceptable solution (4 equations but 3 unknowns). An appropriate way to tackle this problem is to eliminate two unknowns (e.g. R_2 and R_3) by combining the equations and form two equations dependent on just one unknown (e.g. R_1). We now can minimize the square root of sum of the squares of these two equations and find the only remaining unknown. For example, by combining the Eqs. 2.5, 2.6, 2.7 and 2.8, one can conclude:

$$R_1^2 + [\frac{3V}{4\pi R_1 \sqrt{\frac{5I_{33}}{V} - R_1^2}}]^2 + \frac{5I_{22}}{V} = 0 \tag{2.9}$$

$$(\frac{5I_{33}}{V} - R_1^2) + [\frac{3V}{4\pi R_1 \sqrt{\frac{5I_{33}}{V} - R_1^2}}]^2 + \frac{5I_{11}}{V} = 0 \tag{2.10}$$

Note that V, I_{11}, I_{22} and I_{33} are the geometric properties of voids. R_1 is computable by minimizing SRSS of Eqs. 2.9 and 2.10. Once R_1 is calculated, R_2 and R_3 can be found using the following equations:

$$R_2 = \sqrt{\frac{5I_{33}}{V} - R_1^2} \tag{2.11}$$

$$R_3 = \frac{3V}{4\pi R_1 R_2} \tag{2.12}$$

Figure 2.14 shows the distribution of radii of the equivalent ellipsoids. Expectedly, these distributions look like the distributions of the corresponding moments of inertia (Fig. 2.7).

And here are the histograms displaying the distributions of moments of inertia and the radii aspect ratios. While the moments of inertia of equivalent ellipsoids (Fig. 2.15) match well the moments of inertia of actual voids (Fig. 2.7), the aspect ratios of radii (Fig. 2.16)do not have the same distribution as the aspect ratios of voids' moments of inertia (Fig. 2.8). This is not surprising, because the radii do not have linear relationship with moments of inertia; and also, all three radii have a contribution to the aspect ratios of moments of inertia.

Table 2.3. Comparison of the statistics of the voids of both PSL billets with equivalent ellipsoids

		Mean			Median		
		I_{11} (mm^5)	I_{22} (mm^5)	I_{33} (mm^5)	I_{11} (mm^5)	I_{22} (mm^5)	I_{33} (mm^5)
First Billet	Void	300	36000	36300	0.10	0.63	0.63
	Eq. Ellipsoid	275	36000	36300	0.10	0.63	0.63
Second Billet	Void	750	43000	43600	0.10	0.63	0.63
	Eq. Ellipsoid	710	43000	43600	0.10	0.63	0.63

The matrices of correlation coefficients of the equivalent ellipsoid radii are as follows:

$$\rho_{R_{first}} = \begin{bmatrix} 1 & 0.81 & 0.28 \\ 0.81 & 1 & 0.34 \\ 0.28 & 0.34 & 1 \end{bmatrix} \tag{2.13}$$

$$\rho_{R_{second}} = \begin{bmatrix} 1 & 0.69 & 0.32 \\ 0.69 & 1 & 0.27 \\ 0.32 & 0.27 & 1 \end{bmatrix} \tag{2.14}$$

2.4 Probabilistic model for PSL mesostructure

Once the distributions of equivalent ellipsoids are obtained, one can generate virtual ellipsoidal voids with randomly generated radii, alignments and locations. Given that no clustering of voids was observed in the mesostructure, the centroids of the voids can be modeled by uniform distribution (Fig. 2.9). But no mathematically known and defined distribution can be fitted to the distributions of ellipsoid radii (Fig. 2.14) and void principal angles (Fig. 2.13). The translation model [8] was used to generate non-Gaussian random radii and angles with specified marginal target distributions and correlation functions (Eqs.2.3 and 2.13).

Suppose that the generation of a correlated non-Gaussian random vector, $\mathbf{Z} \in \mathbf{R^d}$, with components Z_i, mean $\boldsymbol{\mu}$ and covariance matrix $\mathbf{c}$ defined by $\mathbf{c} = \mathbf{E}[(\mathbf{Z} - \boldsymbol{\mu})(\mathbf{Z} - \boldsymbol{\mu})^{\mathbf{T}}]$ is of interest (where $E(.)$ is the expectation operator). According to the translation method, first a vector of uncorrelated Gaussian random variables, $\mathbf{Y} \in \mathbf{R^d}$ with components Y_i, is generated. Choleski decomposition this vector to a correlated Gaussian vector, $\mathbf{Y'}$ with components Y_i', using the target correlation coefficients (c_{ij}). This new correlated Gaussian vector can be transformed to a correlated non-Gaussian

random vector, $\mathbf{Z}$, using the experimental cdf obtained from the target distributions. The transformation is given by:

$$Z_i = F^{-1}(\Phi(Y_i')) \tag{2.15}$$

where $F(z)$ is the cumulative distribution function (cdf) of $\mathbf{Z}$ and $\Phi(.)$ is the standard (mean zero, unit variance) Gaussian cdf. In the case of this study, $\mathbf{Z}$ can be the vector of major (or any other type of) ellipsoid radii whose cumulative distribution function ($F(z)$) has been evaluated empirically from the data of fitted equivalent ellipsoids.

Figure 2.17 shows the distribution of the volume of virtually generated ellipsoidal voids which acceptably matches the distribution of the volume of actual voids in the first billet(Fig. 2.6). Therefore, one can generate virtual voids based on the statistical data provided in chapter 3 and virtually generate a PSL specimen with any arbitrary size.

Figure 2.18 displays the distributions of the radii of virtual ellipsoidal voids. They properly match the distributions of the radii of equivalent ellipsoids shown in Fig.2.14. It is also important that the correlation coefficients of virtual radii match the actual values; Eq. 2.16 shows a good agreement between correlation coefficients. Hence, the generation of virtual voids with the size and size correlation similar to actual ones is absolutely possible.

$$\rho_R = \begin{bmatrix} 1 & 0.78 & 0.25 \\ 0.78 & 1 & 0.29 \\ 0.25 & 0.29 & 1 \end{bmatrix} \tag{2.16}$$

Figures 2.19 , 2.20 and 2.21 are the other signs that the size and shape of the virtual voids are the same as actual voids in the first billet. More details about the

comparison of the moments of inertia of actual and virtual voids have been presented in Table 2.4.

Table 2.4. Comparison of the statistics of actual and virtual voids

	Mean			Correlation		
	I_{11} (mm^5)	I_{22} (mm^5)	I_{33} (mm^5)	ρ_{12}	ρ_{13}	ρ_{23}
Actual	300	36000	36300	0.96	0.96	1.00
Virtual	300	44800	45100	0.92	0.92	1.00

Since the location of virtual voids has been randomly selected based on the uniform distribution, there is no doubt that the centroids of virtual voids (Fig. 2.22) are distributed in the same manner as the centroids of actual voids (Fig. 2.9).

To make sure that the orientation of virtual voids follows the actual orientations, one can compare Fig. 2.23 to Fig. 2.13. Note that the angles of more than 10° have been neglected due to their rare appearance in the distribution of the actual angles.

All in all, regarding the size, shape, location and alignment of the voids, the randomly generated virtual ellipsoidal voids have the same statistical data as the actual voids observed in the first PSL billet.

2.5 Problem of Outlier Ellipsoids

There are some equivalent ellipsoids (ellipsoids which have been fitted to actual voids) with unreasonable aspect ratios in T-TT sections (aspect ratios larger than 20). We call these ellipsoids outliers. Despite the fact that the method of fitting proper ellipsoids to voids is sound, the outliers are caused by the bifurcation of voids. In other words, when actual voids have different branches laying along different directions (like voids highlighted in Fig.2.24), the method explained before to fit ellipsoids to actual voids does not work favorably and results in ellipsoids with unreasonable aspect ratio in T-TT plane.

We decided to eliminate the outliers (which form 38% of the whole ellipsoidal void volume fraction) and define new ellipsoids with lower aspect ratios in T-TT section. In this method which is called method#2, the lengths of the axes of each ellipsoid are assumed to be equal to the distance between the maximum and minimum voxel coordinates of the corresponding void in each direction. The volume of this ellipsoid is certainly equal or larger than the void. The lengths of axes of ellipsoid are then scaled down so that ellipsoid's volume matches the corresponding void volume. This method was applied to the outliers and the result showed that the new ellipsoids generated by this method are more circular in T-TT section but shorter in L direction. Therefore, the moments of inertia of the new ellipsoids do not match that of the voids. We decided to neglect this defect and use the new ellipsoids generated by method#2 instead of the outliers. The location of the center and orientation of the new ellipsoids are the same as the outliers. Figure 2.25 shows a T-TT section including equivalent ellipsoids which have been modified using method#2.

The other problem related to method#2 may happen when models consisting of actual voids and equivalent ellipsoids are to be made and compared mechanics-wise. The problem is that by changing the shape of the ellipsoids (especially their length), the volume fraction of the voids in a model of actual voids with a certain size may differ from the volume fraction of equivalent ellipsoids in a model of the same size taken from exactly the same position in the parent billet. In such cases, it was decided to change the position of the models including equivalent ellipsoids in the parent billet so that the volume fractions match.

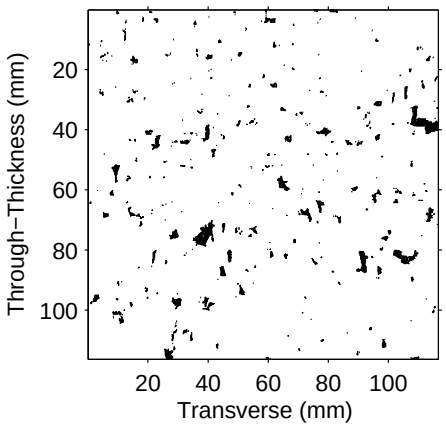

(a) T-TT section

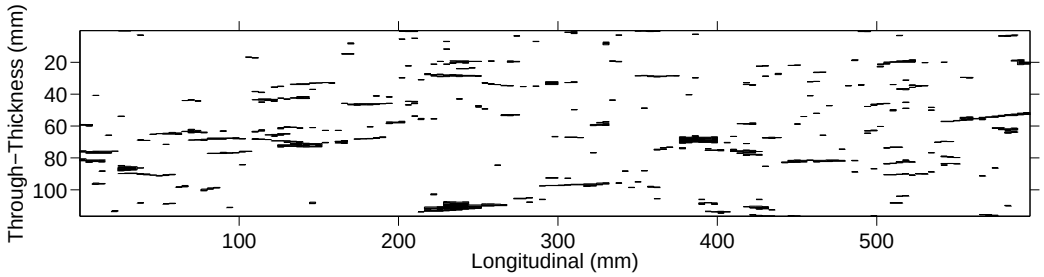

(b) L-TT section

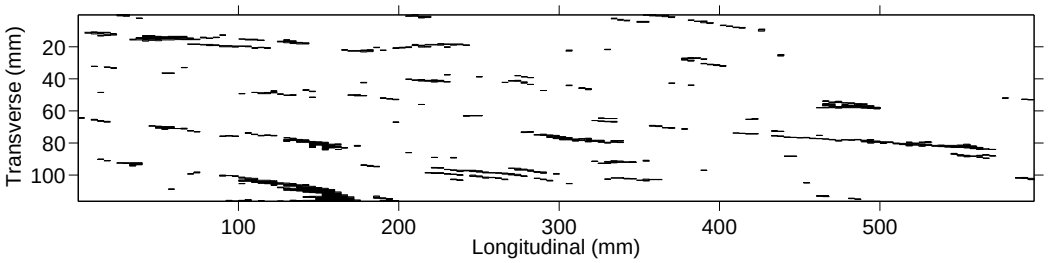

(c) L-T section

Figure 2.2. Three section views through the three dimensional reconstruction of the PSL mesostructure. Black regions represent void and white regions represent wood strands

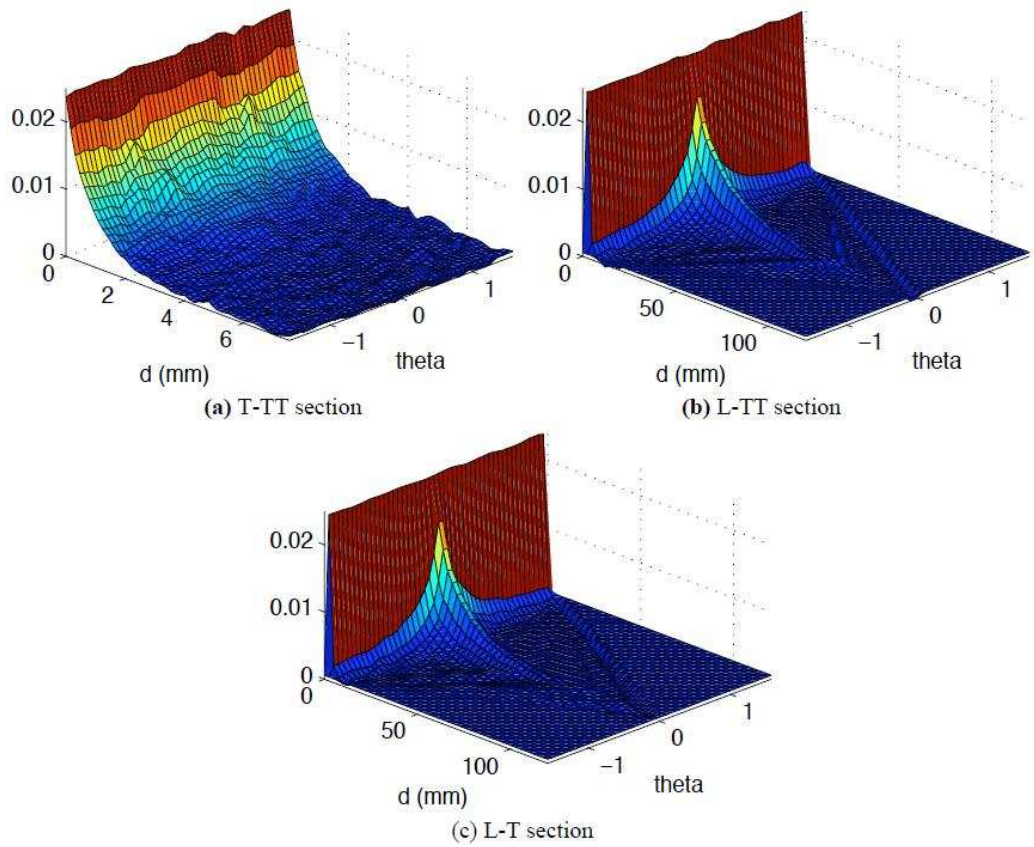

Figure 2.3. Two point probability functions for the first PSL billet

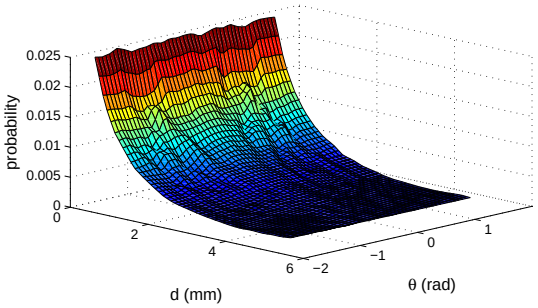

(a) T-TT section

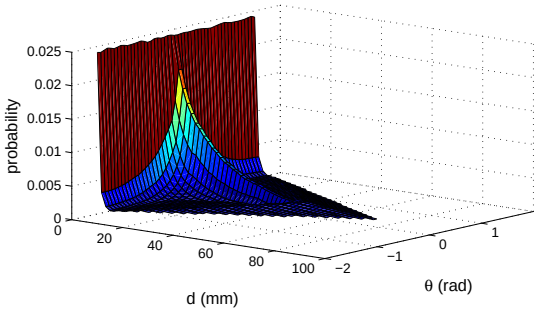

(b) L-TT section

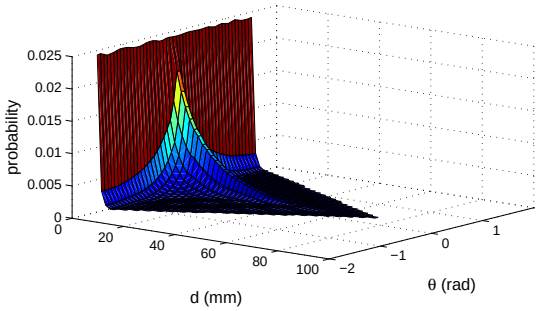

(c) L-T section

Figure 2.4. Lineal path functions for the first PSL billet

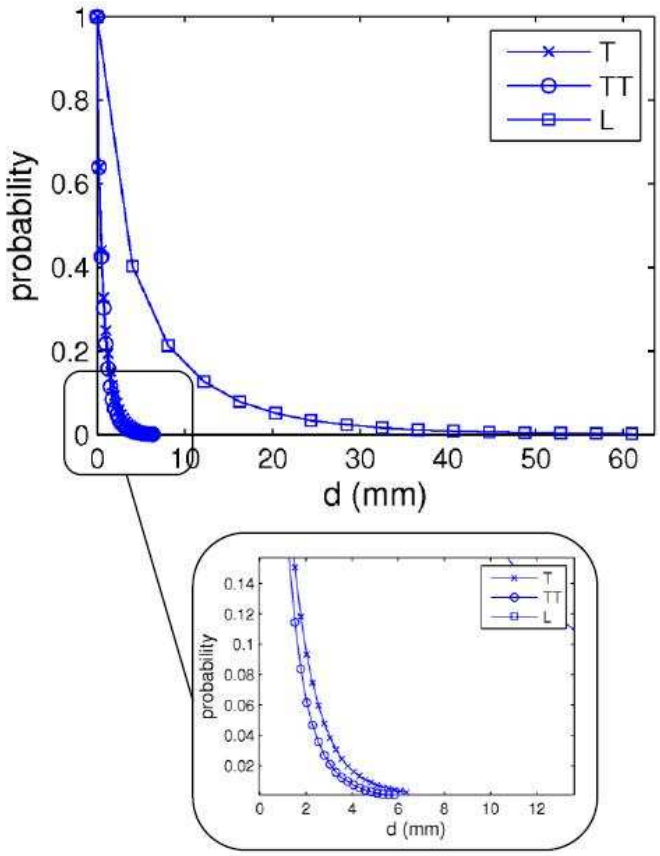

Figure 2.5. Chord length density function in all three directions of the first PSL billet

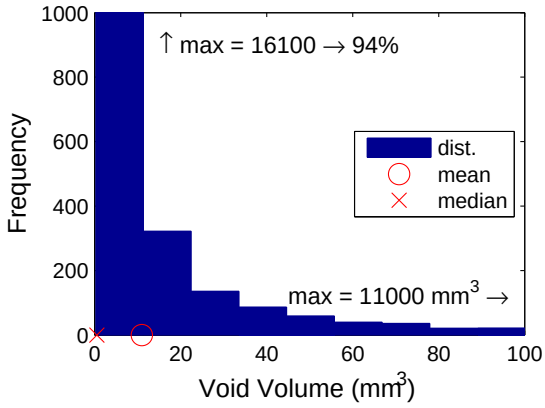

Figure 2.6. Distribution of volume of the first PSL billet voids

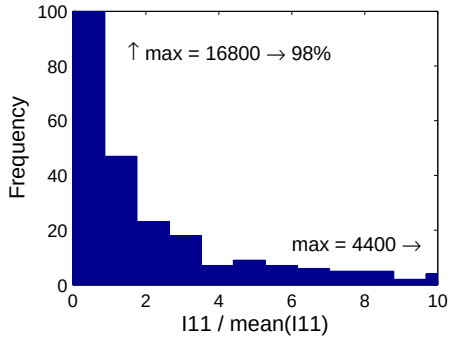

(a) minor principal MOI

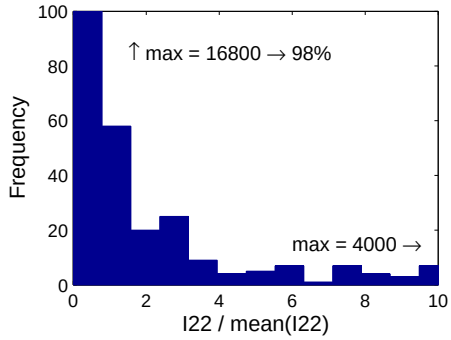

(b) second major principal MOI

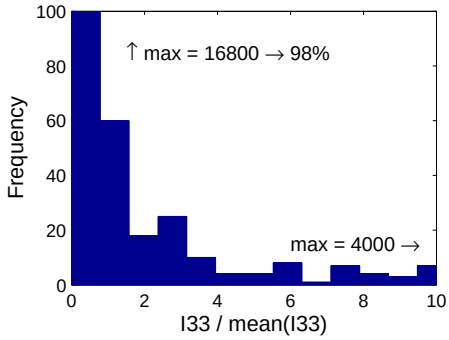

(c) major principal MOI

Figure 2.7. Distribution of principal moments of inertia of the first PSL billet voids

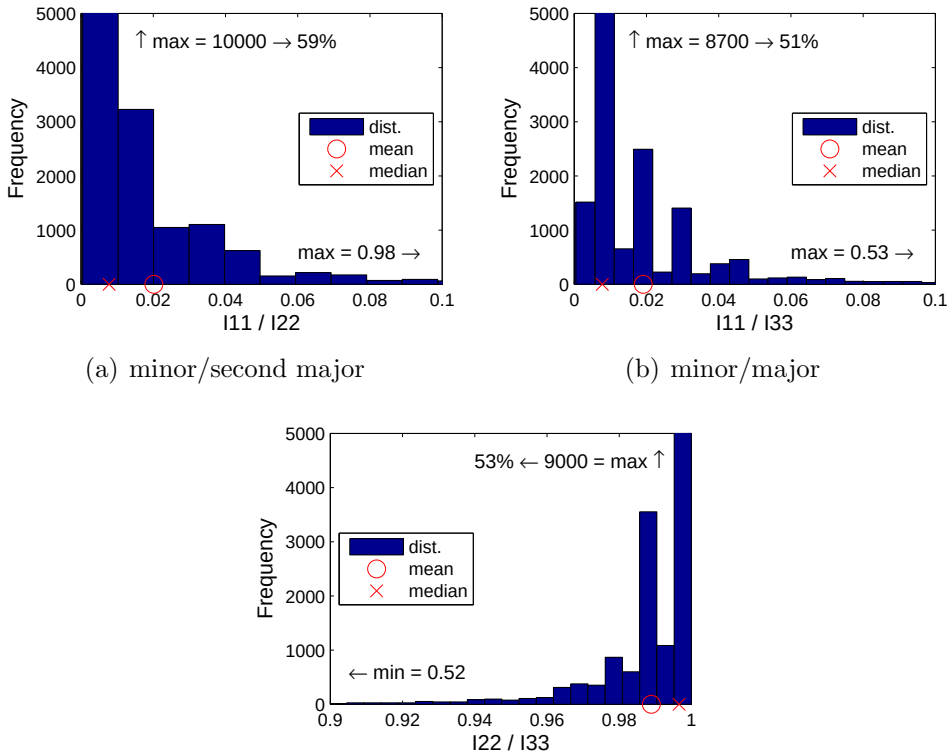

(a) minor/second major

(b) minor/major

(c) second major/major

Figure 2.8. Distribution of aspect ratio of principal moments of inertia of the first PSL billet voids

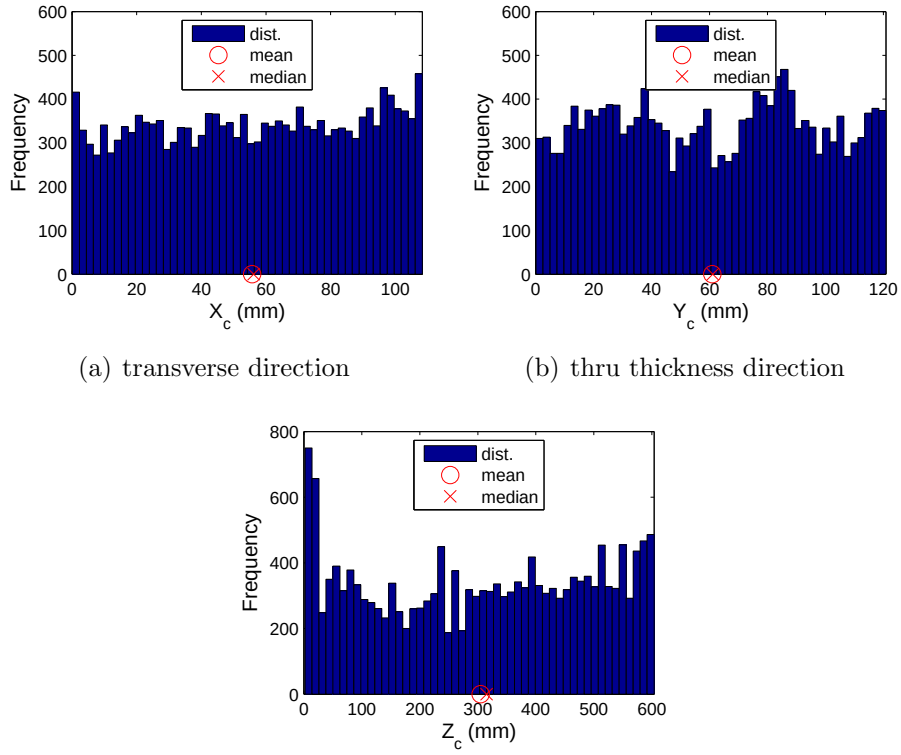

(a) transverse direction

(b) thru thickness direction

(c) longitudinal direction

Figure 2.9. Distribution of the coordinates of centroid of the first PSL billet voids

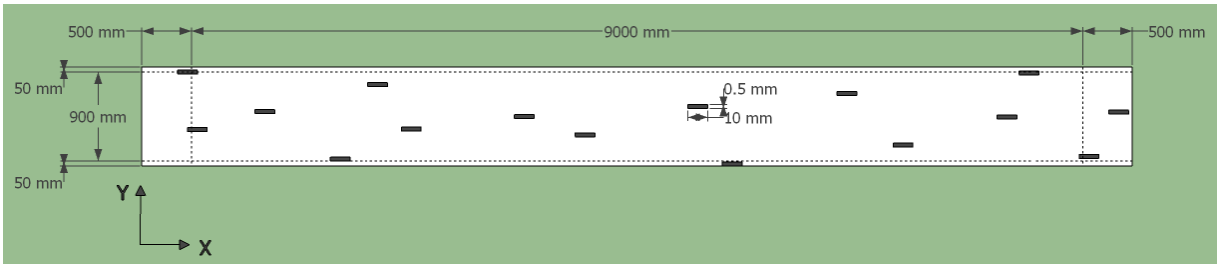

Figure 2.10. Hypothetical rectangular domain containing 10000 uniformly distributed identical rectangles before (solid edges) and after (dashed edges) the edge crop

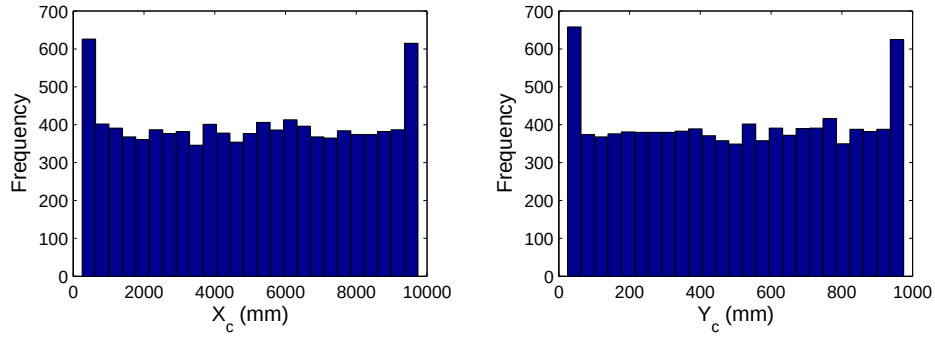

(a) X coordinate (b) Y coordinate

Figure 2.11. Distribution of the coordinates of centroid of the hypothetical rectangles after the edge crop

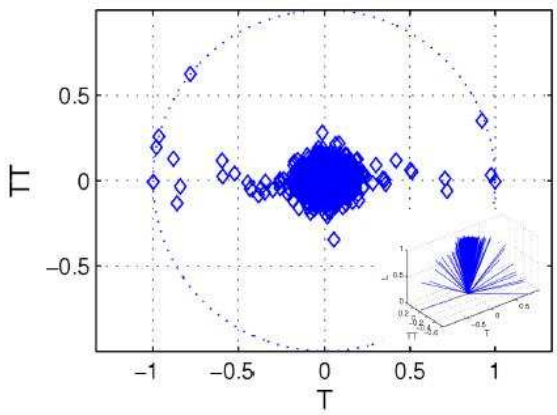

Figure 2.12. Stereographic projection of the voids in the first billet with respect to longitudinal axis

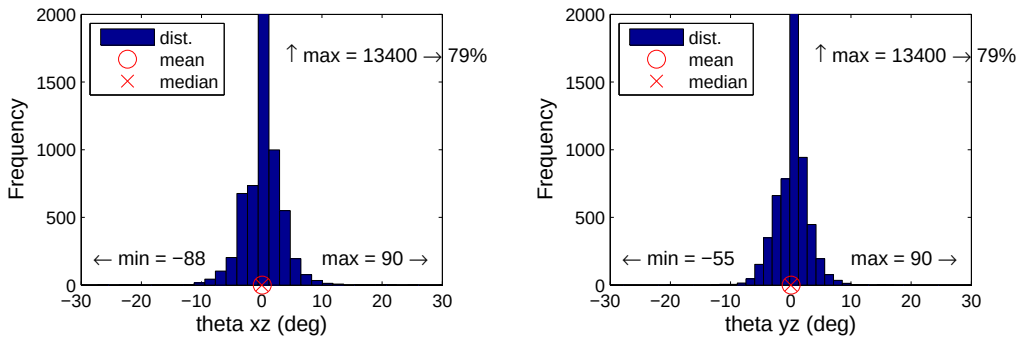

(a) L-T section (b) L-TT section

Figure 2.13. Distribution of the angle that the major principal axis of voids in the first billet makes with the longitudinal direction

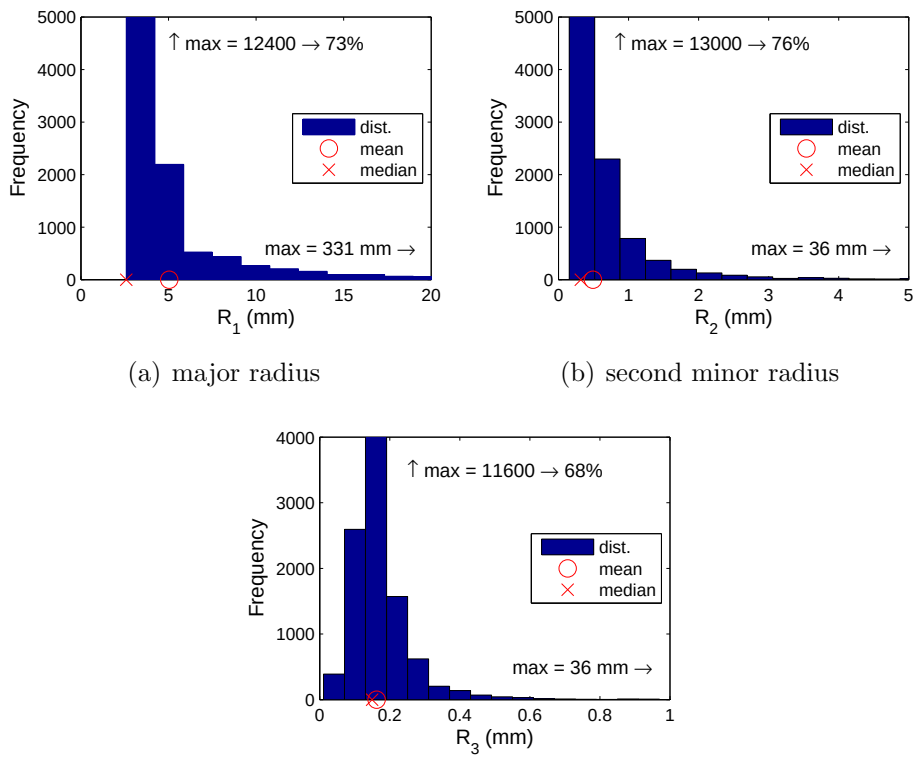

(a) major radius (b) second minor radius

(c) minor radius

Figure 2.14. Distribution of the radii of equivalent ellipsoids fitted to the voids of first billet

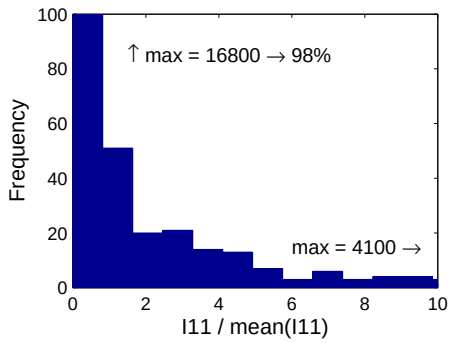

(a) minor principal MOI

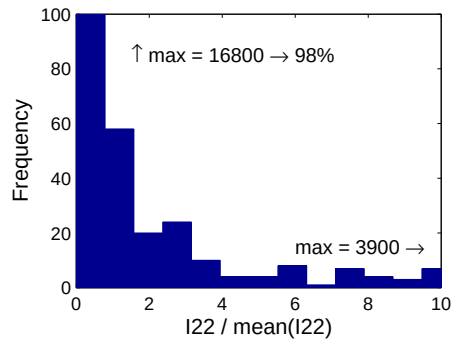

(b) second major principal MOI

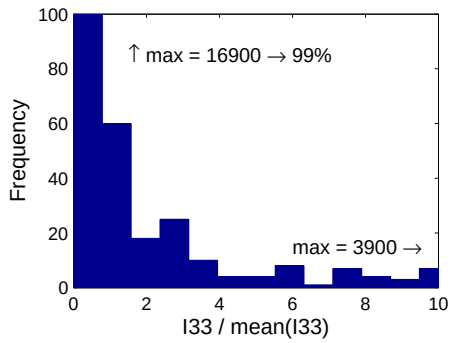

(c) major principal MOI

Figure 2.15. Distribution of the principal moments of inertia of equivalent ellipsoids fitted to the voids of first billet

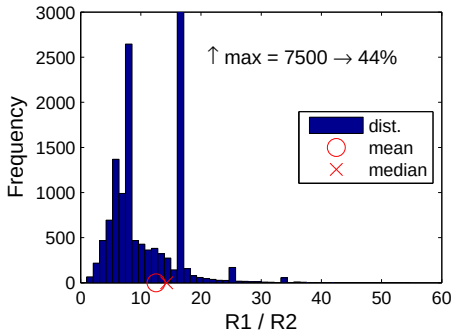

(a) major/second minor

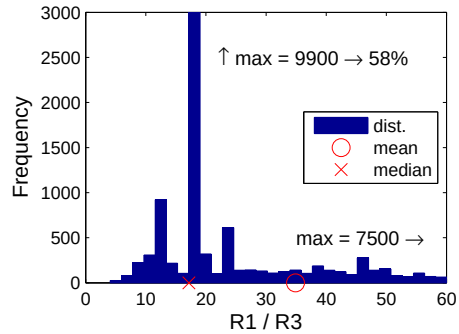

(b) major/minor

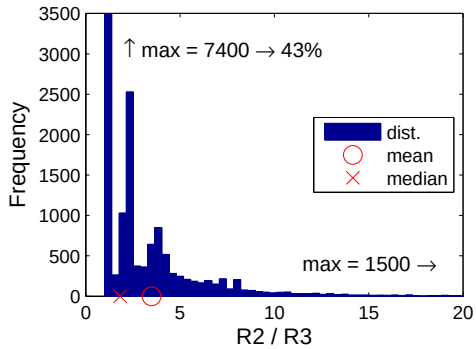

(c) second minor/minor

Figure 2.16. Distribution of the radius aspect ratios of equivalent ellipsoids fitted to the voids of first billet

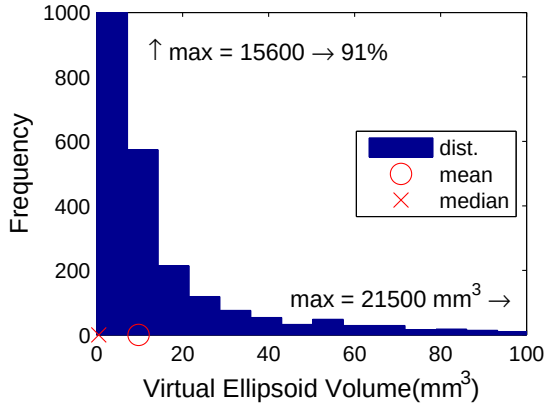

Figure 2.17. Distribution of the volume of randomly generated virtual ellipsoids

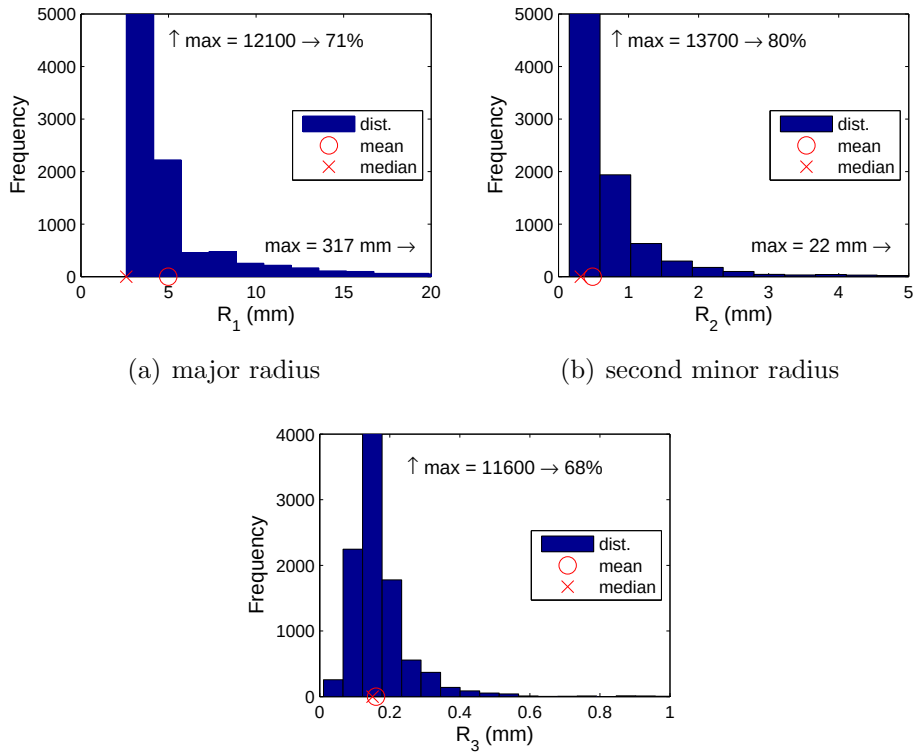

(a) major radius

(b) second minor radius

(c) minor radius

Figure 2.18. Distribution of the radii of randomly generated virtual ellipsoids

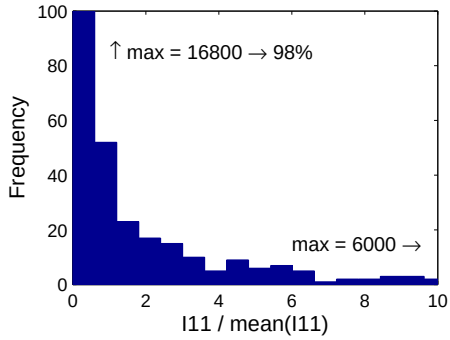

(a) minor principal MOI

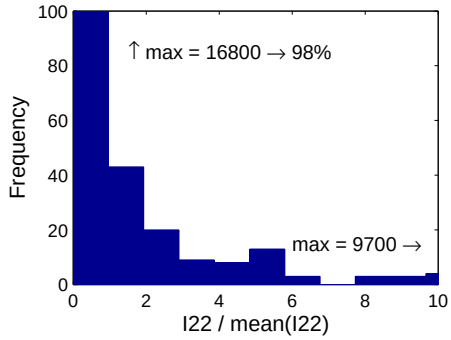

(b) second major principal MOI

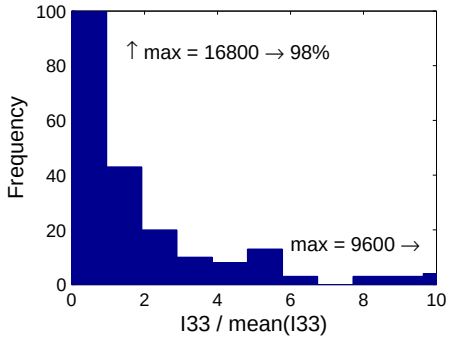

(c) major principal MOI

Figure 2.19. Distribution of principal moments of inertia of randomly generated virtual ellipsoids

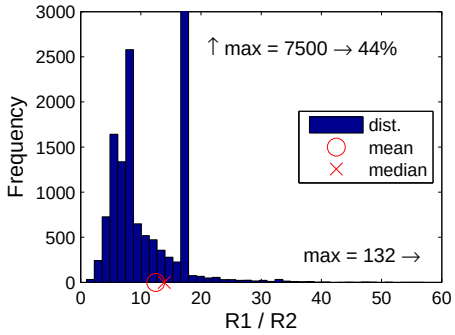

(a) major/second minor

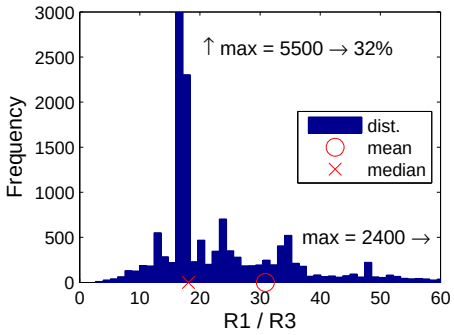

(b) major/minor

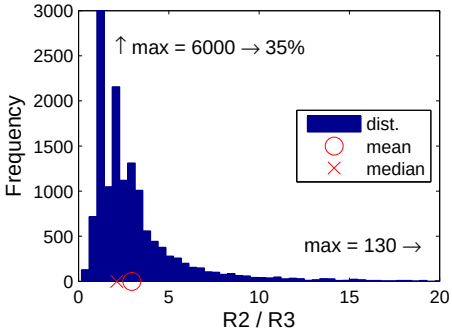

(c) second minor/minor

Figure 2.20. Distribution of the radius aspect ratios of randomly generated virtual ellipsoids

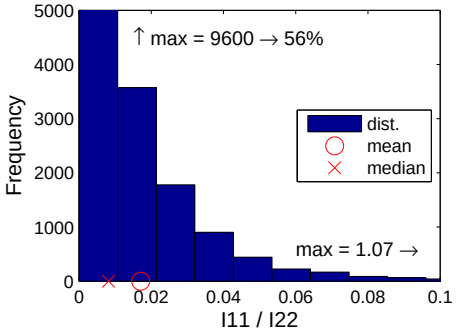

(a) minor/second major

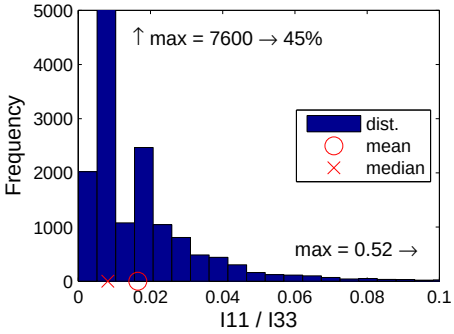

(b) minor/major

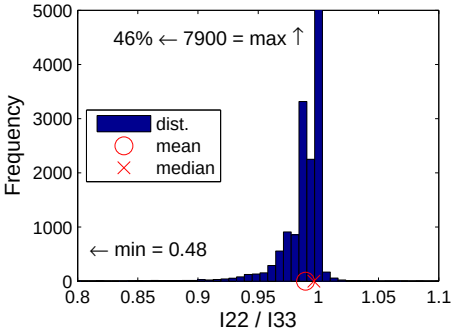

(c) second major/major

Figure 2.21. Distribution of aspect ratio of principal moments of inertia of randomly generated virtual ellipsoids

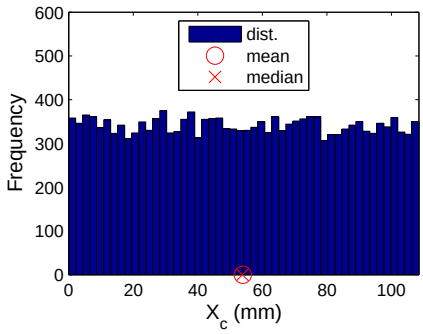

(a) transverse direction

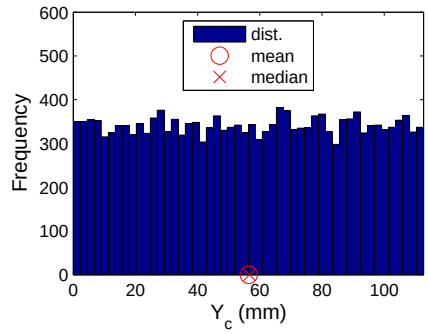

(b) thru thickness direction

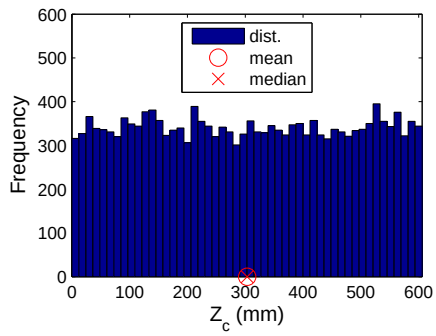

(c) longitudinal direction

Figure 2.22. Distribution of the coordinates of centroid of randomly generated virtual ellipsoids

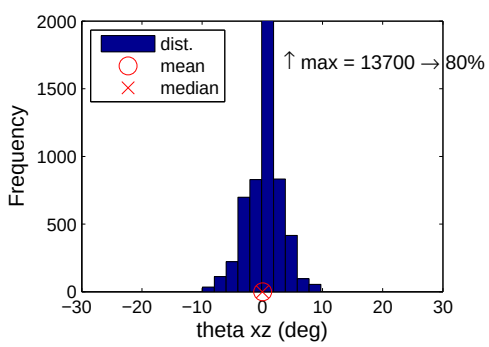

(a) L-T section

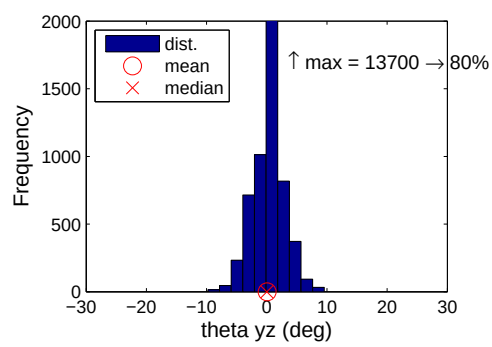

(b) L-TT section

Figure 2.23. Distribution of the angle that the major principal axis of randomly generated virtual ellipsoids makes with the longitudinal direction

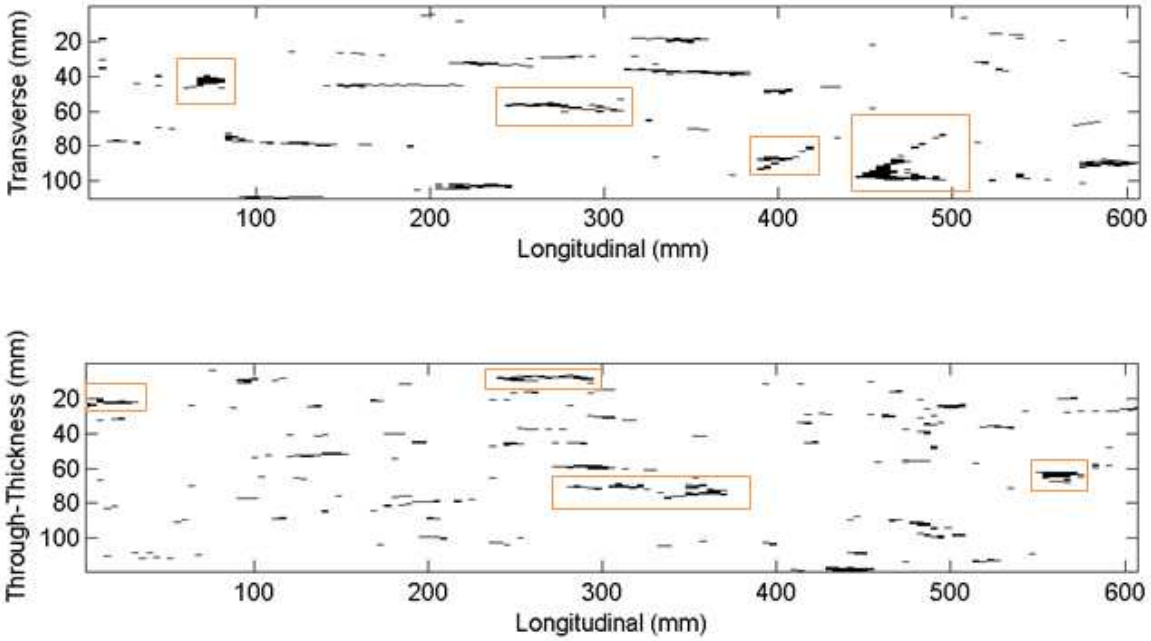

Figure 2.24. Bifurcation of actual voids causes the generation of outlier equivalent ellipsoids

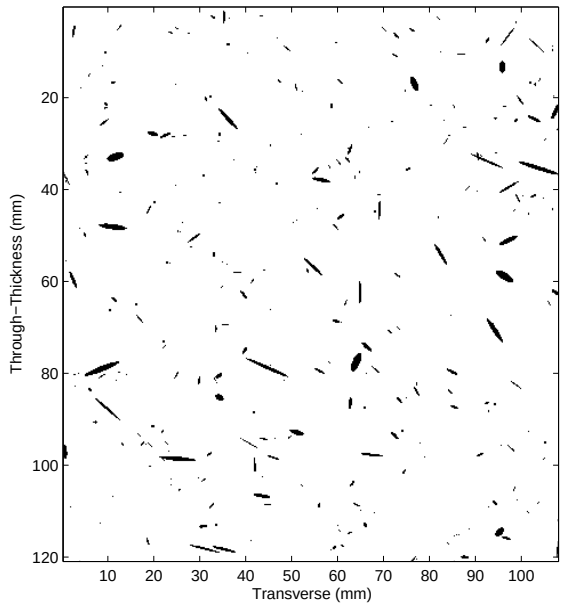

Figure 2.25. A T-TT section of ellipsoidal voids including modified outliers

CHAPTER 3

STUDY OF THE EFFECT OF VOID SHAPE ON PSL MECHANICS CONDUCTING LINEAR ANALYSIS

3.1 Problem Statement

This study is being conducted to test the hypothesis that the virtual ellipsoidal voids (section 2.4) can be an appropriate replacement for the actual voids. The change in the shape of the voids, i.e. the transformation of arbitrarily shaped voids which could have sharp tips into smooth ellipsoids, may affect the distribution of stresses. There is no guarantee that a finite element model including the ellipsoidal voids can detect the stress concentration usually seen at the tip of actual voids. Also, the void tips may cause local multiaxiality. Local multiaxiality is the term used in this report to address the existence of large stresses in the directions other than the direction of loading (here the large stress means of the same order of magnitude as that of the stress along the direction of loading). It is necessary to investigate if the ellipsoidal voids are able to model the local multiaxiality.

Comparison of the results of linear analysis of a model including actual voids with that of a model including corresponding equivalent ellipsoids is the first step required to be done to fulfill this study. Since the models are taken from exactly the same location in PSL billet, and also because the location and orientation of equivalent ellipsoids are the same as that of the voids, the only difference is the shape of the voids. The linear analysis of the orthotropic material may be able to show the effect of void shape on both stress concentration and local multiaxiality. It is necessary to conduct the analyses under uniaxial loading in three main material directions and

check the stress distribution in all loading cases. The normal stresses (stresses along the material directions) control the ductile failure of PSL under compression; however, the principal stresses are important for the brittle failure under tension. Therefore, the distribution of these stresses must be checked and if they match in both void models, it is shown that the void shape does not affect the stress state of material. On the other hand, if the stress distributions do not match but the mean and median of stresses match, a nonlinear study should be conducted to clarify if the ellipsoidal shape is usable for a certain type of simulations (e.g. compressive simulation) or not.

Three loading scenarios, namely, uniaxial compressive loadings along the three main material directions, have been selected for the linear analyses. Under each type of loading, a model including actual voids and a model including equivalent ellipsoids are analyzed. To summarize the linear study, totally 6 simulations have been carried out scrutinized.

3.2 Material Properties and Finite Element Modeling

The material consists of two phases, wood and void. The wood phase is considered elastic orthotropic with elastic moduli E_L=13000 MPa, E_T = 650 MPa and E_{TT}=650 MPa in L, T and TT directions respectively. The value of E_L has been taken from Wood Handbook [4]. E_T and E_{TT} have been calculated using Eq. 3.1 presented in [35].

$$E_2 = E_3 = \frac{1}{20} E_1 \tag{3.1}$$

In our case, the directions 1, 2 and 3 respectively correspond with L, T and TT directions. The values of shear moduli are associated with the 2.0E SP PSL material (not merely the wood phase) based on the measurement of Janowiak et al. [33]. The Poisson's ratios have been chosen so that the inequalities (Eqs. 3.2,3.3,3.4) used in the

software ADINA to guarantee the stiffness matrix is positive definite hold. ADINA takes the values of ν_{12}, ν_{13} and ν_{23} from the user and calculates the other ratios using Eq. 3.5 [35, 4]. Table 3.1 includes the material elastic properties used in this study.

$$\nu_{12} < \sqrt{\frac{E_2}{E_1}} \tag{3.2}$$

$$\nu_{13} < \sqrt{\frac{E_3}{E_1}} \tag{3.3}$$

$$\nu_{12}\nu_{13}\nu_{23} < 0.5(1 - \nu_{12}^2\frac{E_1}{E_2} - \nu_{13}^2\frac{E_1}{E_3} - \nu_{23}^2\frac{E_2}{E_3}) \tag{3.4}$$

$$\frac{\nu_{ij}}{E_i} = \frac{\nu_{ji}}{E_j} \tag{3.5}$$

Table 3.1. Elastic constants of PSL strands

Constant	Value
E_L	13000 MPa
E_T	650 MPa
E_{TT}	650 MPa
ν_{LT}	0.15
ν_{LTT}	0.15
ν_{TTT}	0.09
G_{LT}	500 MPa
G_{LTT}	400 MPa
G_{TTT}	85 MPa

The linear analyses have been done separately for each of the three loading cases on orthotropic 25×25×76 mm PSL models(the model's longest side is always along

the direction of loading). All the simulations have been uniaxial compressive along each material direction and displacement control with the total displacement of 1 mm (total strain of 1.3%).

The size of each finite element is the same as the digital voxels, 0.25×0.25×4.02 mm in T,TT and L directions respectively. This size may not be very good for the loadings in T and TT directions. We will try to examine the effect of this aspect ratio in a later part of this chapter. ADINA's 3D-solid element has been selected to represent each finite element in the simulations. This element has rectangular prism shape with 8 nodes and 24 degrees of freedom (3 DOFs for each node). Obviously, no finite element has been allocated to the void phase.

The boundary conditions are only applied to the nodes at the base of each model. In all models, one of the base nodes is constrained along the three displacement directions and the other base nodes are just constrained along the direction of loading. Figure 3.1 displays schematically the dimensions, loading and boundary conditions of the models.

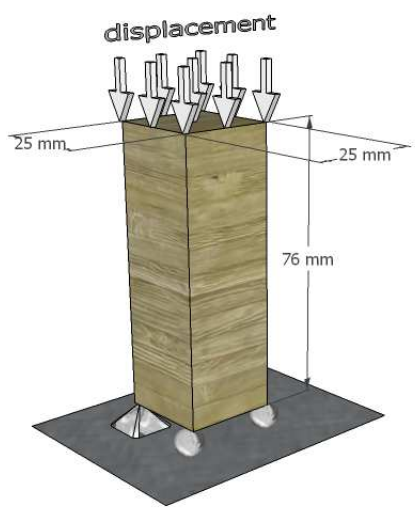

Figure 3.1. A schematic sketch of finite element models of PSL made for uniaxial linear and nonlinear analyses

The size of the PSL billet from which the finite element models are taken is 110×120×600 mm. The position of the lower left corner of the model used for the loading in L direction is (X_T=51 mm, Y_{TT}=51 mm, Z_L=102 mm) in the parent PSL billet. In the models used for loading in T and TT directions, the position of the lower left corners are respectively (X_T=0, Y_{TT}=51 mm, Z_L=102 mm) and (X_T=38 mm, Y_{TT}=5 mm, Z_L=102 mm). Note that, from now on, all the models are taken from the first billet characterized in chapter 2. So, the word "parent billet" always refers to the first billet.

3.3 Effect of Aspect Ratio of Finite Elements on Accuracy of Results

As mentioned in the last section, since the size of voxels is 0.25×0.25×4.02 mm in T, TT and L directions respectively, it is easier to make 3D solid finite elements with the same size. Also, the processor and memory limits of our available computers force us not to make very large models. A 25×25×76 mm PSL model contains about 210000 finite elements with the mentioned size. This is a rather large model. Making and analyzing larger models will increase the cost of simulations. On the other hand, it should be verified that the current aspect ratio of finite elements does not spoil the accuracy of analysis. Especially, this aspect ratio might be problematic when the uniaxial loading is along T or TT directions, because in these cases, the largest dimension of finite elements is perpendicular to the loading direction. The following test simulations have been done for the purpose of estimating the accuracy of analysis when the mentioned finite elements are used.

Two 25×25×25 mm PSL models including actual voids taken from exactly the same location in the parent billet have been made. The difference between these two models is that the first model is made of 0.25×0.25×4.02 mm finite elements (called coarse elements), while the length of finite elements along L direction in the

second model is one third of that of first model; hence, the second model is made of 0.25×0.25×1.34 mm finite elements (called fine elements). The numbers of elements in the first and second models are respectively about 70000 and 210000.

Material elastic properties are based on the values of Table 3.1 and loading method and boundary conditions are the same as the ones displayed in Fig.3.1. Loading has been set to be a 1 mm compressive displacement (4% strain) along TT direction. The analysis is linear, therefore, there is no problem to apply the displacement in just one step.

Figures 3.2 and 3.3 show the distribution of normal and principal stresses in the two models under investigation. Also, the statistics of these stresses are listed in Table 3.2. The statistics imply that the model made of coarse elements is able to simulate the overall material's state of stress as accurate as the model made of fine elements, that is why the means, medians and standard deviations are very close. However, coarse elements cannot catch maximum local stresses that probably occur at the vicinity of large voids. This can be problematic especially in tensile nonlinear simulations where the material behavior is brittle. All in all, it is practical to accept the slight inaccuracy due to the failure to catch maximum local stresses and, instead, decrease the cost of analyses by using the coarse finite elements.

Table 3.2. Statistics of stresses in two models made of coarse and fine finite elements under compressive loading in TT direction (all values in MPa)

Stress	Coarse Elements			Fine Elements		
	Mean	Median	St. Dev.	Mean	Median	St. Dev.
σ_x	0	0.2	2.0	0	0.2	2.1
σ_y	-20.3	-22.8	8.6	-19.5	-21.9	8.9
σ_z	0	0.1	3.2	0	0	3.6
σ_1	1.3	0.8	2.5	1.4	0.8	3.0
σ_2	-0.9	-0.3	2.4	-0.9	-0.4	2.4
σ_3	-20.7	-23.0	8.2	-20.0	-22.2	8.6

3.4 Results of Analyses

3.4.1 Effective elastic moduli

All the simulations are uniaxial (i.e. the axial loading is applied just in one direction and the boundary conditions are selected such that the macroscopic state of stress is uniaxial). Therefore the effective elastic modulus (in the direction of loading) can be calculated by dividing the total stress induced at the base of the model by the total strain applied. Total stress equals sum of the base reactions over the total cross-sectional area. Having done these calculations, the resulting values of effective elastic moduli in L, T and TT directions in the models including actual voids are respectively 12700 MPa, 593 MPa and 536 MPa . The same properties in the models consisting of equivalent ellipsoids are equal to 12700 MPa, 535 MPa and 556 MPa (respectively 0, -9.8% and 3.7% difference). The replacement of ellipsoids does not cause a considerable change in the effective elastic modulus. Specifically, the elastic modulus in L direction (which is the largest and usually most important one) is less sensitive to the shape of the voids.

3.4.2 Reactions

Since the output of the software ADINA is going to be shown, it is necessary to mention the notation applied in the software. In ADINA the T, TT and L directions have been respectively addressed as the directions x, y and z. In all the figures which will be shown in the following sections, the ADINA notation has been used. The reaction forces induced at the constrained nodes covering the base of the model show substantial variabilities (Figs. 3.4, 3.5 and 3.6). For the loading in T (or x) direction, the coefficients of variation of reactions for actual and equivalent models are 32% and 30% respectively. When the model was loaded in TT (or y) direction, the coefficients of variation were higher than the corresponding values for T direction. They also do not properly match in actual and equivalent models. For actual model, COV is

52%, but for equivalent model it drops to 31%. The least variability and the most agreement between two void model was seen in the loading in L (or z) direction. The coefficients of variation are 13% and 12%. The interesting point is that all the histograms contain two peak points. The reason is not clear for the author. All in all, one can see an acceptable agreement between the distribution of reactions in the two void models.

3.4.3 Stresses

To address the questions of effect of void shape on stress concentration and multi-axiality, the corresponding normal stresses along the material directions, the principal stresses and the shear stresses should all be compared in the models of actual voids and equivalent ellipsoids. Each model is consisted of about 200000 finite elements, therefore the most appropriate way to study the stresses is to investigate the statistics of the element stresses. Each element's stress is calculated by taking the average over the same type stresses of all Gauss points within the element (8 Gauss point per element).

Figures 3.7, 3.8 and 3.9 show the distributions of normal stresses along the three material directions under the uniaxial compressive loading in T, TT and L directions respectively. The histograms on the left columns display the element stress distribution in the models of actual voids and the histograms on the right columns are the element stress distributions in the corresponding models of equivalent ellipsoids. Note that the loadings (in displacement form) in each direction have been applied such that they generate the same macroscopic strain. Because the elastic modulus in L direction is much higher than the elastic moduli in T and TT directions, σ_z induced under the loading in L (or z) direction is on average much higher than σ_x induced under the loading in T (or x) direction and σ_y induced under the loading in TT (or y) direction. Expectedly, the mean and median of normal stresses in the directions

other than the direction of loading are near zero, but the standard deviation is still considerable. When the models (both actual and equivalent) are loaded in T and TT directions, there are few elements that experience high stresses (i.e. in the same order of magnitude of the mean stress in the direction of loading) along the directions orthogonal to the loading direction. This issue is not evident when the loading is along L direction, because the elastic modulus (and consequently the induced stresses) in this direction is much higher than the ones in T and TT directions.

Comparing the stresses in actual models with equivalent models, the means and medians are very close but the maximum values differ. When the models are loaded in L and TT directions, the maximum values of all three normal stresses in actual models are larger than that of the equivalent models. But with the loading in T direction, the equivalent models experience larger maximum stresses. The reason of this bias is not currently clear. Instead of the maximum value which is a very sensitive measure, the 95th percentile would be a more consistent measure. Table 3.3 compares 95th percentile of the maximum principal stresses (σ_3) in actual and equivalent models for all three loading scenarios. The corresponding values seem sufficiently close.

Table 3.3. 95th percentile of the maximum principal stresses in actual and equivalent models for all three loading scenarios (all values in MPa)

Load Direction	95th percentile of σ_3	
	Actual	Equivalent
T	-7.22	-3.85
TT	-4.21	-5.21
L	-161.26	-161.75

The distributions of principal stresses in actual and equivalent models have been illustrated in Figs. 3.10, 3.11 and 3.12. In all six simulations, the distribution of major principal stress (σ_3) is almost similar to the distribution of the normal stress along the direction of loading. This fact shows that the stress multiaxiality at the tip of voids and equivalent ellipsoids is not that much to be able to influence the principal

stresses. Comparing the two representations of voids, the distributions of principal stresses look alike when the models are loaded in TT and L directions.But when the loading is along T direction the distributions of principal stresses do not follow the pattern observed under the other two loading scenarios. In this case, the maximums of principal stresses are strangely larger in equivalent models than that of the actual models. Table 3.3 showed that this problem is due to the sensitivity of maximum values of stresses and it will be solved if the 95th percentile of stresses are taken into consideration instead.

As Figs. 3.13, 3.14 and 3.15 display, the all three types of shear stresses calculated in the six simulations have been distributed about zero and their maximums are not large enough to be taken into consideration. The only exception is σ_{xy} in the equivalent model loaded in T direction the maximums of which are of the same order as the average of maximum normal stress (σ_x). All in all, one should not expect large shear stresses when PSL models are loaded uniaxially along the material directions.

The important statistical properties of the element stresses in both actual and equivalent models have been gathered in Tables 3.4, 3.5 and 3.6. In all six simulations, the means and medians of all types of stresses almost match. Under the loading in TT and L directions, the standard deviations of all types of stresses in actual models are larger than that of the equivalent models. This is the effect of the sharp void tips in actual models compared to the smooth tips of equivalent ellipsoids. But the strange case is the loading in T direction when the variability of the stresses in equivalent model is more than that of the actual model.

3.4.4 Stress multiaxiality factor

The stress multiaxiality factor can be calculated by the Equation 3.6 [37].

Table 3.4. Statistics of the element stresses when actual and equivalent models have been loaded in T direction (all values in MPa)

	Mean	Median	St. Dev.
Actual-σ_x	-8.29	-8.33	1.15
Equivalent-σ_x	-7.48	-7.71	2.25
Actual-σ_y	0	0.01	0.29
Equivalent-σ_y	0	0.03	0.62
Actual-σ_z	0	0	0.31
Equivalent-σ_z	0	0.01	0.60
Actual-τ_{xy}	0	0	0.29
Equivalent-τ_{xy}	0	-0.02	0.54
Actual-τ_{xz}	0	0	0.16
Equivalent-τ_{xz}	0	0	0.34
Actual-τ_{yz}	0	0	0.08
Equivalent-τ_{yz}	0	0	0.19
Actual-σ_1	0.12	0.06	0.29
Equivalent-σ_1	0.27	0.14	0.51
Actual-σ_2	-0.10	-0.03	0.31
Equivalent-σ_2	-0.19	-0.04	0.62
Actual-σ_3	-8.31	-8.34	1.09
Equivalent-σ_3	-7.56	-7.74	2.18

$$q = \frac{\sigma_v}{\sigma_h} \tag{3.6}$$

where σ_v and σ_h are Von Mises (or effective) and hydrostatic stresses respectively defined by the following equations:

$$\sigma_v = \frac{1}{\sqrt{2}}\{(\sigma_1 - \sigma_2)^2 + (\sigma_1 - \sigma_3)^2 + (\sigma_2 - \sigma_3)^2\}^{\frac{1}{2}} \tag{3.7}$$

$$\sigma_h = \frac{\sigma_1 + \sigma_2 + \sigma_3}{3} \tag{3.8}$$

Based on equation 3.6, when an element is under uniaxial tension, q=3, while under uniaxial compression q=-3. Under hydrostatic stress q=0 and under uniform

Table 3.5. Statistics of the element stresses when actual and equivalent models have been loaded in TT direction (all values in MPa)

	Mean	Median	St. Dev.
Actual-σ_x	0	0.02	0.53
Equivalent-σ_x	0	0.04	0.46
Actual-σ_y	-7.58	-7.67	2.18
Equivalent-σ_y	-7.85	-7.97	1.89
Actual-σ_z	0	0.02	0.69
Equivalent-σ_z	0	0.01	0.33
Actual-τ_{xy}	0	-0.01	0.52
Equivalent-τ_{xy}	0	-0.03	0.45
Actual-τ_{xz}	0	0	0.18
Equivalent-τ_{xz}	0	0.01	0.13
Actual-τ_{yz}	0	0	0.32
Equivalent-τ_{yz}	0	0	0.22
Actual-σ_1	0.24	0.11	0.55
Equivalent-σ_1	0.19	0.12	0.34
Actual-σ_2	-0.16	-0.02	0.62
Equivalent-σ_2	-0.15	-0.02	0.42
Actual-σ_3	-7.65	-7.68	2.09
Equivalent-σ_3	-7.89	-7.98	1.84

torsion q approaches the infinity [37]. This factor has been used in [37] to find the least resistant part of material around a crack tip and find the most probable crack propagation path. In this study, the attention is on the possibility of production of stresses in the directions other than the direction of loading. Figure 3.16 shows the distributions of multiaxialty factors within the elements in the actual and equivalent models with the uniaxial compressive loadings in three material directions. In all simulations, the majority of elements experience a uniaxial compressive stress accompanied with much smaller normal and shear stresses of other types. With the loading in T and TT directions, the values of multiaxiality factor in a few elements are very high (i.e. orders of magnitude larger than the uniaxial tensile value of 3) , it means that the shear stresses are the controlling stresses in these elements. Since there are not many of these elements, one can conclude that the controlling stress state in both actual and equivalent models under all three types of loading is uniaxial

Table 3.6. Statistics of the element stresses when actual and equivalent models have been loaded in L direction (all values in MPa)

	Mean	Median	St. Dev.
Actual-σ_x	0	0	0.28
Equivalent-σ_x	0	0	0.18
Actual-σ_y	0	0	0.28
Equivalent-σ_y	0	0	0.18
Actual-σ_z	-169.41	-170.21	9.87
Equivalent-σ_z	-169.94	-170.21	6.17
Actual-τ_{xy}	0	0	0.11
Equivalent-τ_{xy}	0	0	0.08
Actual-τ_{xz}	0	-0.03	1.24
Equivalent-τ_{xz}	0	-0.04	1.01
Actual-τ_{yz}	0	-0.01	1.13
Equivalent-τ_{yz}	0	0	0.90
Actual-σ_1	0.13	0.05	0.41
Equivalent-σ_1	0.10	0.04	0.21
Actual-σ_2	-0.11	-0.04	0.26
Equivalent-σ_2	-0.09	-0.05	0.14
Actual-σ_3	-169.43	-170.21	9.46
Equivalent-σ_3	-169.95	-170.21	6.16

and the stress multiaxiality is negligible. It is important not to mix up the question of multiaxiality with the question of stress concentration. The stress concentration (here we are talking about the stress along the direction of loading) at the tip of the actual voids is still an existing issue (based on what was observed in previous section) and the ellipsoidal replacement can not fully simulate it.

Because of the variation of the material strength along the different directions of an orthotropic material, the stress multiaxiality factor is not able to provide a full insight about the problem of multiaxiality. Although the absolute value of the normal stress along the direction of loading in almost all of the elements is much more than the values of other stresses, the low strength of material in one of the directions other than the direction of loading may lead the failure to happen along that direction (here "failure" means that the stress-strength ratio overpasses 1).

To investigate this problem, the stress-strength ratios for all types of normal and shear stresses within the elements have been calculated to find out which stress would cause the first failure. Let us define the stress-strength ratio (SSR) by equation 3.9.

$$SSR_{ij} = \frac{\sigma_{ij}}{S_{ij}} \tag{3.9}$$

where i and j represent material directions x (or T), y (or TT) and z (or L); σ is the stress induced due to loading and S is strength (yield stress in case of compression) of material in a certain direction. For simplicity, in case of $i = j$, the subscript ii will be replaced by a single i.

Table 3.7 lists the values of strength of PSL strands (Southern Species group) in different material directions [4, 38, 21] and Table 3.8 shows the percentage of the failures occurred along each type of stress. In all simulations, more than 98% of the elements have failed along the direction of loading; therefore the multiaxiality is not a big issue in PSL. Even if the maxima of theses ratios (i.e. the maximum of all the maximum ratios within the elements which the maximum ratio in the whole model) happen to be in a direction other than the direction of loading (it may happen, because the tensile strengths in T and TT directions are very low), we predict that this failure will be local and can not cause the failure of the whole specimen. To show the credibility of this prediction, more investigation should be done on this issue using nonlinear analyses.

To sum up this chapter, linear analysis shows that ellipsoidal replacement of actual voids in numerical models of PSL does not affect the effective elastic modulus and stress state of the composite material under uniaxial loading in any material direction. However, because of the smooth shape of ellipsoids, the stress concentration at the tip of ellipsoids is less than that of the actual void tips. Also, no influential stress multiaxiality state has been detected in any of actual and equivalent void models under any defined loading scenario.

Table 3.7. Strength values of PSL strands in different material directions ($x = T$, $y = TT$, $z = L$)

Strength	Value
S_x in compression	6.2 MPa
S_x in tension	1.5 MPa
S_y in compression	6.2 MPa
S_y in tension	1.5 MPa
S_z in compression	53.5 MPa
S_z in tension	53.7 MPa
S_{xy}	9.2 MPa
S_{xz}	5.9 MPa
S_{yz}	9.2 MPa

Table 3.8. Likliehood that the maximum stress-strength ratio within the elements corresponds each type of stress (all values in percent)

	SSR_x	SSR_y	SSR_z	SSR_{xy}	SSR_{xz}	SSR_{yz}
Actual-Loaded in x	99.57	0.43	0	0	0	0
Equivalent-Loaded in x	98.08	1.65	0.02	0.04	0.20	0.01
Actual-Loaded in y	1.22	98.60	0.03	0.01	0.06	0.08
Equivalent-Loaded in y	0.93	98.92	0.04	0.02	0.03	0.06
Actual-Loaded in z	0.04	0.01	99.85	0	0.09	0.01
Equivalent-Loaded in z	0	0	99.99	0	0.01	0

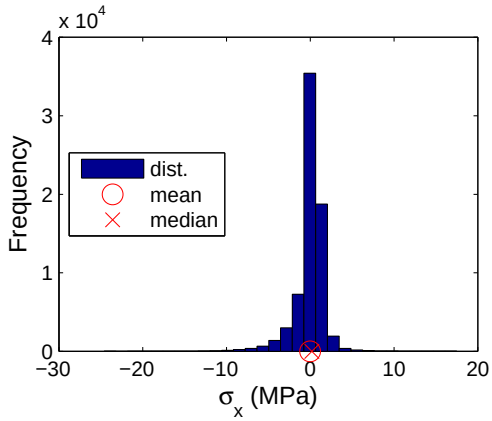

(a) σ_x in model made of coarse elements

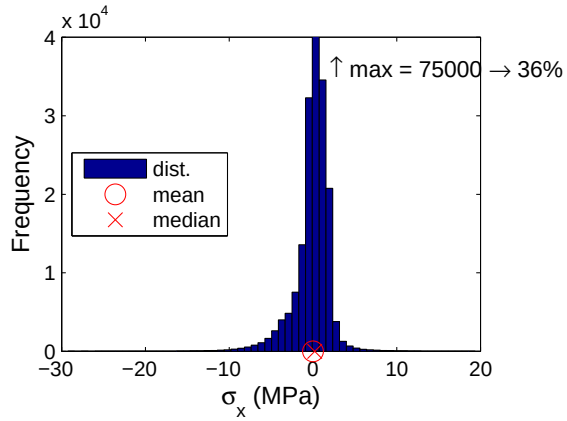

(b) σ_x in model made of fine elements

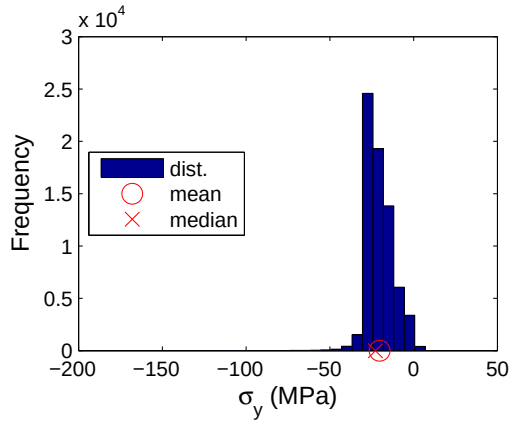

(c) σ_y in model made of coarse elements

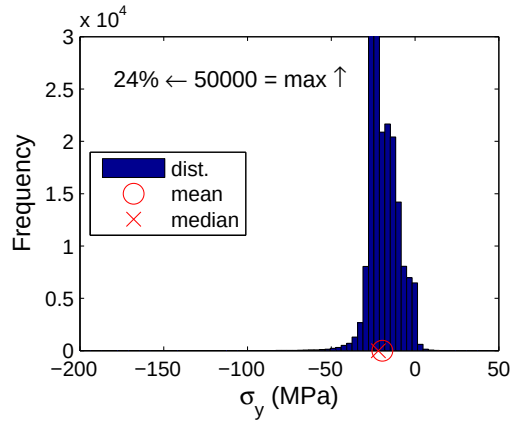

(d) σ_y in model made of fine elements

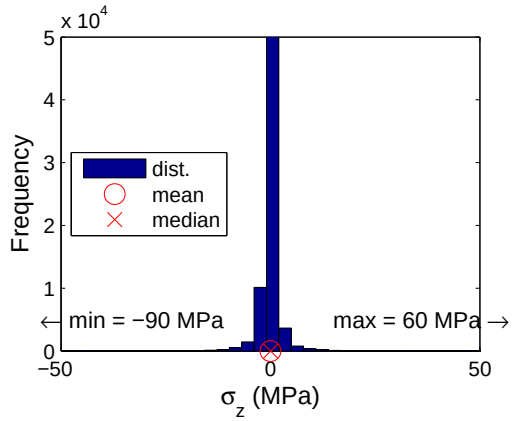

(e) σ_z in model made of coarse elements

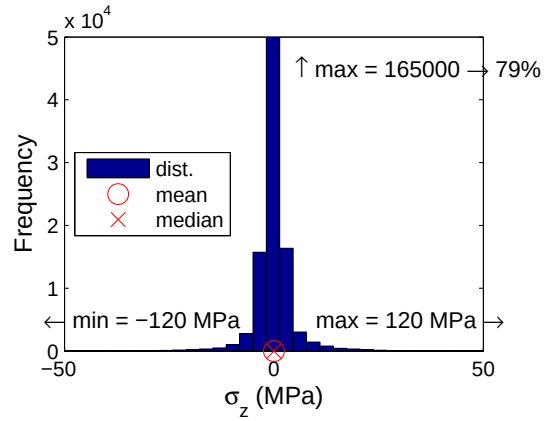

(f) σ_z in model made of fine elements

Figure 3.2. Distribution of the normal stresses in two models made of coarse and fine finite elements under compressive loading in TT direction

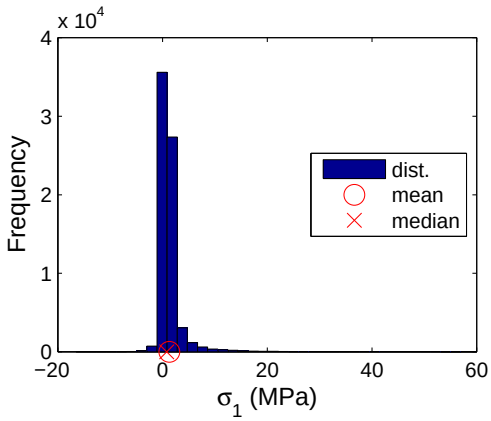

(a) σ_1 in model made of coarse elements

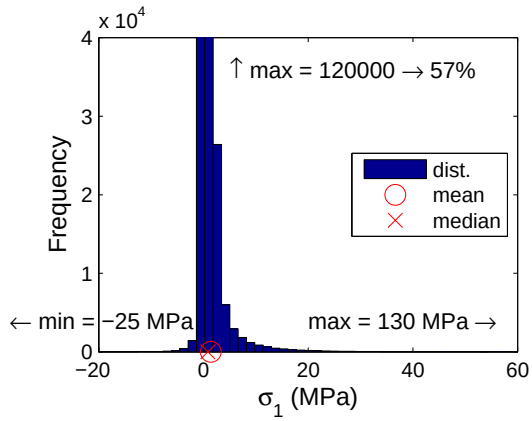

(b) σ_1 in model made of fine elements

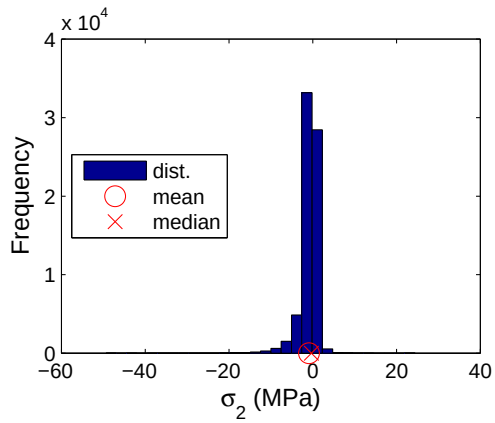

(c) σ_2 in model made of coarse elements

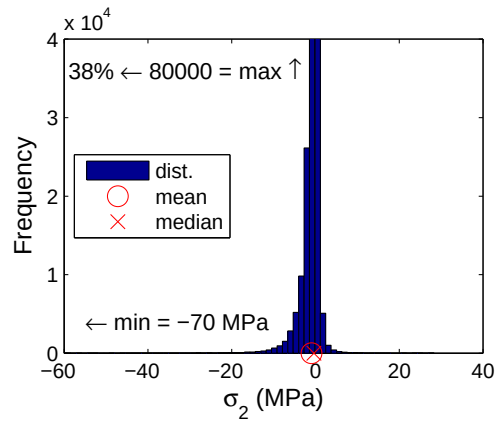

(d) σ_2 in model made of fine elements

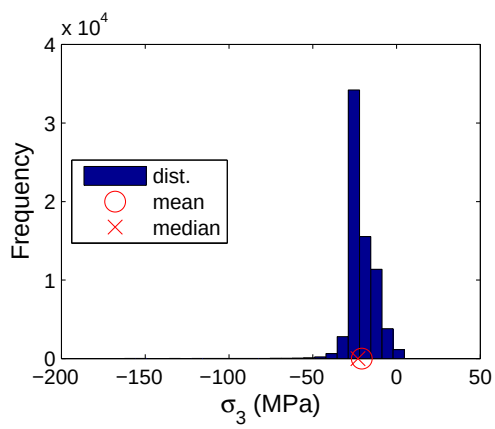

(e) σ_3 in model made of coarse elements

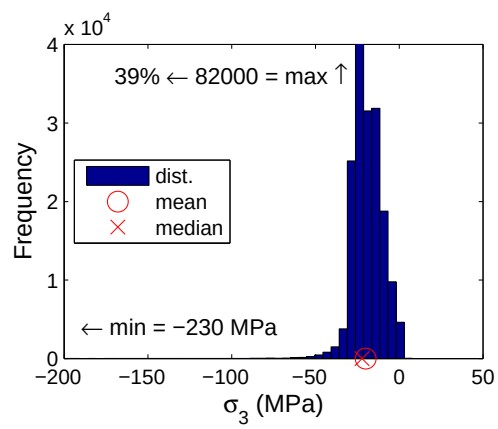

(f) σ_3 in model made of fine elements

Figure 3.3. Distribution of the principal stresses in two models made of coarse and fine finite elements under compressive loading in TT direction

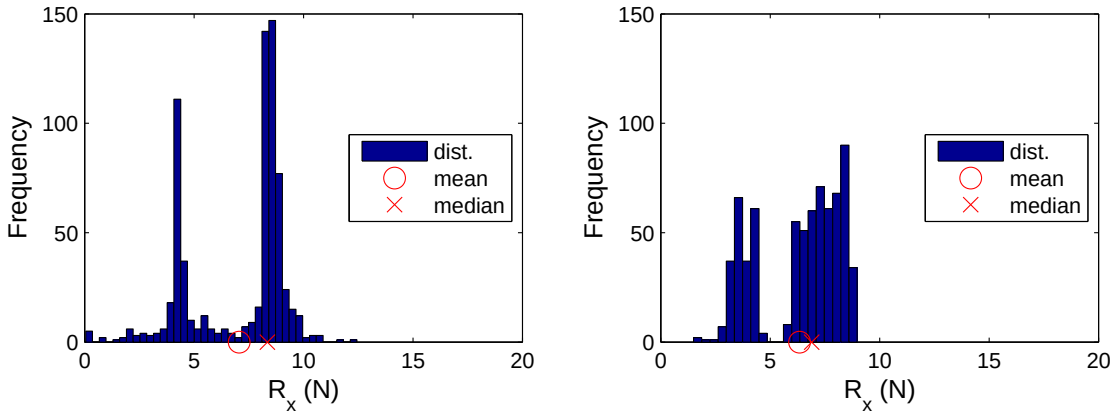

(a) model of actual voids

(b) model of equivalent ellipsoids

Figure 3.4. Distribution of the reaction forces in actual and equivalent models under the loading in T direction

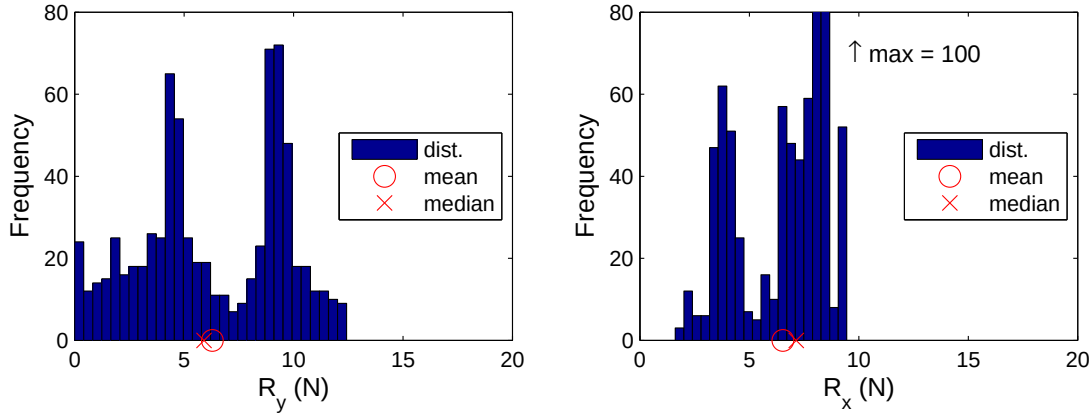

(a) model of actual voids

(b) model of equivalent ellipsoids

Figure 3.5. Distribution of the reaction forces in actual and equivalent models under the loading in TT direction

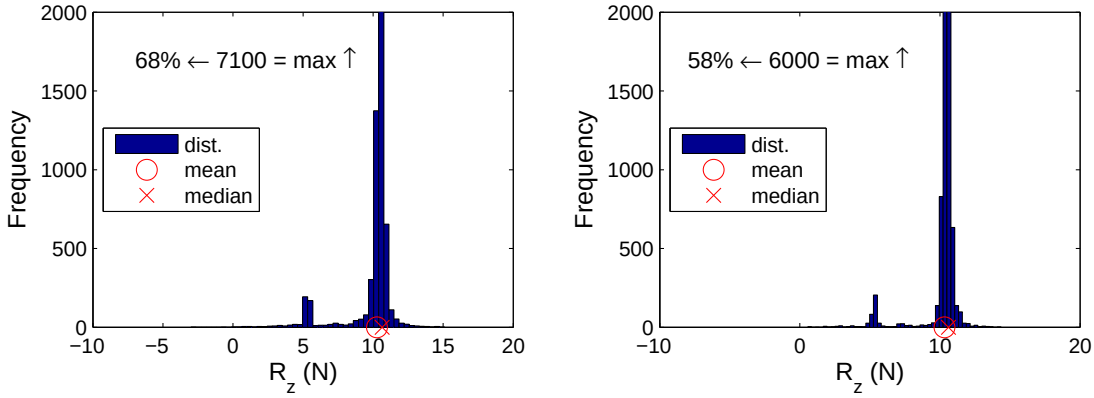

(a) model of actual voids

(b) model of equivalent ellipsoids

Figure 3.6. Distribution of the reaction forces in actual and equivalent models under the loading in L direction

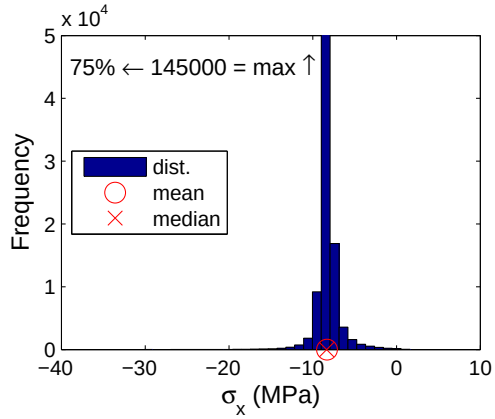

(a) σ_x in model of actual voids

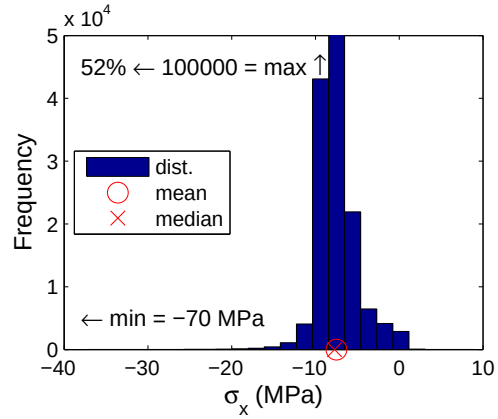

(b) σ_x in model of equivalent ellipsoids

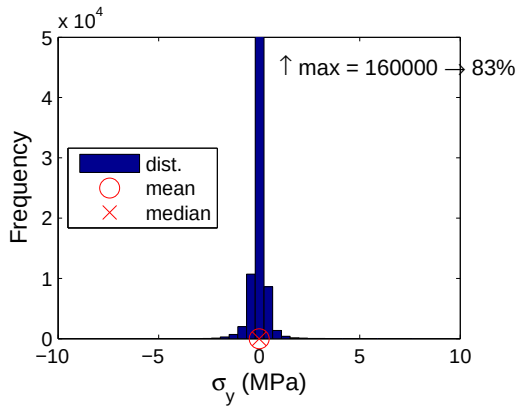

(c) σ_y in model of actual voids

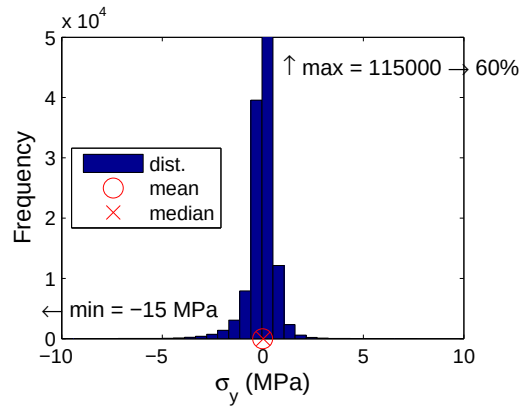

(d) σ_y in model of equivalent ellipsoids

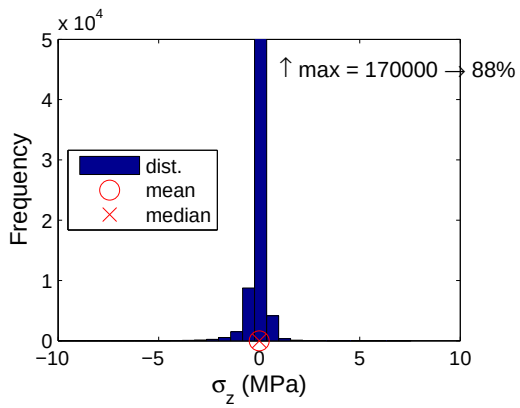

(e) σ_z in model of actual voids

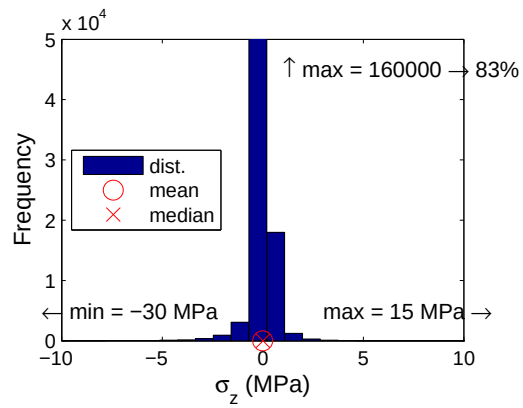

(f) σ_z in model of equivalent ellipsoids

Figure 3.7. Distribution of the normal stresses in actual and equivalent models under the loading in T direction

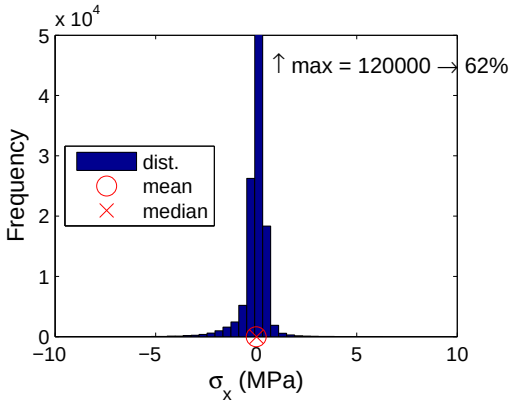

(a) σ_x in model of actual voids

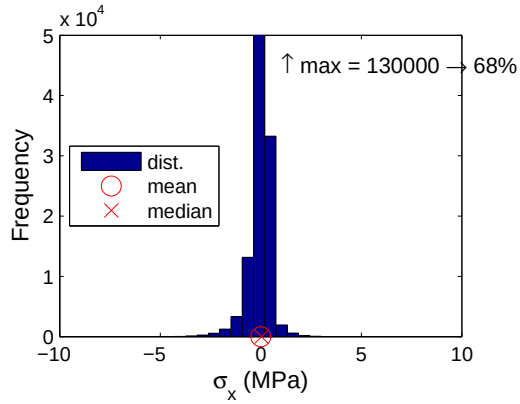

(b) σ_x in model of equivalent ellipsoids

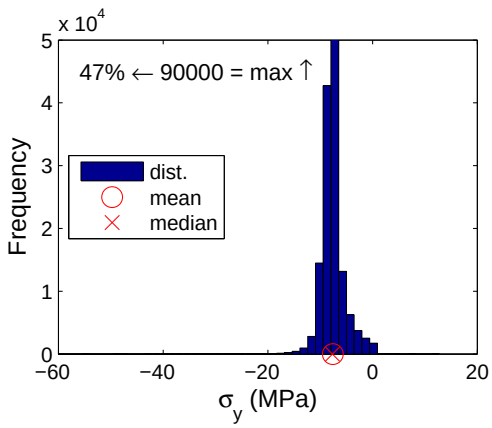

(c) σ_y in model of actual voids

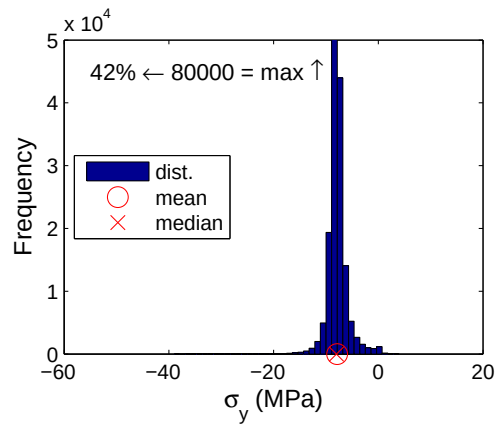

(d) σ_y in model of equivalent ellipsoids

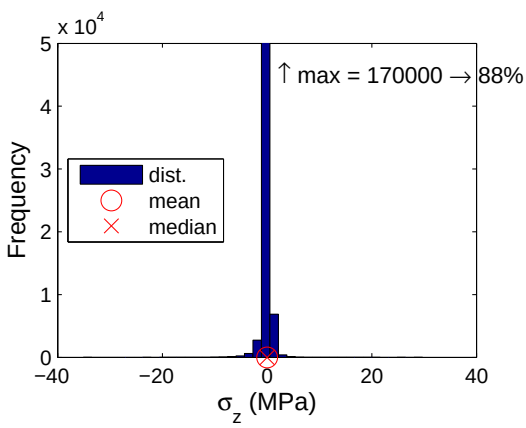

(e) σ_z in model of actual voids

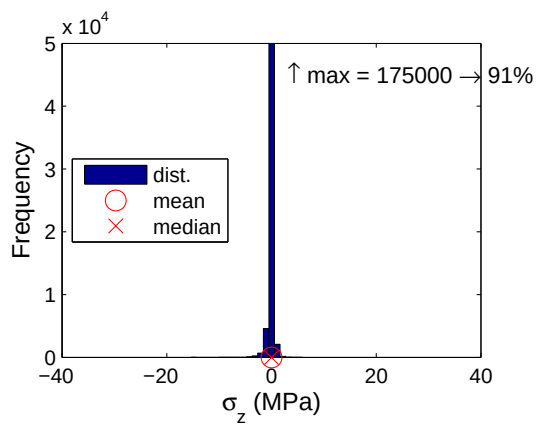

(f) σ_z in model of equivalent ellipsoids

Figure 3.8. Distribution of the normal stresses in actual and equivalent models under the loading in TT direction

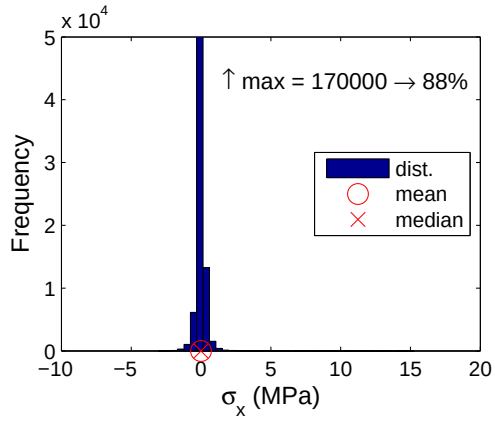

(a) σ_x in model of actual voids

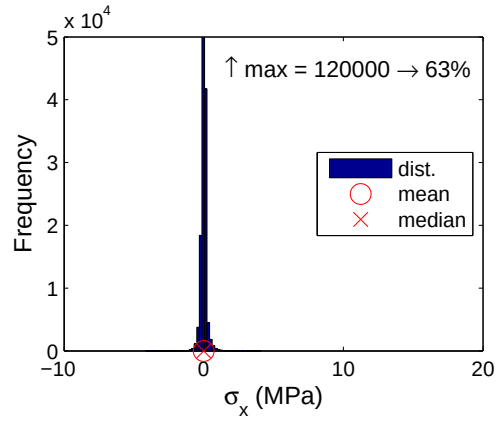

(b) σ_x in model of equivalent ellipsoids

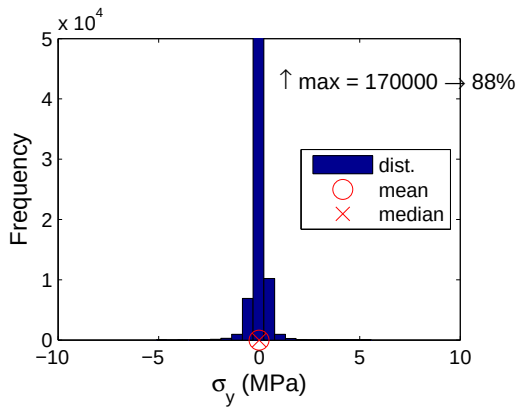

(c) σ_y in model of actual voids

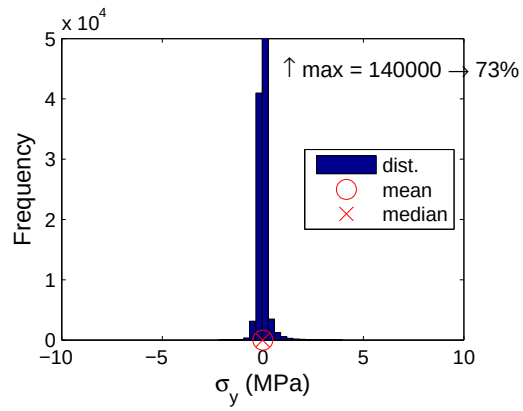

(d) σ_y in model of equivalent ellipsoids

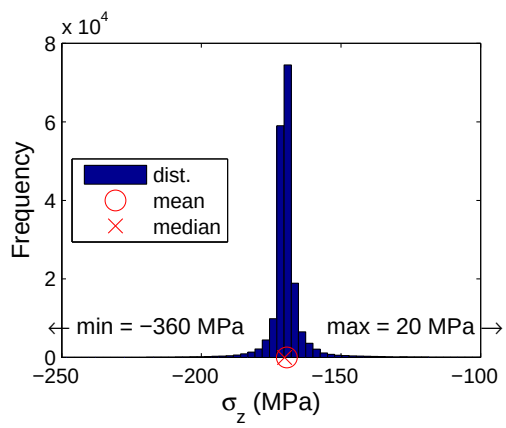

(e) σ_z in model of actual voids

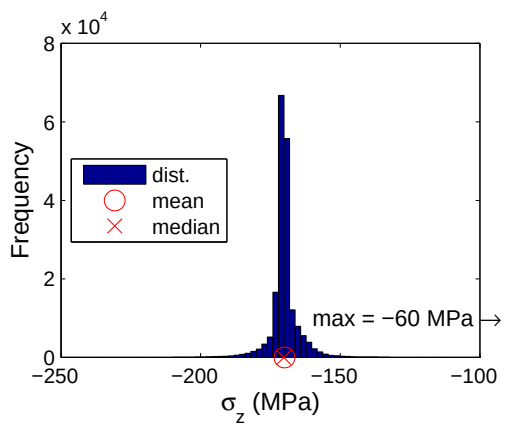

(f) σ_z in model of equivalent ellipsoids

Figure 3.9. Distribution of the normal stresses in actual and equivalent models under the loading in L direction

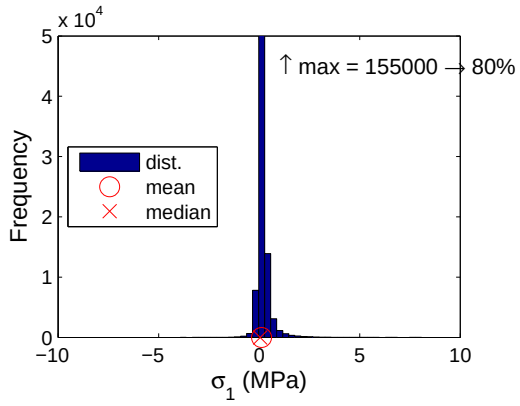

(a) σ_1 in model of actual voids

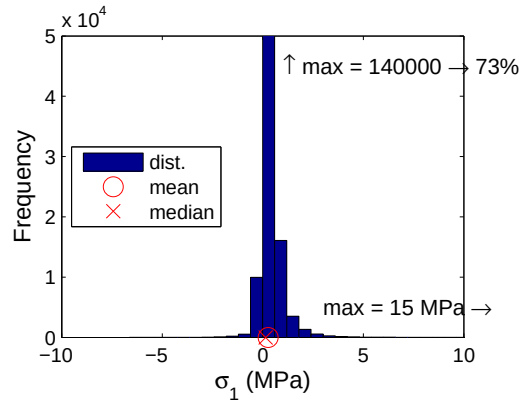

(b) σ_1 in model of equivalent ellipsoids

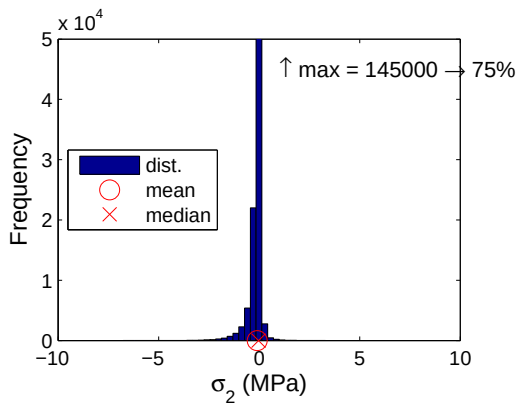

(c) σ_2 in model of actual voids

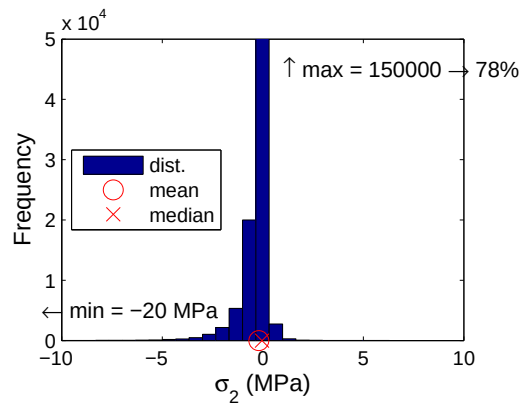

(d) σ_2 in model of equivalent ellipsoids

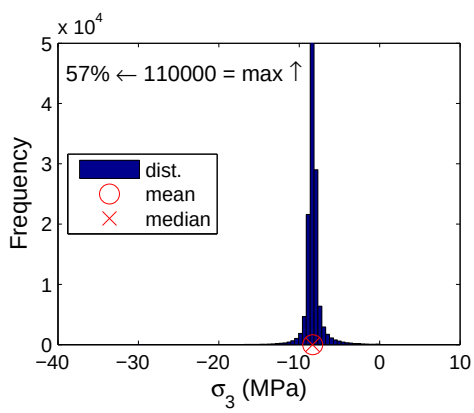

(e) σ_3 in model of actual voids

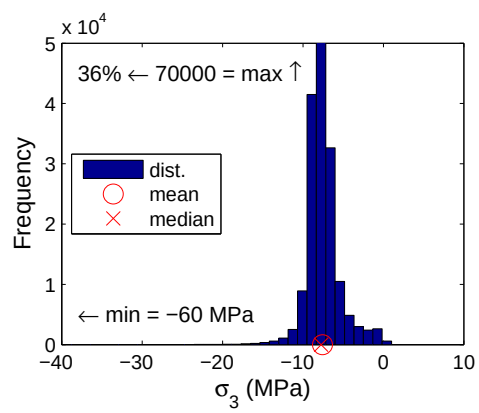

(f) σ_3 in model of equivalent ellipsoids

Figure 3.10. Distribution of the principal stresses in actual and equivalent models under the loading in T direction

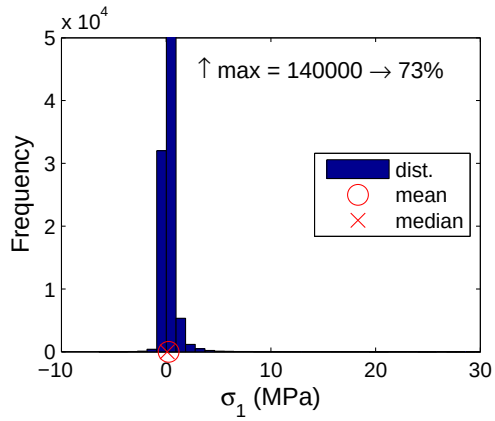

(a) σ_1 in model of actual voids

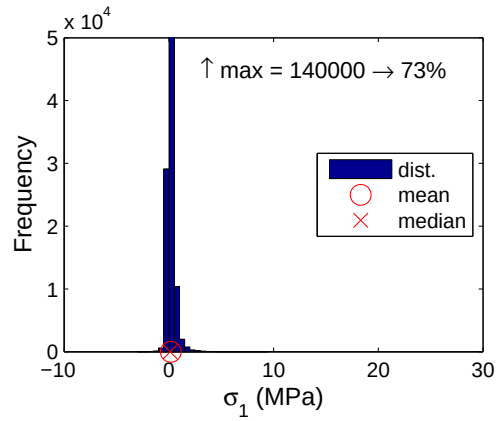

(b) σ_1 in model of equivalent ellipsoids

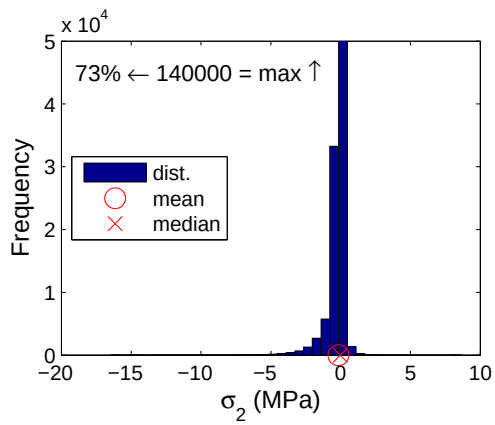

(c) σ_2 in model of actual voids

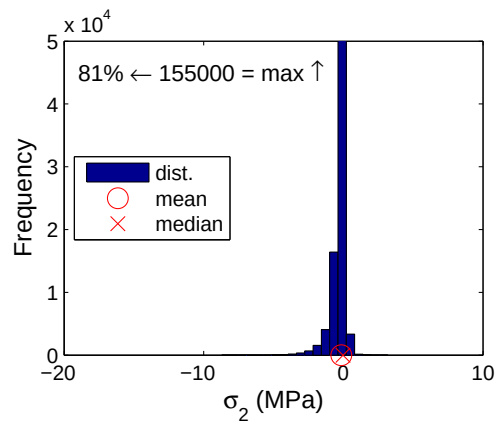

(d) σ_2 in model of equivalent ellipsoids

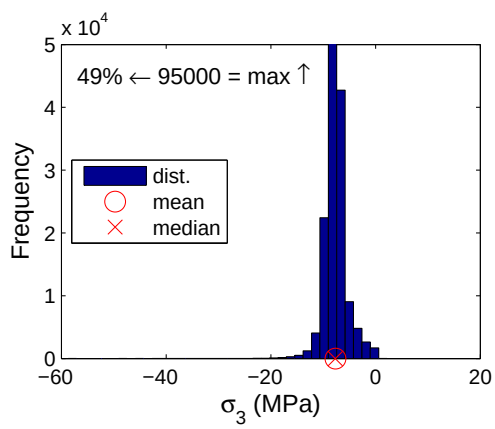

(e) σ_3 in model of actual voids

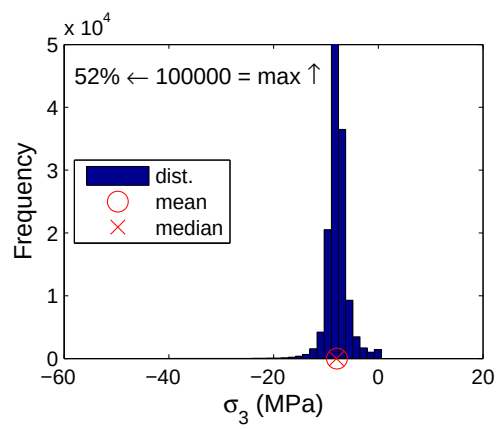

(f) σ_3 in model of equivalent ellipsoids

Figure 3.11. Distribution of the principal stresses in actual and equivalent models under the loading in TT direction

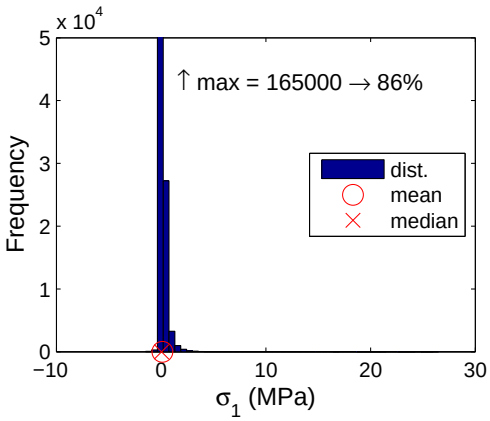

(a) σ_1 in model of actual voids

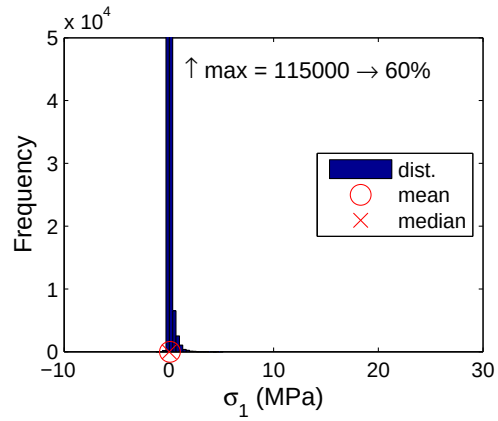

(b) σ_1 in model of equivalent ellipsoids

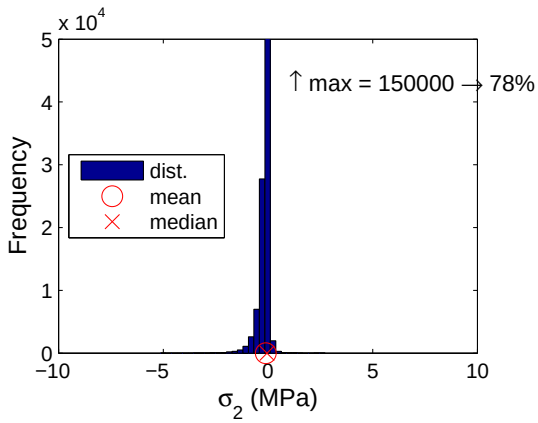

(c) σ_2 in model of actual voids

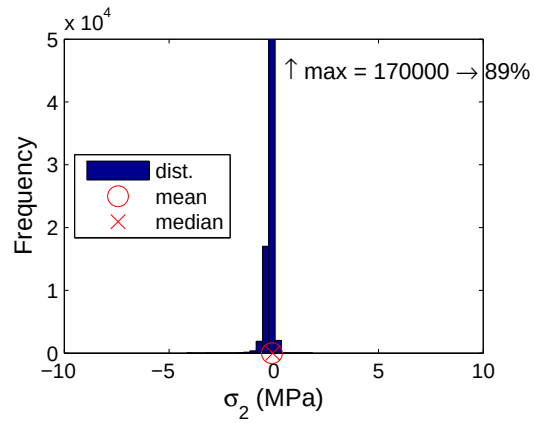

(d) σ_2 in model of equivalent ellipsoids

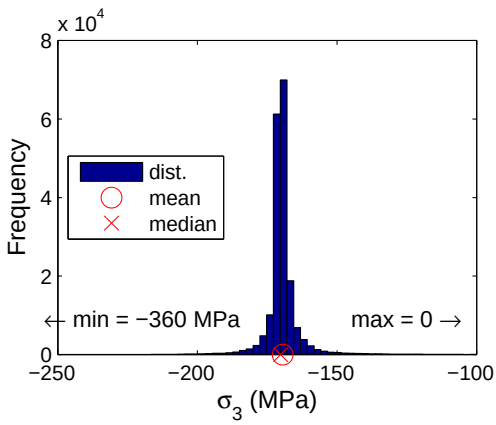

(e) σ_3 in model of actual voids

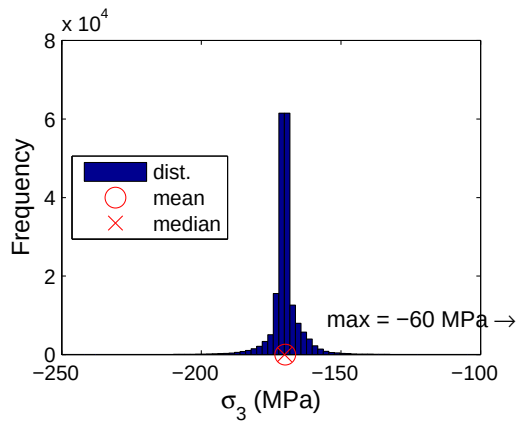

(f) σ_3 in model of equivalent ellipsoids

Figure 3.12. Distribution of the principal stresses in actual and equivalent models under the loading in L direction

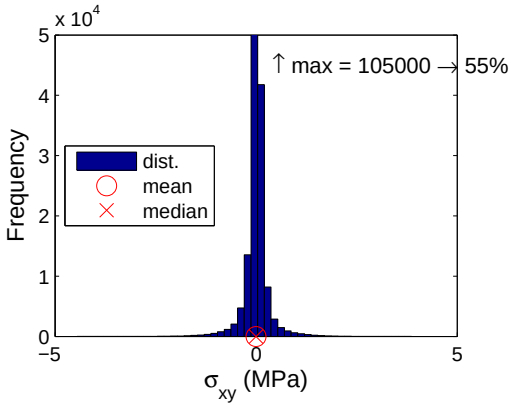

(a) σ_{xy} in model of actual voids

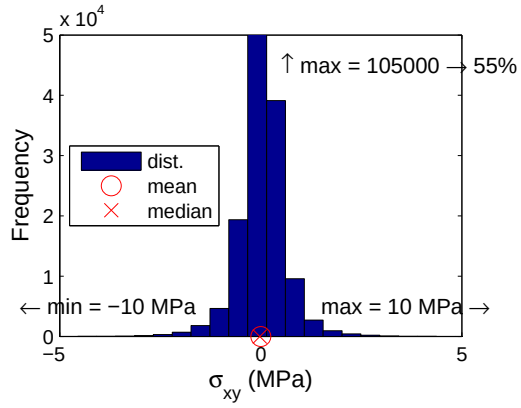

(b) σ_{xy} in model of equivalent ellipsoids

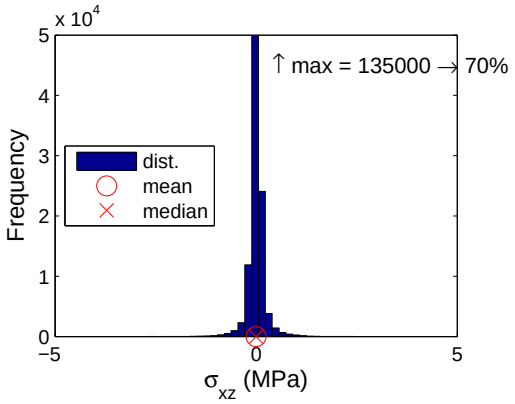

(c) σ_{xz} in model of actual voids

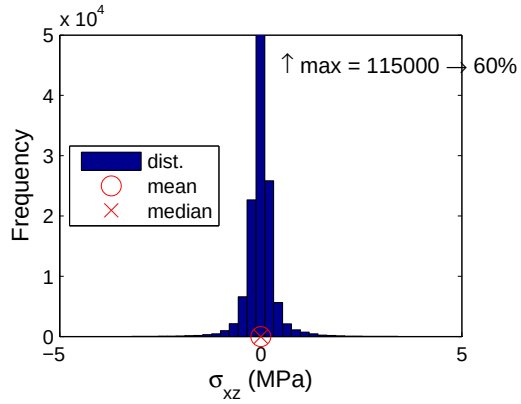

(d) σ_{xz} in model of equivalent ellipsoids

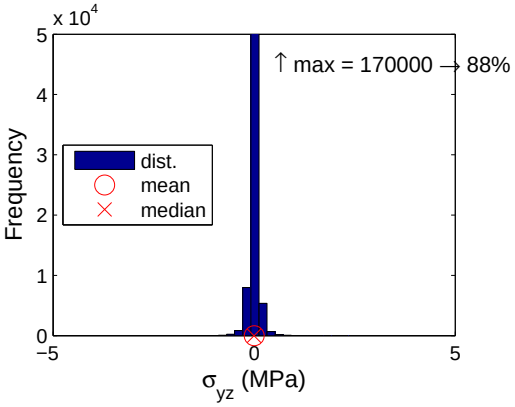

(e) σ_{yz} in model of actual voids

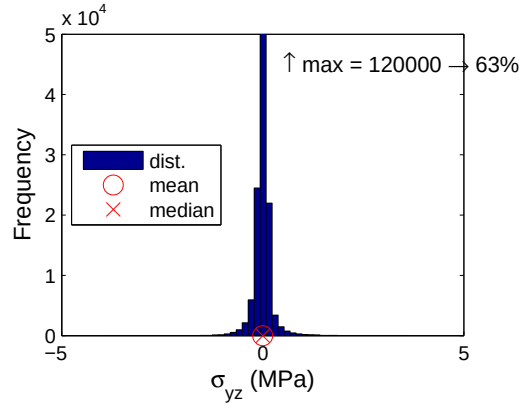

(f) σ_{yz} in model of equivalent ellipsoids

Figure 3.13. Distribution of the shear stresses in actual and equivalent models under the loading in T direction

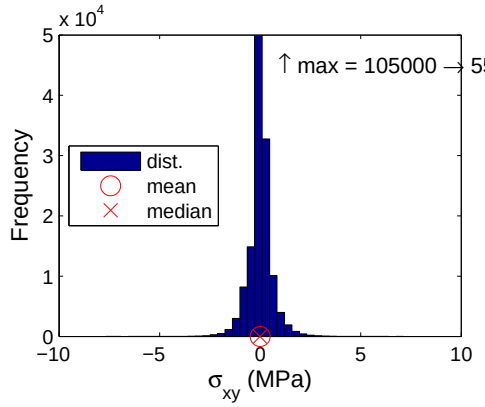

(a) σ_{xy} in model of actual voids

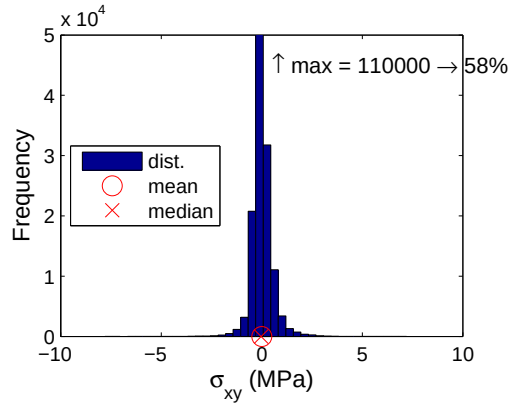

(b) σ_{xy} in model of equivalent ellipsoids

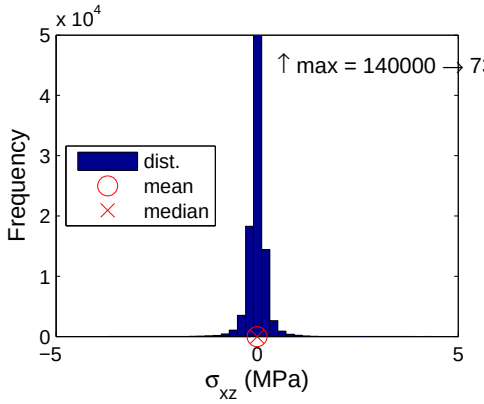

(c) σ_{xz} in model of actual voids

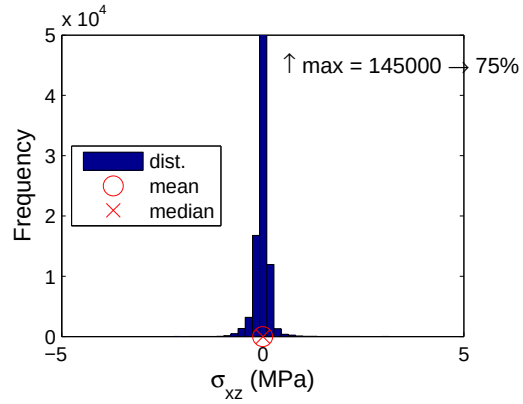

(d) σ_{xz} in model of equivalent ellipsoids

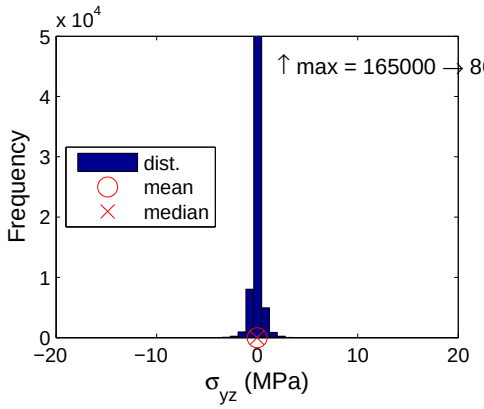

(e) σ_{yz} in model of actual voids

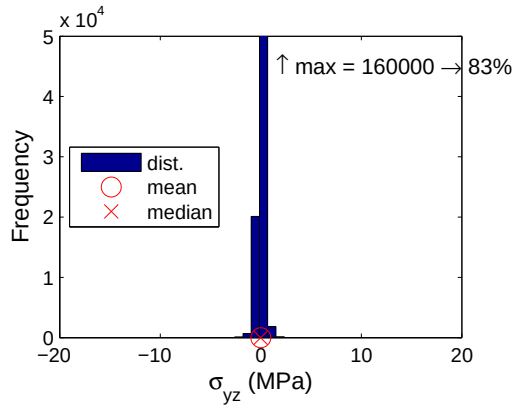

(f) σ_{yz} in model of equivalent ellipsoids

Figure 3.14. Distribution of the shear stresses in actual and equivalent models under the loading in TT direction

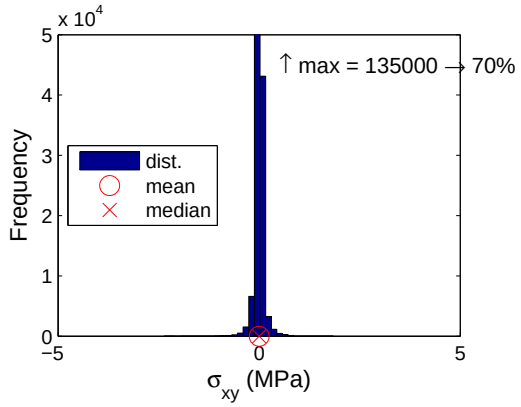

(a) σ_{xy} in model of actual voids

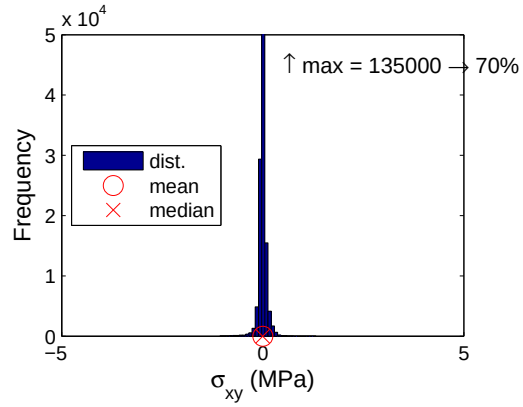

(b) σ_{xy} in model of equivalent ellipsoids

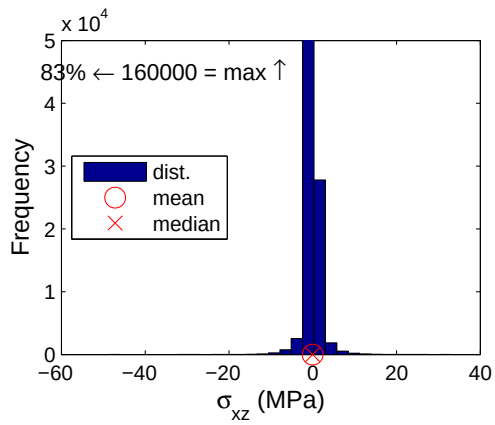

(c) σ_{xz} in model of actual voids

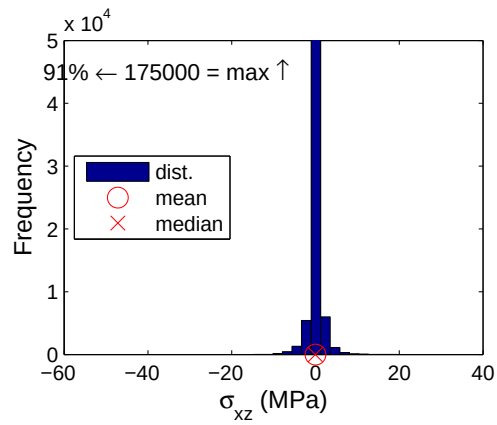

(d) σ_{xz} in model of equivalent ellipsoids

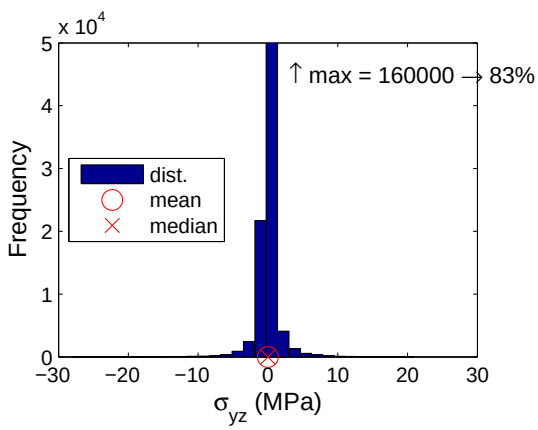

(e) σ_{yz} in model of actual voids

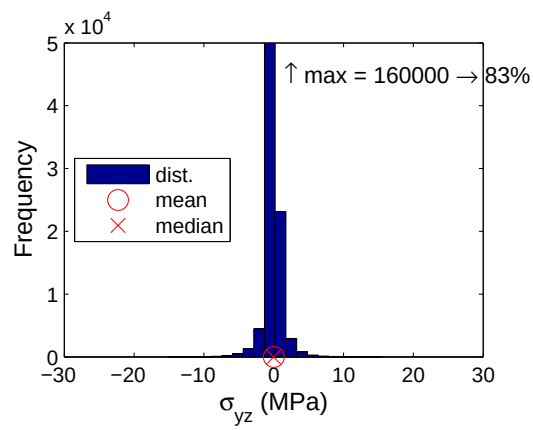

(f) σ_{yz} in model of equivalent ellipsoids

Figure 3.15. Distribution of the shear stresses in actual and equivalent models under the loading in L direction

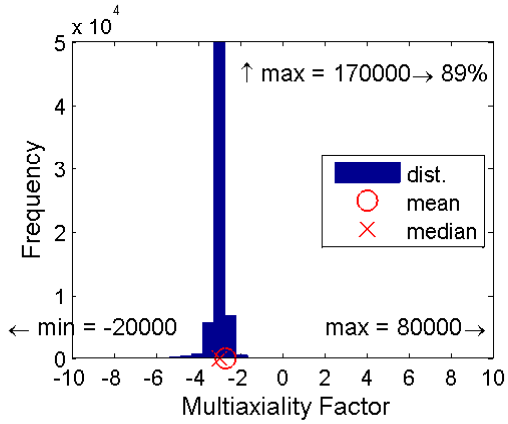

(a) model of actual voids loaded in T direction

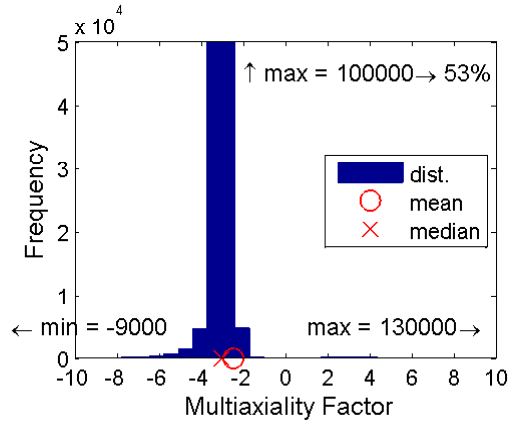

(b) model of equivalent ellipsoids loaded in T direction

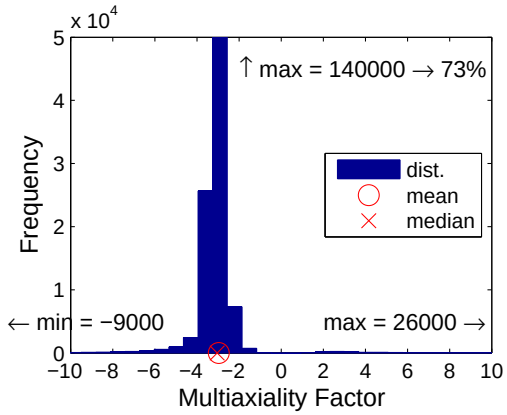

(c) model of actual voids loaded in TT direction

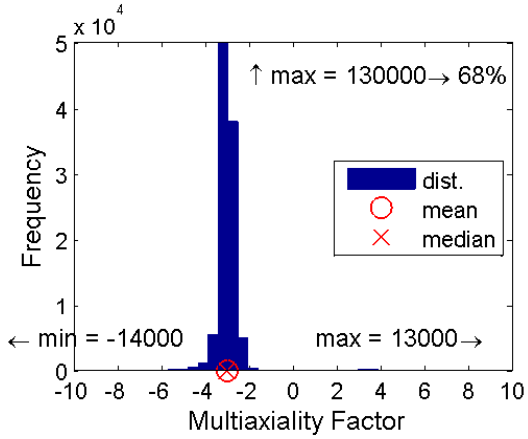

(d) model of equivalent ellipsoids loaded in TT direction

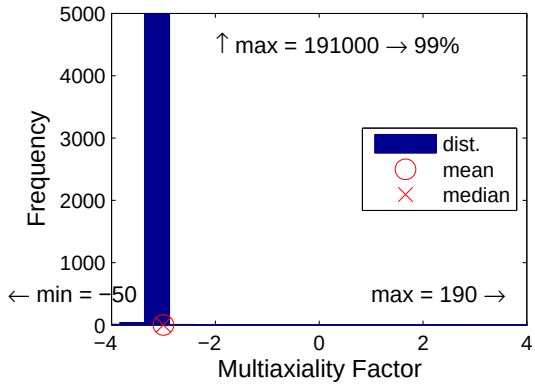

(e) model of actual voids loaded in L direction

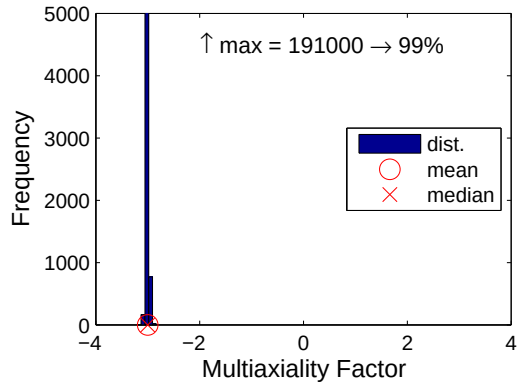

(f) model of equivalent ellipsoids loaded in L direction

Figure 3.16. Distribution of the stress multiaxiality factors in actual and equivalent models under the loading in three material directions

CHAPTER 4

STUDY OF THE EFFECT OF VOID SHAPE ON NONLINEAR COMPRESSIVE BEHAVIOR OF PSL

4.1 Problem Statement

Linear analyses showed that if the ellipsoids with the same volume and moments of inertia replace PSL actual voids, the stress distribution and effective modulus of elasticity of material will not change considerably (section 3.4). However, because of the smooth shape of ellipsoids, the stress concentration at the tip of ellipsoids is less than that of the actual void tips. Nonlinear analysis can show more completely how the replacement of actual voids with equivalent ellipsoids will affect the mechanics of PSL. Since the material shows different behavior under compression and tension, it has been decided to study the nonlinear behavior of material in two stages. The first stage which will be studied in this chapter is allocated to compressive behavior. In the next stage/chapter, we will focus on the nonlinear tensile behavior of material.

Some compressive tests have been done on PSL material by Winans [6, 7]. The tests provide measurement of elastic modulus and yield stress of PSL material merely in longitudinal direction. There is now a good opportunity to, first, calibrate the models that include actual voids or equivalent ellipsoids and certify that the constitutive model and properties selected for the material work satisfactorily, and second, compare the results of analysis of the models that contain virtually generated voids with the experimental results and validate the numerical results. Winans's tests have just covered the uniaxial longitudinal loading and there is no data available for the uniaxial loadings in transverse and thru thickness directions. To fill this gap, we tested

some PSL specimens under uniaxial compressive loading along T and TT directions and used the results to calibrate our simulation models.

For each void model (actual or equivalent) under each uniaxial loading scenario (3 uniaxial loadings in each material direction), 6 finite element models have been made and analyzed (3 pairs of corresponding actual and equivalent models have been taken from the same location in the parent billet and the other 3 pairs have been selected in a way that the void volume fractions match). Also, for each void model (actual or equivalent) under each biaxial loading scenario (3 biaxial loadings along each pair of material directions), 3 finite element models have been made and analyzed (the pairs of corresponding actual and equivalent models have been taken from the same location in the parent billet). Totally 54 simulations have been done in this stage of study.

It is good to define some terminology which will be used in this chapter. A scheme of the expected constitutive behavior of PSL material under compression is illustrated in Fig.4.1. This scheme is based on the hypothesis that PSL's constitutive behavior should not be very different from that of solid-sawn lumber. σ_c and ϵ_c represent compressive stress and compressive strain respectively. As shown in this figure, σ_{yield} and ϵ_{yield} are respectively the compressive stress and strain at which the material yields (switches from linear elastic phase with elastic modulus E to nonlinear plastic phase with varying plastic modulus). They are called "compressive yield stress" and "compressive yield strain" (since no yielding behavior is expected under tensile loading, they are simply called yield stress and yield strain). The maximum compressive stress which the material bears is called "compressive strength" or "compressive ultimate stress" and labeled by σ_u. The strain corresponding to the compressive ultimate stress is called "compressive ultimate strain" (ϵ_u). Note that this strain may be less than the maximum strain which the material experiences.

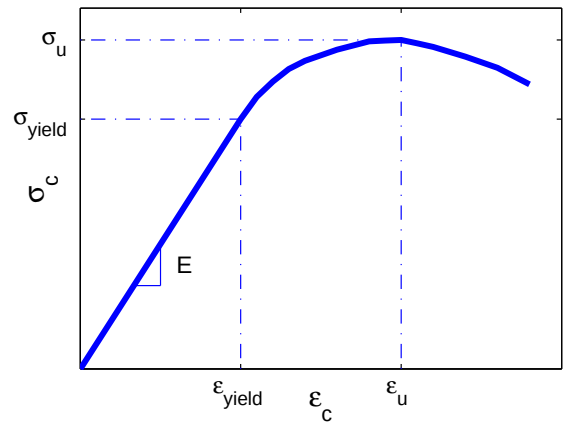

Figure 4.1. A Scheme of the expected stress-strain relationship of PSL material under compression

4.2 Experimental Approach

In 2008, Winans conducted experiments to measure the elastic modulus, compressive yield stress and compressive strength (which in his terminology means the maximum stress that the material can bear) of PSL in longitudinal direction [6, 7]. The tests were done on 25×25×76 mm PSL rectangular prism specimens the longest dimension of which was along the longitudinal direction. The loading was uniaxially compressive along longitudinal direction and displacement control. The results of this experiment are repeatedly used in the current investigation, but since the mentioned experiment did not cover the material properties in T and TT directions, we conducted another experiment, this time with compressive loading in T and TT directions separately, to complete the database of PSL compressive properties in all material directions. For each loading scenario, 6 tests have been done. The size of rectangular prism specimens is again 25×25×76 mm, but the specimens' longest dimensions are along the direction of loading (T or TT direction depending on the loading scenario). Figure 4.2 shows the test setup and its schematic illustration.

In this new displacement control experiment, the rate of cross-head displacement was 1.25 mm/min (for both loading directions) and an extensometer was used for

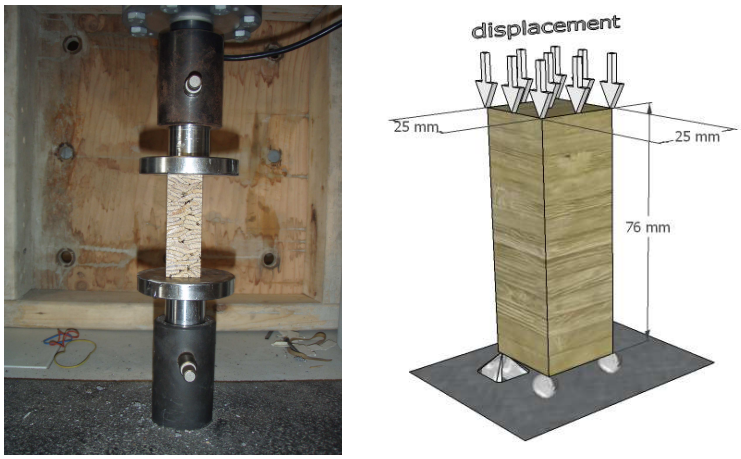

(a) test setup (b) schematic illustration of the test

Figure 4.2. Setup of the test conducted on 25×25×76 mm PSL specimens and its schematic illustration (notice: this photo had been taken before the extensometer was placed)

strain capture. Figures 4.3 and 4.4 illustrate the PSL specimens used for testing with loading in T and TT directions respectively before and after the test. If we assume that the crack follows the "weakest link" in the wood strands, the crack patterns in these figures show that the weakest link usually lies in the region between the closest voids to the specimen's longest edge and the longest edge. The second candidate for the weakest link is the region between two voids that are significantly larger than the other ones (if there are such voids in the specimen). In most cases the wood strands (not the adhesive) in the weakest link have been fractured. The interesting point is that the cracks do not usually traverse the shortest path between a void and the closest edge (i.e. the cracks are not usually perpendicular to the loading direction), instead, they usually make an acute angle with the loading direction.

The results of tests are displayed in Fig. 4.5. The effective elastic modulus in T direction (on average 325 MPa) is more than that of TT direction (on average 131 MPa). The average strengths (ultimate stresses) are almost equal in this two directions (5.5 MPa in T direction and 5.7 MPa in TT direction); but the standard

deviation of measured strengths is much more in TT direction (1.6 MPa comparing to 0.4 MPa). The most important difference is that there are strain softening and hardening phases when PSL is loaded in T direction; but when it is loaded in TT direction, the stress-strain relationship is almost bilinear. These results (also presented in Table4.1) will be used in simulations.

Table 4.1. Statistics of effective elastic modulus and compressive strength measured in the compressive tests

Measurements		Load Direction T	Load Direction TT
E_{eff}	Mean	325 MPa	131 MPa
	COV	17%	8%
σ_u	Mean	5.5 MPa	5.7 MPa
	COV	7%	28%

The last question about experiments is whether the compressive strength measured here is really due to plastic deformation or it has been caused by buckling. In other words, is the test output compressive strength or buckling critical stress (σ_{cr}) defined by equation 4.1?

$$\sigma_{cr} = \frac{P_{cr}}{A} = \frac{\pi^2 EI}{(KL)^2 A} \tag{4.1}$$

where P_{cr} is buckling critical load, A and I are column's cross sectional area and moment of inertia, E is material's elastic modulus, K is the effective length factor. In these tests, the gross area and moment of inertia of the specimens are $A = 625mm^2$, $I = 32552mm^4$; the measured elastic moduli are $E_T = 325MPa$ and $E_{TT} = 131MPa$; the length of each specimen is $L = 76mm$ and, assuming the pinned-pinned boundary condition (which is conservative), the effective length factor is $K = 1$. With these inputs, the buckling critical stresses will be $(\sigma_{cr})_T = 28.9MPa$ and $(\sigma_{cr})_{TT} = 11.7MPa$ for the cases of loading in T and TT directions respectively. These values are greater

than the maximum stresses measured in the tests. Hence, buckling is not an issue for our experiments and the test outputs are really compressive strengths.

4.3 Material Properties and Finite Element Modeling

Like the linear analysis, the PSL material model in nonlinear compressive analysis consists of two phases, wood and void. The wood phase is considered elastic-perfectly plastic and orthotropic with elastic moduli E_L=13000 MPa, E_T = 650 MPa and E_{TT}=650 MPa in L, T and TT directions respectively. Note that these properties are just related to the strands, not the whole composite. These values are the same as the values used in linear analysis and section 3.2 explains how these values have been selected. Of course, the experiment showed that the elastic modulus of whole composite, and consequently the elastic moduluds of wood strands, in T direction is larger than that of TT direction; but since the only objective of current simulations is to compare actual and equivalent void models, using identical values for E_T and E_{TT} will not cause any problem. Poisson's ratios are ν_{LT}=0.15, ν_{LTT}=0.15 and ν_{TTT}=0.09.

The wood phase in the numerical models is elastic-perfectly plastic, therefore the compressive strength of wood strands is considered equal to their yield stress. In the section 3.4, the strengths of wood strands in three material directions have been listed in Table 3.7. Identical compressive strength values (taken from Wood Handbook [4]) are used here as the strands' yield stress. Despite the fact that wood's yield stress is less than its compressive strength, it has been set equal to the compressive strength here, because in this study the wood medium is assumed continuum and therefore the yield stress specified in the model should represent the yielding behavior of the combination of narrow wood strands and adhesive (which has higher strength than wood).

Hill's failure criterion has been selected for plastic flow rule. This failure criterion is given by [1]:

$$f_{yield} = F(\sigma_{bb} - \sigma_{cc})^2 + G(\sigma_{cc} - \sigma_{aa})^2 + H(\sigma_{aa} - \sigma_{bb})^2 + 2L\sigma_{ab}^2 + 2M\sigma_{bc}^2 + 2N\sigma_{ac}^2 - 1 = 0 \tag{4.2}$$

where (a,b,c) are the material principal axes, and F, G, H, L, M, N are material constants given by:

$$F = \frac{1}{2}(\frac{1}{Y_{bb}^2} + \frac{1}{Y_{cc}^2} - \frac{1}{Y_{aa}^2}) \tag{4.3}$$

$$G = \frac{1}{2}(\frac{1}{Y_{cc}^2} + \frac{1}{Y_{aa}^2} - \frac{1}{Y_{bb}^2}) \tag{4.4}$$

$$H = \frac{1}{2}(\frac{1}{Y_{aa}^2} + \frac{1}{Y_{bb}^2} - \frac{1}{Y_{cc}^2}) \tag{4.5}$$

$$L = \frac{1}{2Y_{ab}^2} \tag{4.6}$$

$$M = \frac{1}{2Y_{bc}^2} \tag{4.7}$$

$$N = \frac{1}{2Y_{ac}^2} \tag{4.8}$$

where Y_{aa}, Y_{bb}, Y_{cc} are the yield stresses in the material directions a, b, c and Y_{ab}, Y_{ac}, Y_{bc} are the yield stresses for pure shear in the planes (a,b), (a,c), and (b,c).

Equation 4.2 is a quadratic expression of stresses that represents a governing energy for yielding of orthotropic materials. The Hill criterion is therefore considered

an extended form of distortion-energy criterion of von Mises. The most important difference between these two criteria is that the linear terms have been omitted in Hill's criterion to imply that a hydrostatic state of stress does not influence yielding [16]. It will be shown in section 4.4 that this failure criterion can simulate the plastic failure of PSL material favorably.

Two general loading scenarios have been utilized in this investigation. The first one is uniaxial compressive loading along each of the material directions (Fig. 3.1); and the second one is biaxial compressive loading along two material directions (Fig.4.6). The first loading scenario have been conducted for each of the three uniaxial loading cases separately on orthotropic 25×25×76 mm PSL models(the model's longest side is always along the direction of loading). They are displacement control with the total displacement of 1 mm (total strain of 1.3%). The second loading scenario has also three cases: loading in L+T, L+TT and T+TT directions. The size of models are 25×51×51 mm the two 51 mm dimensions of which are along two loading directions. In the case of loading along T or TT directions, the total applied displacement is 0.7 mm (1.4% total strain), but the applied total displacement in L direction is 0.4 mm (0.8% total strain). The reason of this difference is that the elastic modulus in L direction is much larger than that of T and TT directions and therefore a small strain in L direction can cause large stress. Also, uniaxial simulations and Winans's tests show that the yield and ultimate strains of PSL in L direction are smaller than that of other two directions.

Uniaxial compressive loading scenario is supposed to simulate the condition of PSL columns under gravity loads. This is a very common loading scenario that happens frequently in structures. Unlike uniaxial loading case, biaxial loading is rather rare (especially when both axial stresses in perpendicular directions are compressive), but important in PSL structural members due to their unequal strengths in different material directions. Biaxial state of stress is seen in beam-column connections when

the angle between beam and column is not 90° and therefore the load transfered from beam to column has two horizontal and vertical components (Fig.4.7(a)). The other possible case is when the beam connects eccentrically to a side of the column (Fig.4.7(b)). In this case, the connectors (such as bolts, screws or nails) that compress the beam to the column induce a horizontal stress in the column (that already bears vertical stress due to gravity loads). This horizontal stress is probably small comparing to the vertical stress due to gravity loads, but do not forget that the strength of PSL is also relatively small in that direction. In addition, the connectors may cause stress multixiality in their vicinity due to the combination of torsional and axial mechanisms. This can be another example for the biaxial state of stress.

The size of each 3D solid finite element is the same as the digital voxels, 0.25×0.25×4.02 mm in T,TT and L directions respectively. The investigation done on finite elements aspect ratio in section 3.3 showed that this element size is acceptable for the loadings in T and TT directions. No finite element has been allocated to the void phase.

The boundary conditions are only applied to the nodes at the base of each model. In all models, one of the base nodes is constrained along the three displacement directions and the other base nodes are just constrained along the direction of loading.

The size of PSL billet from which finite element models are taken is 110×120×600 mm. For each of the six loading cases (three uniaxial and three biaxial), three models of actual voids and three models of equivalent ellipsoids have been analyzed (totally 18 models for uniaxial loading and 18 models for biaxial loading, each pair of actual and equivalent models selected from similar positions in the big billet).

Because of the problem of outlier ellipsoids (which was explained in section 2.5), it was decided to compare two sets of actual and equivalent models. In the first set, the corresponding void and ellipsoid models (three models of each) are taken from exactly the same positions (above mentioned positions). In this case, the void volume fraction of corresponding models may differ. In the second set, actual and

equivalent models (three models of each) are taken from different positions, but their void volume fractions are similar.

4.4 Results of Analyses

4.4.1 Uniaxial loading

Remember that because of the problem of outlier ellipsoids (section 2.5), at the same position in the parent billet, the volume fraction of voids and equivalent ellipsoids are not equal. In this section, it will be tried to see whether the equivalent void model works the best when the locations of models are matched or when the volume fractions are matched.

Figures 4.8(a),4.9(a) and 4.10(a) help us to compare the behavior of actual and equivalent models taken from exactly identical positions in the parent billet. The positions of the lower left corner of the models used for the loading in T direction are $\times$:(X_T=2.5 mm, Y_{TT}=2.5 mm, Z_L=25 mm), $\bigcirc$:(X_T=13 mm, Y_{TT}=64 mm, Z_L=279 mm) and $\square$:(X_T=25 mm, Y_{TT}=48 mm, Z_L=533 mm) in the parent PSL billet. The void volume fractions in actual models are respectively 1.6%, 3.4% and 2.5%; while in equivalent models, they are 1.8%, 1.6% and 2.3%. In the models used for loading in TT direction, the position of the lower left corners are respectively $\times$:(X_T=5 mm, Y_{TT}=5 mm, Z_L=25 mm), $\bigcirc$:(X_T=51 mm, Y_{TT}=13 mm, Z_L=305 mm) and $\square$:(X_T=76 mm, Y_{TT}=25 mm, Z_L=508 mm). The void volume fractions in actual models are 2.8%, 2.8% and 4.2%; and in equivalent models are 2.4%, 1.9% and 2.7% respectively. And in the models used for loading in L direction, the position of the lower left corners are respectively $\times$:(X_T=0, Y_{TT}=0, Z_L=8 mm), $\bigcirc$:(X_T=51 mm, Y_{TT}=51 mm, Z_L=254 mm) and $\square$:(X_T=64 mm, Y_{TT}=64 mm, Z_L=457 mm). The void volume fractions are 0.9%, 2% and 2.6% in actual and 0.7%, 1.3% and 2.7% in equivalent models respectively.

On the other hand, Figs. 4.8(b),4.9(b),4.10(b) show the behavior of actual and equivalent models when the corresponding models have similar void volume fractions but are extracted from different locations in the parent billet. For loading in T direction, void volume fraction in $\times$, $\bigcirc$ and $\square$ models are respectively 1.6%, 1.8% and 2.4%. Loaded in TT direction, void volume fractions are 2.6%, 1.9% and 2.8% respectively. And finally, void volume fractions in the models loaded in L direction are respectively 0.8%, 1.3% and 2.7%.

The models have not calibrated yet to be compared to experimental results. Therefore, we just compare actual and equivalent models here and leave the comparison of simulation and experimental results to the after the calibration stage. All mean and standard deviation values presented here are based on three samples. They are probably not very accurate estimates, but still good for our purposes. As figure 5.5(c) illustrates, the behavior of actual and equivalent models loaded in L direction match favorably. Even when the void volume fractions of corresponding actual and equivalent models are very different (e.g. $\bigcirc$ models in Fig. 4.10(a)), the yield and ultimate stresses are sufficiently close to be assumed similar. When the corresponding models are compared based on position, the mean and standard deviation of the strength (ultimate stress) of actual models are 51.1 MPa and 0.8 MPa respectively; while the corresponding values of equivalent models are 51.8 MPa and 1.2 MPa. The behavior of models is almost elastic-perfectly plastic (just for loading in L direction); hence we can assume that yield stress is the point where two inclined and almost horizontal lines intersect. The mean and standard deviation of the yield stress in actual models are 50.3 MPa and 0.7 MPa, and in equivalent models, they are 51.4 MPa and 1.3 MPa. If we compare the models based on the void volume fraction, the mean yield stress and strength of actual models are 50.4 MPa and 51.2 MPa and their standard deviations are respectively 0.7 MPa and 0.8 MPa. For equivalent models, the corresponding values are respectively 51.4 MPa, 51.8 MPa, 1.3 MPa and 1.2 MPa. All

these values as well as the overall nonlinear behavior shown in Fig. 5.5(c) confirm that when the compressive loading is in L direction, ellipsoidal representation of voids is acceptable. This finding becomes more important when we consider the fact that PSL is usually designed to be loaded in L direction (because the strength of material in this direction is much more than that of the other two directions).

As for the loading in T and TT directions, the differences between the strength (and also yield stress) of corresponding actual and equivalent models is significant. The surprising point is that in the case of similar void volume fractions (Figs. 4.8(b) and 4.9(b)), the yield stresses and strengths of actual models are larger than that of equivalent models (there is just one exception: yield stress of $\times$ model in Fig. 4.9(b)). Even in some cases when the void volume fraction of actual model is higher than that of equivalent model, the strength of actual model is still higher ($\square$ models in Figs. 4.8(a) and 4.9(a)). This is not what we expected. It was expected that the smooth shape of ellipsoids led in lower stress concentration and consequently higher total strength; but the output was the other way around.

Loading in T direction and comparing based on void volume fraction, the mean and standard deviation of strength are 5.2 MPa and 0.1 MPa in actual models and 4.5 MPa and 0.5 MPa in equivalent models. The same statistical parameters for yield stresses are respectively 5.1 MPa, 0.2 MPa, 4.3 MPa and 0.5 MPa. There is about 15% difference between average yield stress and strength obtained from actual models and equivalent models. Also, the standard deviation (therefore the variability) of stresses is higher in equivalent models. But if the position of models are considered, the average values are much closer (However, it seems to be accidental). The mean yield stress and strength of actual models are both 4.6 MPa and their standard deviation are similarly 0.9 MPa. In equivalent models, mean yield stress is 4.3 MPa and mean strength is 4.5 MPa. Standard deviations are both 0.5 MPa. Note that for loading in

T and TT directions, the 0.2% offset yield strain method was used to calculate the yield stress of model [31].

Loading in TT direction and comparing based on void volume fraction,in actual models, average yield stress and strength are 4.3 MPa and 4.6 MPa and their corresponding standard deviations are 0.6 MPa and 0.5 MPa. The same statistical parameters in equivalent models are 4.0 MPa, 4.0 MPa, 0.6 MPa and 0.6 MPa. This is 15% difference in strength and 8% difference in yield stress. When the models are compared based on their position, the mean yield stress and strength in actual models are 3.8 MPa and 4.1 MPa, and in equivalent models are 4.0 MPa and 4.0 MPa. The corresponding standard deviations are respectively 0.4 MPa, 0.4 MPa, 0.6 MPa and 0.6 MPa.

Table 4.2 summarizes the analyses results about yield and ultimate stresses for all void models and loadings. So far, the effort was on the comparison of actual and equivalent models based on their position or void volume fraction. But the values presented in Table 4.2 invite us to compare the two void models in a slightly different way. Perhaps the void volume fraction is not as important as void shape and should be disregarded. No matter what the void volume fraction is, the average yield and ultimate stresses in corresponding equivalent models are the same. It seems to be better to disregard matching position or void volume fraction and compare the average of yield and ultimate stresses obtained from 6 actual and 6 equivalent models simulated under each loading scenario. In this way, the mean yield stresses in T direction for actual and equivalent models are respectively 4.9 MPa and 4.3 MPa (12% difference) and the mean ultimate stresses in the same direction are 4.9 MPa and 4.5 MPa (8% difference). In TT direction, actual and equivalent models have the mean yield stresses of 4.1 MPa and 4.0 MPa (2% difference) and the mean ultimate stresses of 4.4 MPa amd 4.0 MPa (9% difference). Finally, in L direction, the mean yield stresses in actual and equivalent models are 50.4 MPa and 51.4 MPa

(2% difference) and the mean ultimate stresses are 51.2 MPa and 51.8 MPa (1% difference). Except for the case of yield stress in T direction, all differences are less than 10% and considered small. The conclusion is that ellipsoids can be rather good replacements for actual void shapes in the models loaded uniaxially in compression.

Table 4.2. Mean yield and ultimate stresses of actual and equivalent models matched pair to pair based on position in the parent billet or void volume fraction under uniaxial compressive loadings in three material directions (All values in MPa)

Load Direction		same position		same void volume fraction	
		actual	equivalent	actual	equivalent
T	yield stress	4.6	4.3	5.1	4.3
	ultimate stress	4.6	4.5	5.2	4.5
TT	yield stress	3.8	4.0	4.3	4.0
	ultimate stress	4.1	4.0	4.6	4.0
L	yield stress	50.3	51.4	50.4	51.4
	ultimate stress	51.1	51.8	51.2	51.8

4.4.2 Biaxial loading

In this set of simulations, corresponding actual and equivalent models are categorized just based on their position. For loading along T+L directions, three pairs of actual and equivalent models have been taken from these positions: $\times$:(X_T=5 mm, Y_{TT}=5 mm, Z_L=25 mm), $\bigcirc$:(X_T=25 mm, Y_{TT}=51 mm, Z_L=229 mm), $\square$:(X_T=51 mm, Y_{TT}=76 mm, Z_L=533 mm). The void volume fractions in actual models are respectively 1.8%, 3.4% and 2.2%. In equivalent models they are respectively 3.7%, 2.6% and 1.7%. When loading is in TT+L directions, the positions are: $\times$:(X_T=5 mm, Y_{TT}=5 mm, Z_L=51 mm), $\bigcirc$:(X_T=51 mm, Y_{TT}=25 mm, Z_L=279 mm), $\square$:(X_T=76 mm, Y_{TT}=51 mm, Z_L=533 mm). Actual models contain 0.9%, 1.8% and 2.6% void; while their corresponding equivalent models contain 0.8%, 1.6% and 1.1% void. As loads are applied in T+TT directions, models are taken from $\times$:(X_T=51 mm, Y_{TT}=51 mm, Z_L=521 mm), $\bigcirc$:(X_T=25 mm, Y_{TT}=25 mm, Z_L=229 mm), $\square$:(X_T=13 mm,

Y_{TT}=13 mm, Z_L=178 mm). Void volume fractions are 2.5%, 3.4% and 2.1% in actual models and 1%, 1.7% and 1% in equivalent models.

The results of simulations under biaxial loading are very interesting. For the first time in the analytical part of this research on PSL we saw softening behavior (Figs. 4.11(a) and 4.12(a)). The material (wood strands) constitutive model is still elastic-perfectly plastic. Since no softening behavior has been seen in uniaxial simulations, the cause of softening is most probably the interaction of stresses (Poisson's effect). When the model is loaded biaxially in L-T or L-TT directions, the induced stresses in L direction are much larger than the stresses in the perpendicular directions. Also the Poisson's ratios in L-T and L-TT planes are rather large (0.15). Therefore, the longitudinal axial stress interacts with the axial stress in T or TT direction (based on the direction of loading), causes the reduction in the ultimate stress of PSL material in T or TT direction and results in softening.

The other considerable point about biaxial loading is that except for the ○ case in T+L loading, the difference in behavior between actual and equivalent models is really negligible (Figs. 4.11, 4.12, 4.13). Note that void volume fractions are different and even more consistency is expected for the same fractions. One can safely replace an actual model with the corresponding equivalent model and get sufficiently precise results under biaxial loading.

Another interesting point is that although the strands yield stresses (and strength) in T and TT directions are both 6.2 MPa and the material models are elastic-perfectly plastic, stresses induced by the loading in T+TT directions have reached 8 MPa and tend to increase if bigger displacement is applied (Fig. 4.13). It seems that Poisson's effect here acts positively and results in the strength increase.

Here is an explanation that why biaxial state of stress (and Poisson's effect) cause softening in the case of loading in T+L and TT+L directions, but hardening in the case of loading in T+TT directions. Consider Equation 4.2 in which directions a,

b, c are respectively X (or T), Y (or TT), Z (or L) directions. Y_{aa}, Y_{bb}, Y_{cc} have been assumed equal to S_x=6.2 MPa, S_Y=6.2 MPa, S_Z=53.3 MPa (Table 3.7). It was shown in section 3.4 that the stress multiaxiality is negligible if PSL is loaded uniaxially. Let us assume this finding also holds for the case of biaxial loading. Thus, under biaxial loading, all shearing stresses as well as the normal stress in the unloaded direction are zero. Loading in T+L directions, f_{yield} becomes:

$$f_{yield} = \frac{(\sigma_X^2 + \sigma_Z^2 - \sigma_X \sigma_Z)}{53.5^2} + \frac{(\sigma_X - \sigma_Z)^2}{6.2^2} - 1 \tag{4.9}$$

The first term in Equation 4.9 is much smaller than the second term (because it has a much larger denominator), so, let us drop the first term and assume:

$$f_{yield} = \frac{(\sigma_X - \sigma_Z)^2}{6.2^2} - 1 \tag{4.10}$$

With the same reasoning, if the model is loaded uniaxially in T direction, the approximate Hill's yield function will be:

$$f_{yield} = \frac{\sigma_X^2}{6.2^2} - 1 \tag{4.11}$$

Since E_L is 20 times of E_T, the change in σ_Z ($\Delta\sigma_Z$) in each loading step is much larger than the change in σ_X ($\Delta\sigma_X$). Remember that this analysis is displacement control and in fact, in each loading step, certain displacements are applied in T and L directions. Also, the applied displacements in L direction are always smaller than those in T direction, but not 20 times smaller, they are about half of the displacement steps in T direction. Hence:

$$\Delta\sigma_Z \approx 10\Delta\sigma_X \Rightarrow \Delta(\sigma_Z - \sigma_X) > \Delta\sigma_X \tag{4.12}$$

One can conclude from Equations 4.10,4.11 and 4.12 that in the case of biaxial loading in T+L directions, f_{yield} approaches zero much faster than it does in the case of uniaxial loading in T direction. Therefore, comparing these two loading scenarios, model's yield stress must be lower in T+L loading. Also, large value of $\Delta(\sigma_Z - \sigma_X)$ causes softening in the model.

On the other hand, under biaxial loading in T+TT direction, the approximate Hill's yield function is:

$$f_{yield} = \frac{(\sigma_X - \sigma_Y)^2}{6.2^2} - 1 \tag{4.13}$$

But equal displacement steps and elastic moduli in loading directions result in:

$$\Delta\sigma_X \approx \Delta\sigma_Y \Rightarrow \Delta(\sigma_X - \sigma_Y) < \Delta\sigma_X \tag{4.14}$$

Therefore, hardening is predictable in case of loading in T+TT directions, because the change in $\Delta(\sigma_X - \sigma_Y)$ is very small.

All in all, since: 1)the ellipsoidal replacement acts sufficiently good under the uniaxial loading in L direction (the most important loading scenario), 2) a proper consistency is seen between actual and equivalent models under biaxial loading, and 3) the material strength in T and TT directions is such low that even 15% difference of strength estimation means less than 1 MPa difference, we think that ellipsoids can replace actual arbitrary shapes of voids in modeling PSL under compression.

4.4.3 Calibration of model

Two material properties are important for uniaxial compressive loading in each material direction: elastic modulus and yield stress. Comparison of test and simulation results show that these two values have been properly chosen for L direction. The simulated behavior of PSL material shown in Fig. 5.5(c) matches Winans's test output. Therefore, the determined values for elastic modulus of strands, E_L=13000 MPa,

and yield stress of strands (also strength, because the material is elastic-perfectly plastic), S_L= 53.3 MPa, are acceptable. The mean yield stress and strain values of tested PSL specimens were calculated (using 0.2% offset yield point) in T and TT directions. In T direction, the mean yield stress is 3.44 MPa and mean yield strain is 0.0127. The corresponding values in TT direction are 3.16 MPa and 0.0260. To fit the experimental values, the following material properties were selected for simulations: E_T = 375 MPa, E_{TT} = 150 MPa, S_T = 5 MPa, S_{TT} = 5 MPa. Two separate simulations, one under the loading in T direction and another one under the loading in TT direction, have been conducted on 25×25×76 mm models with void volume fractions equal to the average void volume fraction of parent billet (2.5%). The simulation results have been shown in Fig 4.14. The curves fit properly to the experimental yield values. However, the strengths obtained from simulations in both directions are less than the tested strengths (5.5 MPa in T direction and 5.7 MPa in TT direction). Therefore, the models with strand properties presented in Table 4.3 can simulate the actual compressive behavior of PSL material in the working zone (i.e. linear zone). For nonlinear zone, hardening behavior should be added to the wood strands constitutive model.

Table 4.3. Calibrated values for wood strands' compressive properties in an elastic-perfectly plastic constitutive model

Property	Value
S_T	5 MPa
S_{TT}	5 MPa
S_L	53.5 MPa
S_{TTT}	9.2 MPa
S_{TL}	5.9 MPa
S_{TTL}	9.2 MPa
E_T	375 MPa
E_{TT}	150 MPa
E_L	13000 MPa
ν_{TTT}	0.09
ν_{TL}	0.15
ν_{TTL}	0.15

(k) before the test (l) after the test

Figure 4.3. Specimens used for uniaxial compressive test with loading in T direction

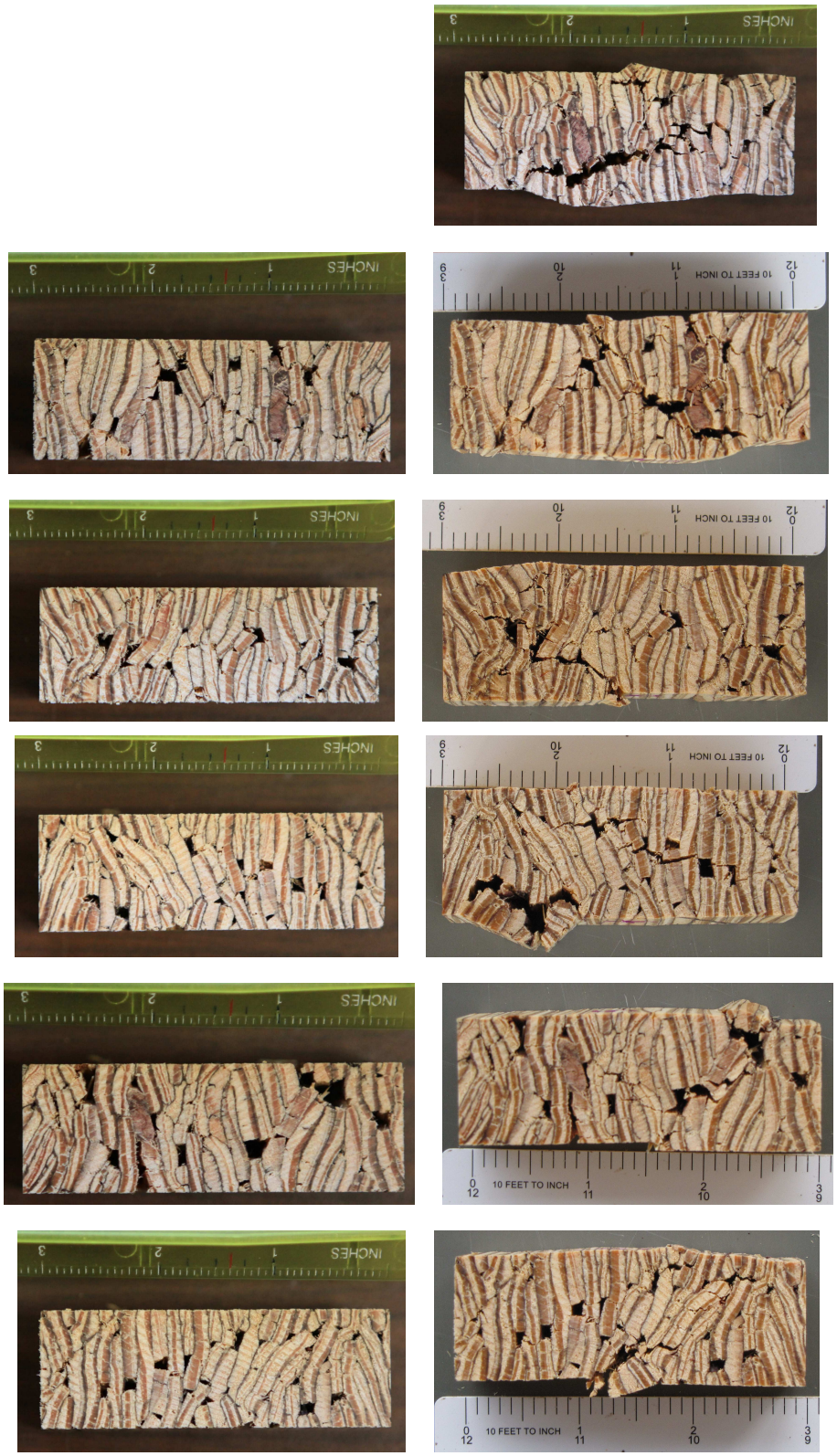

(k) before the test (l) after the test

Figure 4.4. Specimens used for uniaxial compressive test with loading in TT direction

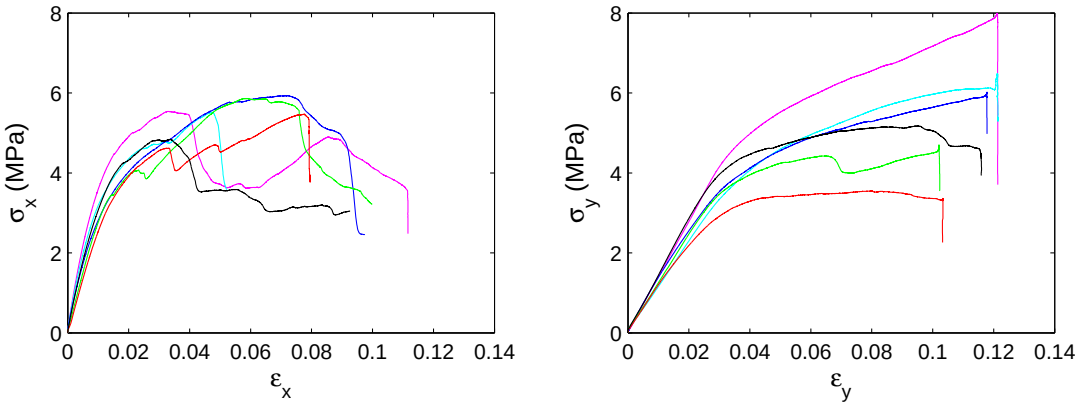

(a) Loading along T direction

(b) Loading along TT direction

Figure 4.5. PSL stress-strain relationship in T and TT directions obtained from uniaxial compressive tests

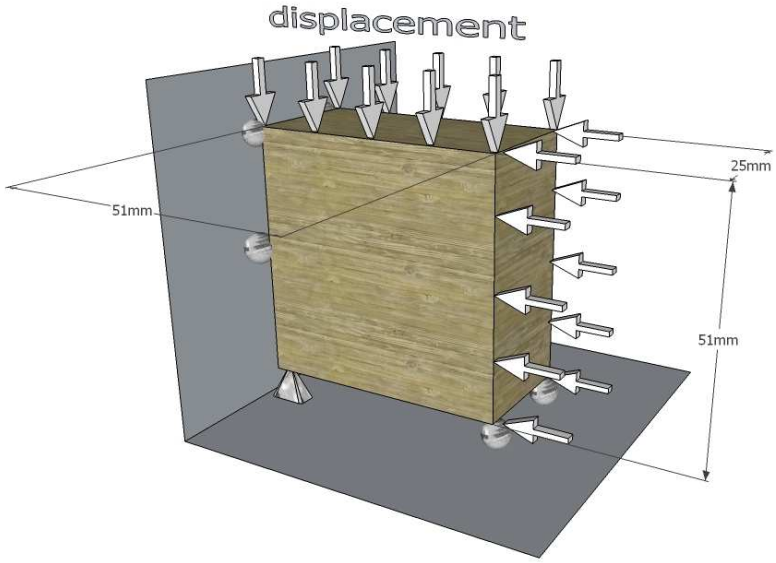

Figure 4.6. A schematic sketch of finite element models of PSL made for biaxial nonlinear compressive analyses

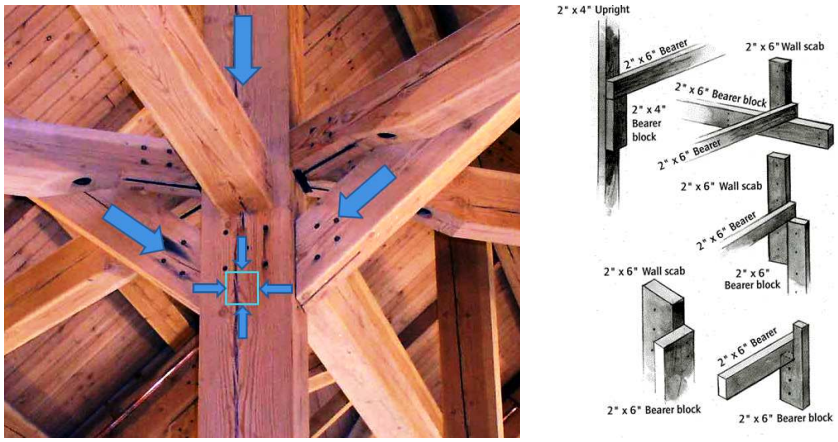

(a) (b)

Figure 4.7. Examples of biaxial state of stress at the position of connection of a beam to a column (Source: www.sefikbeydoner.com/wp-content/uploads)

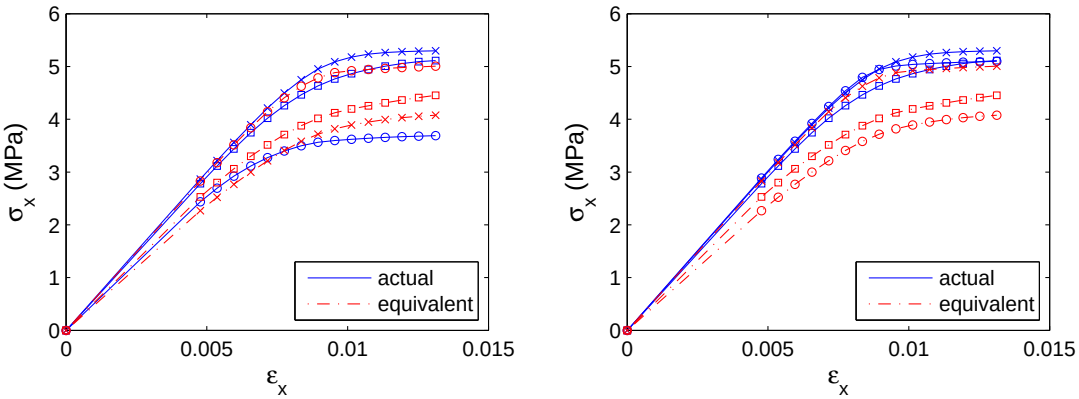

(a) Same position in the parent billet (b) Same void volume fraction

Figure 4.8. Comparison of actual and equivalent void models under uniaxial compressive loading in T direction

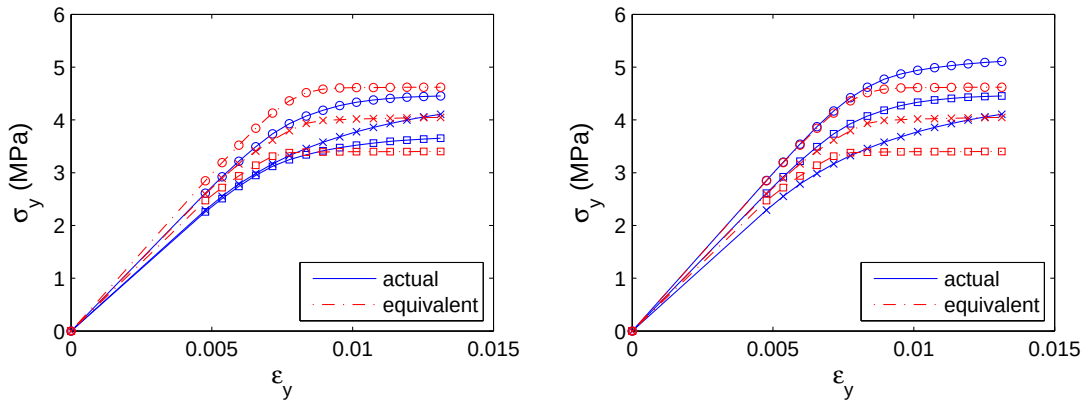

(a) Same position in the parent billet

(b) Same void volume fraction

Figure 4.9. Comparison of actual and equivalent void models under uniaxial compressive loading in TT direction

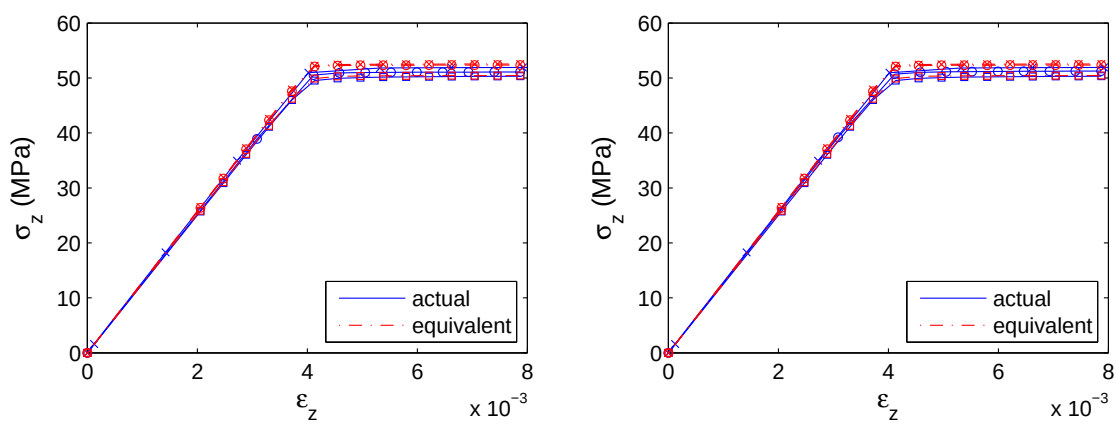

(a) Same position in the parent billet

(b) Same void volume fraction

Figure 4.10. Comparison of actual and equivalent void models under uniaxial compressive loading in L direction

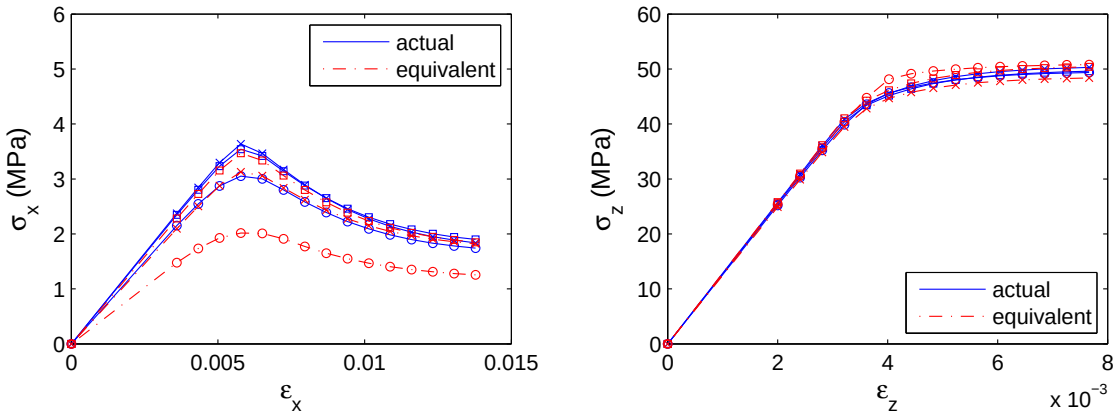

(a) Normal stress along T direction

(b) Normal stress along L direction

Figure 4.11. Comparison of actual and equivalent void models under biaxial compressive loading in T+L directions

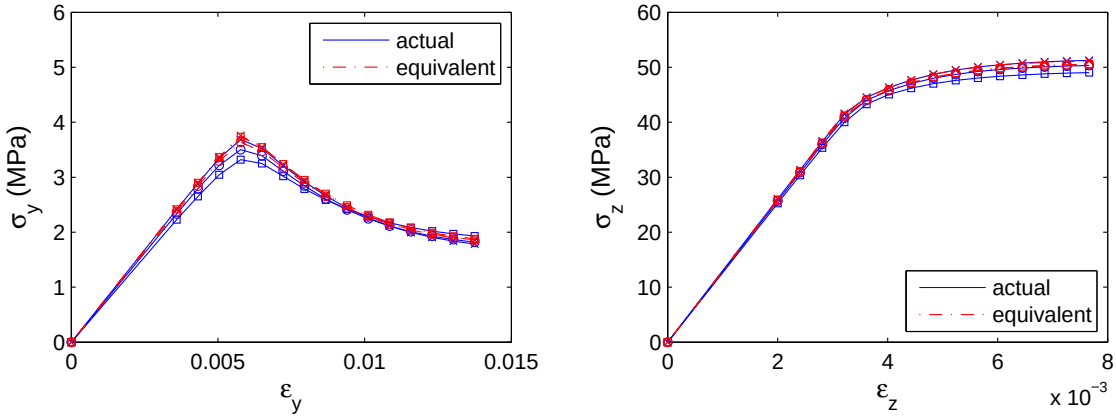

(a) Normal stress along TT direction

(b) Normal stress along L direction

Figure 4.12. Comparison of actual and equivalent void models under biaxial compressive loading in TT+L directions

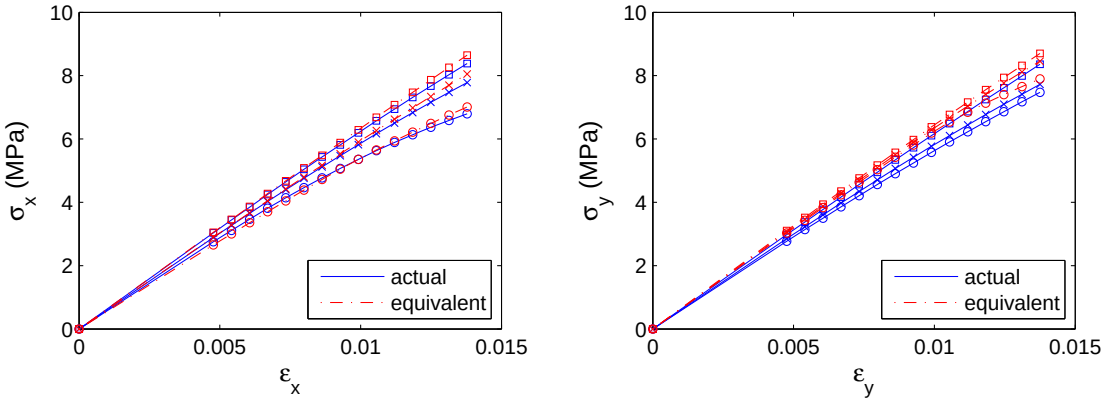

(a) Normal stress along T direction

(b) Normal stress along TT direction

Figure 4.13. Comparison of actual and equivalent void models under biaxial compressive loading in T+TT directions

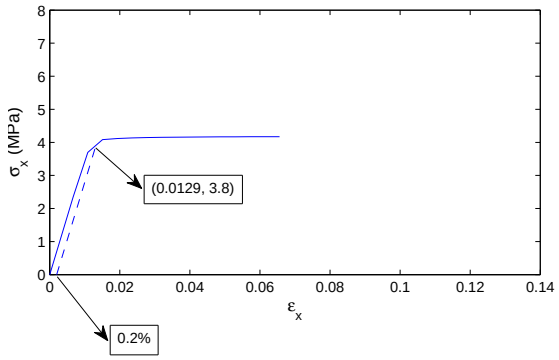

(a) Loading along T direction

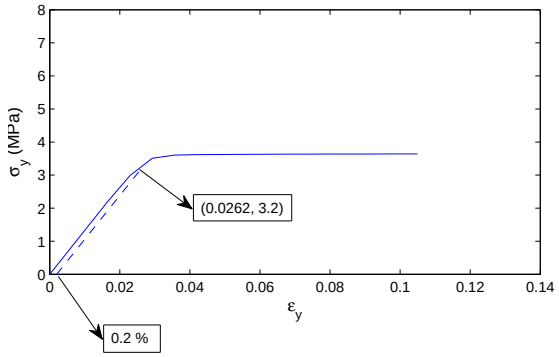

(b) Loading along TT direction

Figure 4.14. Stress-strain relationship of the models calibrated to match the experimental data; Dashed lines have been drawn to locate the yield point using 0.2% offset method

CHAPTER 5

STUDY OF THE EFFECT OF VOID SHAPE ON PSL NONLINEAR TENSILE BEHAVIOR

5.1 Problem Statement

Compressive simulations showed that if actual voids are replaced with their equivalent ellipsoids, the behavior of model will be acceptably similar. But since the behavior of wood under tension is very different from its behavior under compression (the former is brittle, while the latter is ductile), it is necessary to investigate if the ellipsoidal shape also works well in tensile simulations or not.

The tests conducted by Krupka on PSL [38, 21] can help us very much in this study. Krupka has done displacement control uniaxial tensile tests for all three material directions and also studied the size effect problem. The results of these tests will be used both for comparison with simulation results (as well as calibration of model) and size effect study.

Before starting the comparative study of void shapes, an appropriate model must be chosen to simulate the tensile behavior of wood stands. The software has an element removal option based on the allowable effective plastic strain (EPA) within each element. The point is how to determine the allowable effective plastic strain in each material direction. For this reason, unlike the compressive study in last chapter, it was decided to perform the calibration of numerical model before the comparative study of void shapes. In the calibration stage, it has been assumed that the elastic moduli of wood strands are the same in compression and tension, and the proper values for strengths and EPA of strands in different material directions have been determined.

To compare the void shapes, for each void model (actual or equivalent) under each uniaxial loading scenario (3 uniaxial loadings in each material direction), 3 finite element models have been made and analyzed (3 pairs of corresponding actual and equivalent models have been taken from the same location in the parent billet). Totally 18 simulations have been done in this stage of study.

Let us explain the terminology which will be used in this chapter. Based on the hypothesis that PSL's constitutive behavior is similar to that of solid-sawn lumber, a scheme of the expected constitutive behavior of PSL material under tension is illustrated in Fig.5.1. σ_t and ϵ_t represent tensile stress and tensile strain respectively. The material's macro scale behavior is in linear phase until its sudden rupture (however, there may be local nonlinearities in meso scale). The maximum tensile stress which the material bears is called "tensile strength" or "tensile ultimate stress" and labeled by σ_u. The strain corresponding to the tensile ultimate stress is called "tensile ultimate strain" (ϵ_u) that is also the maximum strain which the material can experience.

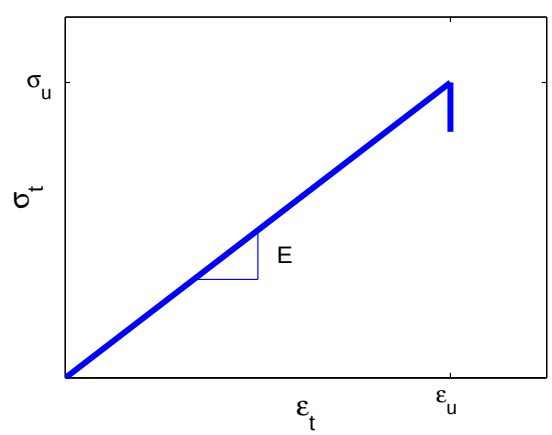

Figure 5.1. A Scheme of the expected stress-strain relationship of PSL material under tension

5.2 Material Properties and Finite Element Modeling

The elastic moduli are assumed to be equal to the values found in compressive simulations by calibration: E_T = 375 MPa, E_{TT} = 150 MPa, E_L=13000 MPa. However, the strengths of material under tension is different from the strengths under compression. These are the tensile strength looked up from Wood Handbook [4] and used in linear analysis (Table 3.7): $S_T = 1.5MPa$, $S_{TT} = 1.5MPa$, $S_L = 53.7MPa$. Poisson's ratios are assumed identical to the values selected for linear analysis: ν_{LT}=0.15, ν_{LTT}=0.15 and ν_{TTT}=0.09.

In reality, wood strands are brittle under tension, but in this study, they are considered elastic-perfectly plastic. Nevertheless, an important modification in strands' constitutive model causes brittle behavior appear in macro scale in PSL models. Brittle behavior is modeled using ADINA's "element death upon rupture" option. Element death (removal) is automatically activated when rupture is detected at any integration point of the element. Here, rupture is defined as when the plastic strain of element becomes larger than the maximum allowable effective plastic strain (EPA). EPA is a positive value inputed by the user [1]. Note that EPA is the allowable effective plastic strain, not the total strain. In an incremental procedure shown in Fig.5.2 ,total strain increment ($d\epsilon$) equals the sum of elastic strain increment ($d\epsilon^e$) and plastic strain increment ($d\epsilon^p$). Effective plastic strain increment ($d\epsilon^{ep}$)equals the absolute value of plastic strain increment [16].

$$d\epsilon = d\epsilon^e + d\epsilon^p \tag{5.1}$$

$$d\epsilon^{ep} = \sqrt{d\epsilon^p d\epsilon^p} \tag{5.2}$$

When an element ruptures, the mass and stiffness contribution of the element will be removed from the model [2]. The loads will be redistributed based on the new

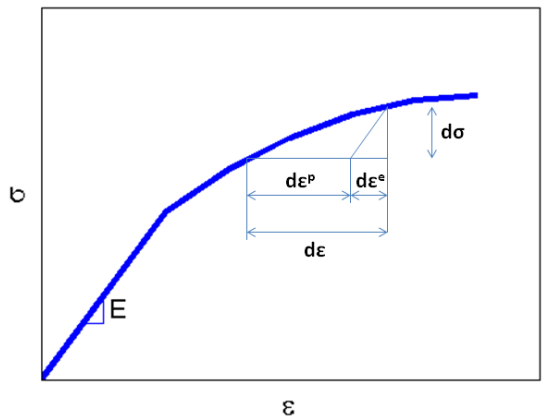

Figure 5.2. Stress-strain relationship after a plastic deformation

stiffness matrix and the stresses within each element will be calculated again. If any other element under the new state of stress ruptures, it will be removed from the model, the mass and stiffness matrix will again be updated and the loads will be redistributed. This procedures is repeated again and again until no element ruptures anymore and the whole model reaches the state of equilibrium.

As the simulations progressed, we were convinced that just one loading scenario was enough to decide about the accuracy of equivalent models compared to actual ones (the reason will be explained later in section 5.3). Loading is tensile, uniaxial and displacement control along the longest direction of each model. The sizes of models are identical to the sizes selected by Krupka in the experiment: 51×38×15 mm for loading in T and TT directions and 102×24×15 mm for loading in L direction. Based on the elastic moduli and strength of material in each material direction, the total displacement selected to be applied in T direction is 0.25 mm (0.5% total strain), but the applied total displacements in TT and L direction are both 0.5 mm (1% and 0.5% total strain respectively). Remember that tensile ultimate strains (that equals tensile strength over elastic modulus) defined for wood strands were 0.4%, 1% and 0.4% for T,TT and L directions respectively. That is why it is believed that the strain values defined to be applied on the model will ensure rupture.

The size of each finite element is the same as the digital voxels, 0.25×0.25×4.02 mm in T,TT and L directions respectively. As mentioned before, the investigation done on finite elements aspect ratio in the section 3.3 showed that this element size is acceptable for the loadings in T and TT directions. The aspect ratio should not make any problem when the model is loaded in L direction, because the longest dimension of each finite element is aligned L direction. No finite element has been allocated to the void phase.

Just like linear and nonlinear compressive uniaxial analyses, the boundary conditions are only applied to the nodes at the base of each model. In all models, one of the base nodes is constrained along the three displacement directions and the other base nodes are just constrained along the direction of loading (Fig.3.1 with this difference that the applied displacement is now tensile)

For each of the three loading cases, three models of actual voids and three models of equivalent ellipsoids have been analyzed (each pair of actual and equivalent models selected from similar positions in the big 110×120×610 mm billet). The tensile simulations showed that conducting more simulations on a set of actual and equivalent models with similar void volume fractions was not required.

5.3 Results of Analyses

5.3.1 Calibration of model

The report of experiment just includes the strength of PSL specimens under tension and does not provide any data about tensile stiffness of PSL. In this case, it is easier to assume that the moduli of elasticity in all three directions are equal in compression and tension. Wood Handbook [4] supports this assumption. Two other parameters, tensile strength of wood material and EPA, should be calibrated. Obviously, along each material direction, these two values differ from the corresponding values along the other two directions.

As the first step, to find the appropriate values of wood material strengths in three material directions, it is assumed that the material is elastic-perfectly plastic (along all directions) under tension without the "element death upon rupture" option activated (EPA is set to be zero). Yield stress values are the same as the ones mentioned in the previous section (let us emphasize that for elastic-perfectly plastic material, yield stress and strength are equal). For each loading case, one actual model with void volume fraction equal to the average fraction (2.5%) have been made and analyzed. Figure 5.3 depicts the models' stress-strain relationship under the assumption of material elastic-perfectly plastic behavior. The average strength values of PSL specimens (with the same size as models) which have been measured in experiment are 0.9 MPa, 0.6 MPa and 52.1 MPa for T, TT and L directions respectively. Comparing tested values with the ultimate stresses (strengths) obtained from simulation, it is concluded that even when no rupture occurs (i.e. no element deletion in the simulations), the strength of PSL model in L direction is less than the experimentally measured value. Therefore, in numerical models, a larger material strength in L direction must be defined. The new value for S_L is selected to be 80 MPa.

When the option "element death upon rupture" is turned on by selecting a non-zero value for EPA, the models show a very different behavior from what is seen in Fig. 5.3. In the first attempt, EPA is considered 10^{-6}. When element removal is activated, ADINA does not let EPA be zero (in other words, when EPA is zero, element removal is automatically deactivated). Hence, to model material rupture right at the yield time, EPA should be very small value and nearly zero, but not zero. That is the reason for the selection of EPA=10^{-6}. Three models for each loading scenario have been made and analyzed. The void volume fractions are different, that is the main reason that models show different strengths under similar loading. The results (as shown in Fig. 5.4) are not good at all. Except ○ case under uniaxial

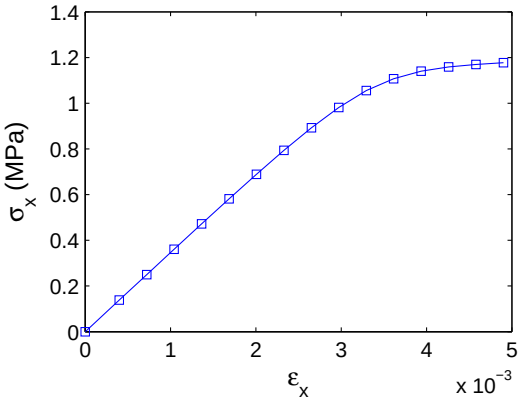

(a) Loading along T direction

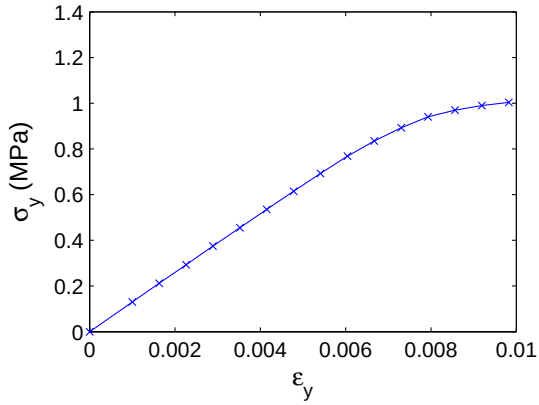

(b) Loading along TT direction

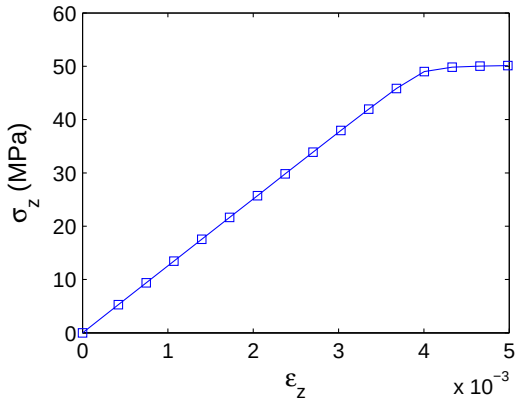

(c) Loading along L direction

Figure 5.3. Stress-strain relationship of PSL models under tension when the material is considered plastic

loading in TT direction (which has low void volume fraction of 0.8%), all models become unstable very soon and therefore their strength is much less than what expected. EPA must definitely be increased. The following values are selected for EPA in different directions: $(EPA)_T$=0.5×$\epsilon_{yield,T}$=0.002, $(EPA)_{TT}$=0.5×$\epsilon_{yield,TT}$=0.005, $(EPA)_L$=2×$\epsilon_{yield,L}$=0.012. Where ϵ_{yield} in each direction equals the wood strands' yield stress (=strength) in that direction divided by its corresponding elastic modulus. The stress-strain relationships of the actual models shown in Fig.5.5 are the results of application of these EPA values. The average strength of models are respectively 1.0 MPa, 0.8 MPa and 49.1 MPa in T, TT and L directions which are 10%,

33% and 6% different from average experimental measurements. Although there is a considerable difference between numerical and experimental average strengths in TT direction, since the absolute value of this strength is rather small, it is not unreasonable to accept the material properties applied in the last set of numerical models as the calibrated properties. Table 5.1 lists the calibrated values of all material tensile properties required for modeling PSL under tension.

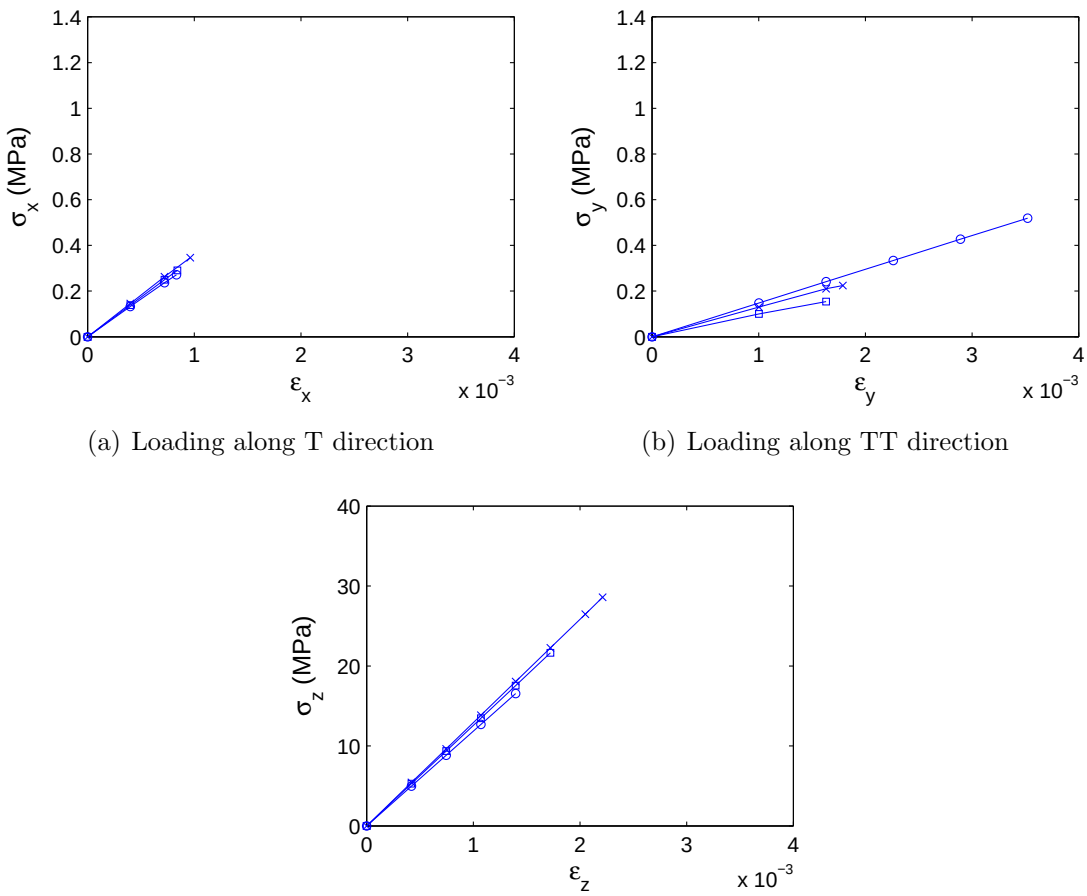

(a) Loading along T direction

(b) Loading along TT direction

(c) Loading along L direction

Figure 5.4. Stress-strain relationship of actual PSL models under tension when the allowable plastic strain is nearly zero

Table 5.1. Calibrated values for wood strands' tensile properties in an elastic-perfectly plastic constitutive model

Property	Value
S_T	1.5 MPa
S_{TT}	1.5 MPa
S_L	80 MPa
S_{TTT}	9.2 MPa
S_{TL}	5.9 MPa
S_{TTL}	9.2 MPa
E_T	375 MPa
E_{TT}	150 MPa
E_L	13000 MPa
ν_{TTT}	0.09
ν_{TL}	0.15
ν_{TTL}	0.15
$(EPA)_T$	0.002
$(EPA)_{TT}$	0.005
$(EPA)_L$	0.012

5.3.2 Comparison of actual and equivalent models

Actual and equivalent models, the behaviors of which are shown in Fig. 5.5, are taken from exactly identical positions in the parent billet. The positions of the lower left corner of the models used for the loading in T direction are $\times$:(X_T=2.5 mm, Y_{TT}=2.5 mm, Z_L=25 mm), $\bigcirc$:(X_T=13 mm, Y_{TT}=65 mm, Z_L=279 mm) and $\square$:(X_T=25 mm, Y_{TT}=51 mm, Z_L=533 mm) in the parent PSL billet. The void volume fractions in actual models are respectively 1.1%, 2.9% and 2.4%; while in equivalent models, they are 1%, 1.5% and 1.7%. In the models used for loading in TT direction, the position of the lower left corners are respectively $\times$:(X_T=5 mm, Y_{TT}=5 mm, Z_L=25 mm), $\bigcirc$:(X_T=51 mm, Y_{TT}=13 mm, Z_L=254 mm) and $\square$:(X_T=76 mm, Y_{TT}=25 mm, Z_L=521 mm). The void volume fractions in actual models are 2.9%, 0.8% and 5.8%; and in equivalent models are 4.2%, 0.4% and 1.5% respectively. And in the models used for loading in L direction, the position of the lower left corners are respectively $\times$:(X_T=2.5, Y_{TT}=2.5, Z_L=25 mm), $\bigcirc$:(X_T=25 mm, Y_{TT}=25 mm,

Z_L=254 mm) and □:(X_T=64 mm, Y_{TT}=64 mm, Z_L=457 mm). The void volume fractions are 0.6%, 6.4% and 2.6% in actual and 0.7%, 5.6% and 3.2% in equivalent models respectively.

Like previous set of simulations with smaller value of EPA, most of the simulations with larger EPA also stopped due to instability before full defined displacement was applied. In almost all cases, at the macro scale, models are still in linear phase when they become unstable (It should be emphasized that this is not true for meso scale, since for element deletion to occur, plastic strain must occur). Under loading in TT direction, the strength (ultimate stress) of corresponding actual and equivalent models are almost equal. The average strength in actual models is 0.8 MPa and in equivalent models is also 0.8 MPa. Standard deviations are 0.6 MPa and 0.5 MPa respectively. Of course, because the number of simulations for a certain void model and loading scenario is just three, mean and specially standard deviation absolute values are not that reliable. But just for the sake of comparison relative to the statistical values other void model, they are acceptable. There is now enough evidence to show that ellipsoidal representation of voids acts properly under tensile loading in TT direction.

But this conclusion is not true for loadings along T and L directions. Figures 5.5(a) and 5.5(c) apparently show that the performance of equivalent models is very poor and in all cases the strength of actual models is more than that of equivalent models. The mean strengths in actual models are 1 MPa and 49.1 MPa as loading is along T and L directions respectively. The corresponding values for equivalent models are 0.7 MPa and 28.1 MPa, i.e. 30% and 43% lower. Even in the cases that the void volume fraction of an equivalent model is less than that of its corresponding actual model, again the strength of equivalent model is lower. Therefore, the simulations show that ellipsoidal representation of actual void shapes are not able to model the tensile behavior of material under loadings in T and L directions. The most important

loading direction is for sure L direction; so, it is reasonable to conclude that ellipsoids should not be used for modeling PSL material under tension.

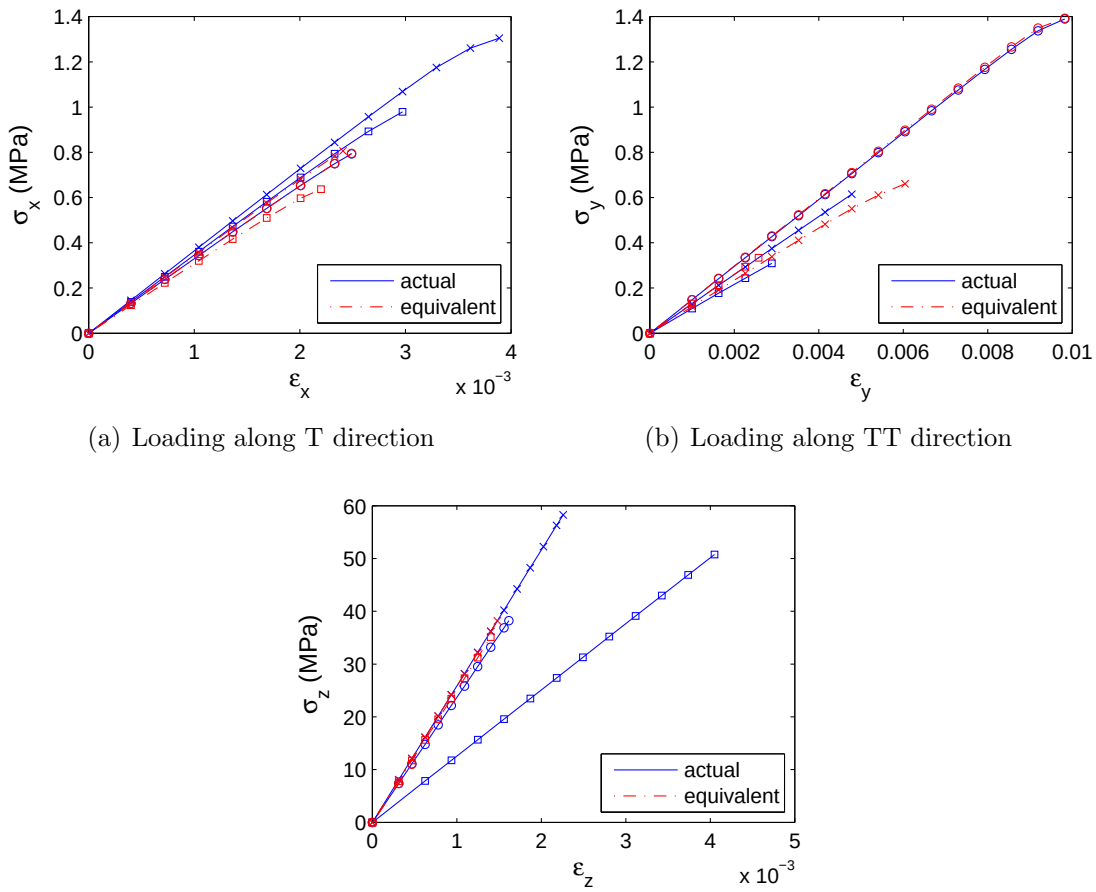

(a) Loading along T direction

(b) Loading along TT direction

(c) Loading along L direction

Figure 5.5. Comparison of the tensile behavior of corresponding actual and equivalent models which are taken from identical positions in the parent billet

One possible explanation for the discrepancy between T and L directions on one side and TT direction on the other side is that in most cases the smallest radii of ellipsoids are along TT direction. Therefore, the likelihood that TT stresses in the finite elements in vicinity of voids reach their yield stress is lower than the same likelihood for the finite elements in the models loaded in T or L directions. That is why equivalent models loaded in TT direction can maintain their stability more than the equivalent models loaded in T or L directions. In other words, the reason that

equivalent models are compatible with actual models under TT loading is that the dimension of the voids (actual and ellipsoidal) in TT direction is so small that the void shapes can not influence the stresses in the vicinity of voids. The bigger the voids' dimension along the direction of loading, the more void shapes' effect on the magnitude of stresses.

CHAPTER 6

PROBABILISTIC MODELING OF PSL MATERIAL UNDER COMPRESSIVE LOADING

25×25×76 mm models with calibrated material properties (Tab. 6.1) were loaded uniaxially under compression (displacement control along the longest direction of each model) and their behavior was compared to the experimental data. 15 simulations were conducted for each loading direction. As usual, there were three loading scenarios (uniaxial along each material direction) and the applied displacement in each scenario was selected based on the elastic modulus and strength of material in that direction. The total displacement selected to be applied in T direction was 5 mm (6.6% total strain), while the applied total displacements in TT and L direction were respectively 8 mm and 0.6 mm (10.5% and 0.8% total strain respectively). The size of each finite element was 0.25×0.25×4.02 mm in T,T and L directions respectively.

A set of virtual ellipsoids was generated to be used as void model in these simulations. The distributions of volumes, moments of inertia, orientations and locations of virtual ellipsoids are the same as that of actual voids. The aim of this investigation is to show that it is possible to make a PSL model including a random set of ellipsoidal voids and calibrate it in a way that the mechanical statistics of model match the experimental statistics.

Figure 6.1 shows the stress-strain curves obtained from Monte Carlo simulations. Statistics of the results of simulations have been compared with that of experimental data in Table 6.2. As mentioned in section 4.1, there is experimental data available for longitudinal compressive yield stress and strain of PSL which is presented by Winans

Table 6.1. Suggested material properties for the calibration of numerical compressive models

Class	Property	Value
Stiffness	E_T	375 MPa
	E_{TT}	150 MPa
	E_L	13000 MPa
	ν_{LT}	0.15
	ν_{LTT}	0.15
	ν_{TTT}	0.09
Yield Stress	S_T	5.0 MPa
	S_{TT}	5.0 MPa
	S_L	53.5 MPa

et al.[7]; but there had been no data available for transverse and thru thickness mechanical yield stress of PSL before the tests conducted during this project (section 4.2). Statistics of all the mentioned experimental studies are presented in Table 6.2.

Table 6.2. Statistical comparison of yield stress (in MPa) of calibrated virtual ellipsoidal void models loaded under compression in different material directions with the corresponding experimentally measured values

	Mean Yield Stress (MPa)		St. Dev. of Yield Stress (MPa)		COV (%)	
Loading Direction	Exp.	Num.	Exp.	Num.	Exp.	Num.
T	3.32	3.72	0.22	1.20	6.7	44.7
TT	2.92	2.51	1.37	0.58	47.0	24.2
L	52.0	50.4	8.0	1.0	15.4	2.1

It is not surprising if the standard deviations of experimentally measured yield stresses are larger than that of stresses calculated in simulations. Arbitrary shapes of actual voids have certainly more deviation than the smooth and adjusted ellipsoidal shapes. Therefore, that the coefficients of variation of experimental yield stresses measured under loadings in TT and L directions are respectively almost 2 and 7 times of their corresponding numerical yield stresses is expectable and justified. But the author does not currently have any explanation that why under the loading in T direction the coefficient of variation of simulated yield stresses is much larger than that of measured yield stresses.

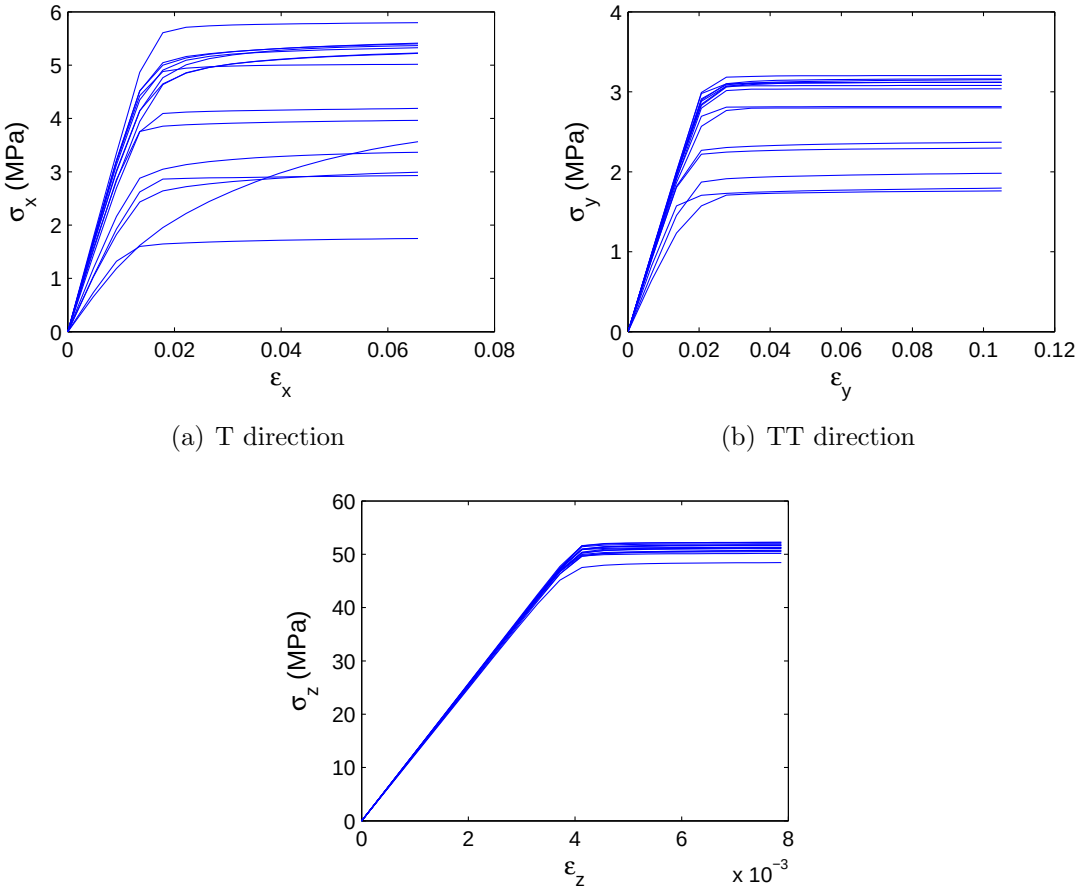

(a) T direction

(b) TT direction

(c) L Direction

Figure 6.1. Stress-strain relationship of calibrated virtual ellipsoidal void models under uniaxial compression

Although standard deviations of stresses of experimental and numerical models do not match, the mean values are within 10% difference and therefore acceptable. It is very difficult to simulate voids with a smoother shape and also calibrate material properties in such a way that both mean and standard deviation of the resulting yield stresses match. Hence, it is reasonable to prefer matching mean values rather than standard deviations.

It should be emphasized that the material behavior in numerical models was elastic-perfectly plastic and therefore the post-yielding behavior of models does not

match that of experiments. The proposed material compressive properties in this study are good in design (pre-yielding) range.

To sum up, it was shown in this chapter that finite element models of PSL, that include virtually generated ellipsoidal voids (that have identical geometrical statistics with the ellipsoids fit to the actual voids) and assume PSL's wood phase as a continuum medium with certain calibrated material properties, can simulate the average pre-yielding stress state of PSL specimens under uniaxial compressive loading along all three material directions. Especially, these numerical models are sufficiently accurate for the case of compressive loading of PSL material along the most structurally important direction, namely L direction. It is recommended not to be satisfied with the simulation of one or few virtual models and conduct a Monte Carlo simulation to obtain a decent strength range for a given specimen size and loading scenario.

CHAPTER 7

PROBABILISTIC MODELING OF PSL MATERIAL UNDER TENSILE LOADING

7.1 Problem Statement

The effect of void shape on brittle behavior of PSL material was studied in section 5.3. It was concluded that ellipsoids are not an appropriate replacement for actual voids when the model is under tension. A new model must be found to represent void structure when an arbitrary model of PSL is made for analysis. Since the material behavior is very sensitive to the shape of voids, it is reasonable to find a way to use the actual shapes. Grigoriu et al.[29] has worked on basically similar problem for modeling concrete aggregates and concluded that a Gaussian non-stationary random field defined by the sum of spherical harmonic functions with Gaussian coefficients is superior to the spherical harmonic functions of aggregate shape with random non-Gaussian coefficients. The interesting point in this paper for our purposes is that they had a library of 128 actual aggregate shapes obtained from the same material and used it to calibrate their models. This method is applicable for PSL voids. Since we have a very good database of PSL voids (containing more than 17000 voids), it is easy to make a void library that includes voids' lengths, volumes and mass moments of inertia. The important point is how one should pick voids randomly and put them in a model. Two methods of void random selection will be proposed in the following section.

7.2 Material Properties and Finite Element Modeling

The elastic moduli are again assumed to be equal to the values found in compressive simulations by calibration: E_T = 375 MPa, E_{TT} = 150 MPa, E_L=13000 MPa. Poisson's ratios are: ν_{LT}=0.15, ν_{LTT}=0.15 and ν_{TTT}=0.09. The tensile strengths in T and TT directions have been picked from Wood Handbook[4]: $S_T = 1.5MPa$, $S_{TT} = 1.5MPa$; but for the reason explained in the calibration study in section 5.3, it was decided to choose a value larger than what was suggested in the Wood Handbook for the tensile strength in L direction. Now: $S_L = 80MPa$.

Brittle behavior is modeled using ADINA's "element death upon rupture" option. Rupture is defined as when the plastic strain of element becomes larger than the maximum allowable effective plastic strain (EPA). As explained in section 5.3, the following values are selected for EPA in different directions: $(EPA)_T$=0.5×$\epsilon_{yield,T}$=0.002, $(EPA)_{TT}$=0.5×$\epsilon_{yield,TT}$=0.005, $(EPA)_L$=2×$\epsilon_{yield,L}$=0.012. Where ϵ_{yield} in each direction equals the material strength in that direction divided by its corresponding elastic modulus. All these properties have already been listed in Table 5.1.

Loading is tensile, uniaxial and displacement control along the longest direction of each model. The sizes of models are identical to the sizes selected by Krupka in the experiment[38, 21]: 51×38×15 mm for loading in T and TT directions and 102×24×15 mm for loading in L direction. Based on the elastic moduli and strength of material in each material direction, the total displacement selected to be applied in T direction is 0.25 mm (0.5% total strain), but the applied total displacements in TT and L direction are both 0.5 mm (1% and 0.5% total strain respectively). These strain values are almost equal to the ultimate strains of wood strands in different directions (i.e. strands' strengths in different directions divided by their corresponding elastic moduli), so, it is expected that these strains cause fracture in the model.

The size of each 3D solid finite elements is the same as the digital voxels, 0.25×0.25×4.02 mm in T,TT and L directions respectively. It was shown in section 3.3 that the aspect

ratio of these elements does not spoil the overall accuracy of model, but some large local stresses may be estimated less than their real values. In this stage of study, some models with more than 210000 elements have been analyzed, and it is not practical to increase the number of elements by decreasing the elements' aspect ratio.

The boundary conditions are only applied to the nodes at the base of each model. In all models, one of the base nodes is constrained along the three displacement directions and the other base nodes are just constrained along the direction of loading (Fig. 3.1).

A side conclusion from the comparison of actual and ellipsoidal void models was that the number of simulations for each void model should be increased. In other words, more comprehensive Monte Carlo simulations are really required. To compare actual and random void models, for each of the three loading cases, 15 models of actual voids and 15 models of random voids have been analyzed (totally 90 models). Then, new Monte Carlo simulations were conducted on the models with different sizes to study the size effect. The details of size effect study will be expressed in section 7.5.

Random models are made by picking the voids randomly from the void library and putting them in random locations in the model. The question is how the void volume fraction should be selected for each random void model. In other words, how many voids with what volume should be put in each model? To find the distribution of void volume fractions in actual models, 48 longitudinal actual models (with the size 24×15×102 mm) have been selected from random positions in the parent billet. Figure 7.1 displays the histogram of the void volume fractions of the selected models. Among the known distributions, Beta distribution, the PDF of which is given by Equation 7.1, fits the best to the data.

$$f(x; a, b) = \frac{\Gamma(a+b)}{\Gamma(a)\Gamma(b)} x^{a-1}(1-x)^{b-1} \tag{7.1}$$

where $\Gamma(z)$ is the Gamma function given by:

$$\Gamma(z) = \int_0^\infty e^{-t} t^{z-1} \, \mathrm{d}t \tag{7.2}$$

The same investigation for transverse and thru thickness models concluded that Beta distribution fits the void volume fractions properly. Therefore, in the Monte Carlo simulations, the target void volume fractions will be selected randomly from Beta distribution. The calculated parameters of Beta distributions that best fit each type of models are shown in Table 7.1. With these a and b values, the Beta PDF will be defined in the interval of [0, 0.08] that represents the range of 0 to 8% for void volume fraction.

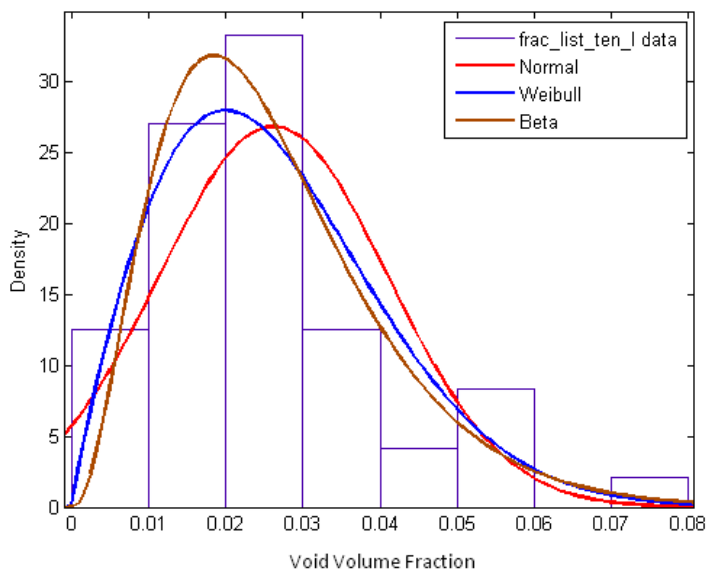

Figure 7.1. Histogram of the values of void volume fraction of longitudinal models along with the best three known distribution fitted to the data

Table 7.1. Parameters of Beta distribution that fit the best to the void volume fractions of different model types

Type of Model	Size (mm)	Beta Parameters	
		a	b
T	51×15×38	4.89	174.74
TT	15×51×38	3.26	121.28
L	24×15×102	3.26	121.28

7.3 Methods of random selection of voids

There are two ways to approach the question of random selection of voids from the void library. First method is to categorize the voids based on their size, find the contribution of each size category to the set of all voids in the parent billet, set a target void volume fraction for a computer model and fill the model with the voids taken from each category based on the share of that certain category until the target void volume fraction is reached. This method is qualitatively similar to the design of concrete mixture using aggregate with different size. If the methods are similar, their names can be similar too. This method is called random selection of voids based on "voids' mix design". A short statistical survey shows that the voids with volume between 0 and 100 mm^3 make 21% of the whole void volume in the parent billet. These voids are called fine voids. The category of medium voids consists of the voids with volume between 100 mm^3 and 1000 mm^3 that represent 36% of the whole void volume. The remaining 43% of whole void volume include coarse voids with volume between 1000 mm^3 and 11000 mm^3. For example, if a model with 2.5% void volume fraction is to be made, 0.525% (=0.21×2.5%) of void volume fraction consist of fine voids, 0.9% (=0.36×2.5%) consist of medium voids and 1.075% (=0.43×2.5%) consist of coarse voids.

The second method has stemmed from the fact that when an actual model is taken from a random location of the big parent billet, the model's voids are not categorized. In other words, there may be no or few voids of a certain size in an actual model.

Therefore, void categorization and mix design may not be an appropriate way of void selection. It makes sense to pick the voids fully randomly and without any mix design from the library and fill the model with voids until the target void volume fraction is reached. Our library has exactly 17065 voids, but coarse voids are just 1% of them (in number); hence, this method of random selection will most probably result in models with no or few coarse voids.

To investigate the effect of mix design of voids on tensile strength of PSL models, 9 actual models, 3 models for each loading direction, and 9 mix designed random models, again 3 models for each loading direction, with corresponding void volume fractions have been made. The number of voids in all 18 models were counted. Each $\times$ marker in Fig.7.2 represents a pair of corresponding actual and random models (i.e. an actual and a random model with identical void volume fractions). Figure 7.2 shows clearly that (#1) in most cases, mix designed models have fewer or equal number of voids than actual models (i.e. the ratio of number of voids in 7 out of 9 cases is less than or almost equal to 1). Since the void volume fractions of corresponding models are equal, in the mentioned cases, the mix designed models have larger voids than the actual models have. (#2) The regression line in Fig. 7.2 implies that as the ratio of number of voids in a random model to that of its corresponding actual model increases, the ratio of their tensile strengths also increases. Therefore, for a certain void volume fraction, the fewer the number of voids (i.e. the larger the voids), most probably the less the tensile strength of model. The conclusion from (#1) and (#2) is that void mix design method will most probably result in the underestimation of tensile strength.

It is worth to discuss about the equation of regression line here. Based on this equation, when the ratio of number of voids is 1 (in other words, when a pair of actual and random model have exactly the same void volume fraction and number of voids), the ratio of their strengths is more than 1. At the first glance, this conclusion

may seem wrong, but it is not. Let us not forget that voids have four sources of uncertainty: 1) volume fraction, 2) size, 3) shape, 4) location. That the volume fractions and numbers of voids in two corresponding models are equal rules out just first and second sources of uncertainty (Of course, it can be argued that even in the case of identity of void volume fractions and numbers, void sizes are not necessarily the same; but let us assume that they are); and the other two sources of uncertainty still remain. Thus, it is possible that even when the void volume fractions and numbers of voids in corresponding actual and random models match, their tensile strengths do not match.

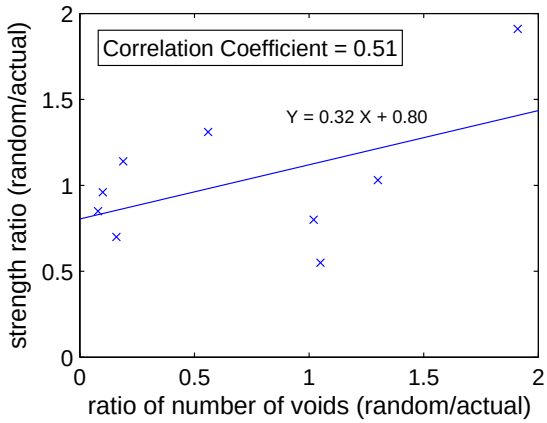

Figure 7.2. Mix design of voids may cause the decrease in the number and consequently the increase in the size of voids. Correlation of the ratio of number of mixed designed voids over the number of actual voids to the ratio of strength of corresponding models is displayed.

7.4 Comparison of actual and random void models

For each loading scenario, 45 simulations (15 simulations on actual void model, 15 simulations on mix designed random void models and 15 simulations on not mix designed random void models) have been performed. Failure happens when the rupture of finite elements causes overall instability. In this study, the ultimate stress at

the time of failure (i.e. the peak stress that the model can bear) is called the strength (Fig. 5.1). The strain at the time of failure is called the ultimate strain. Means and standard deviations of the strengths and ultimate strains of actual and random models were compared to find out if random models can be an appropriate replacement for actual models. If the values of mentioned parameters in random models are within 10% difference of that of actual models, they are considered acceptably close. As Figs. 7.3, 7.4 and Tables 7.2, 7.3 show, under the uniaxial loading in T and TT directions, mix designed random models present a better picture of material strength and ultimate strain that the models without mix design; because the statistics of their strength and ultimate strain is close enough to the statistics of actual models. On the other hand, mix design method does not act well as the loading is along longitudinal direction. Figure 7.5 and Tables 7.2, 7.3 confirm that it is better not to design the mixture of voids when the longitudinal tensile mechanical properties of PSL are of interest.

Table 7.2. Mean strength (in MPa) and ultimate strain (in %) of actual and random void models loaded in different material directions

Loading Direction	Strength (MPa)			Ultimate Strain (%)		
	Actual	Random		Actual	Random	
		mix design	no mix design		mix design	no mix design
T	0.82	0.86	1.13	0.25	0.26	0.34
TT	0.94	0.95	1.13	0.70	0.74	0.84
L	44.2	33.5	41.3	0.32	0.27	0.33

Table 7.3. Standard deviation of strength (in MPa) and ultimate strain (in %) of actual and random void models loaded in different material directions

Loading Direction	Strength (MPa)			Ultimate Strain (%)		
	Actual	Random		Actual	Random	
		mix design	no mix design		mix design	no mix design
T	0.18	0.14	0.16	0.05	0.04	0.05
TT	0.31	0.25	0.30	0.22	0.18	0.20
L	11.6	6.0	8.6	0.10	0.04	0.06

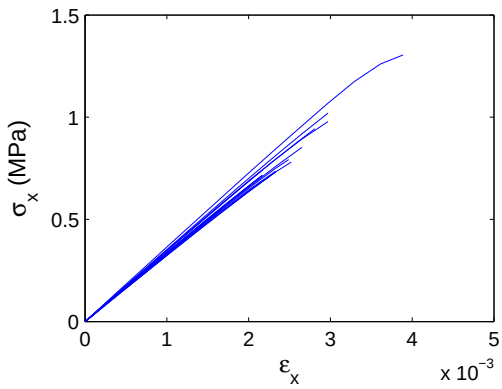

(a) Actual void models

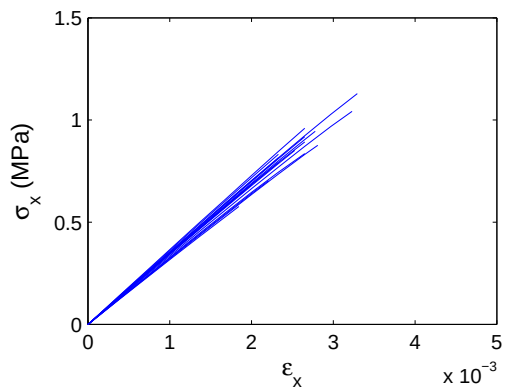

(b) Random void models with mix design

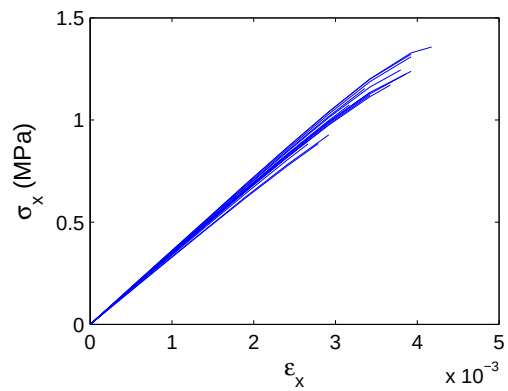

(c) Random void models without mix design

Figure 7.3. Comparison of actual and random void models under uniaxial tensile loading in T direction

It is hard to explain why mix design results in acceptable mechanical properties under the loading in T and TT directions but low mechanical properties under longitudinal loading. One possible explanation is that since the elements aspect ratio is almost 16 longitudinal units to 1 transverse or thru thickness unit, the stress concentration around large voids (which certainly exist in mix designed models, but may not exist in not mixed designed models) impacts the longitudinal properties more than transverse and thru thickness properties. Hence, mix design has affected longitudinally loaded models more than the other ones. Perhaps a smaller aspect ratio will have better ability to tolerate the effect of large voids.

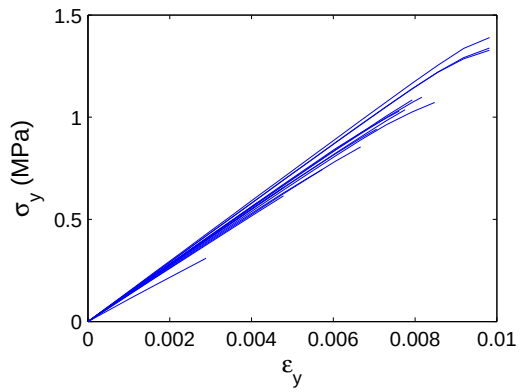

(a) Actual void models

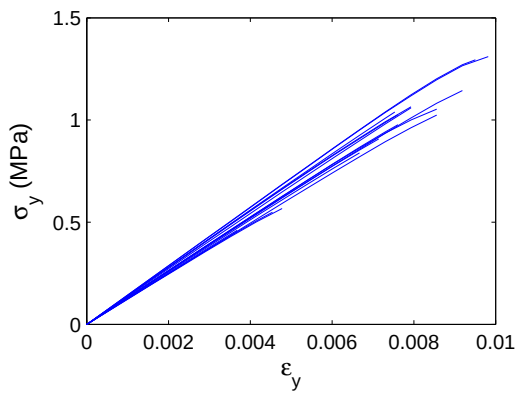

(b) Random void models with mix design

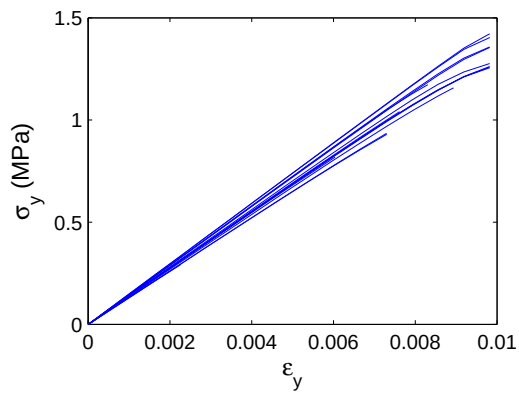

(c) Random void models without mix design

Figure 7.4. Comparison of actual and random void models under uniaxial tensile loading in TT direction

7.5 Study of the effect of size on tensile strength of PSL

Size effect is usually much more significant in brittle materials than in ductile materials. As the size of material gets larger, the number of critical defects increases. The increase of vulnerability will lead to the augmentation of the chance of abrupt failure in brittle materials; whereas in ductile materials, more critical defects just cause more local yieldings which may not contribute considerably to the overall failure of material.

Three model sizes for each loading scenario were selected. To ease the investigation, the cross sections perpendicular to the loading direction remained unchanged

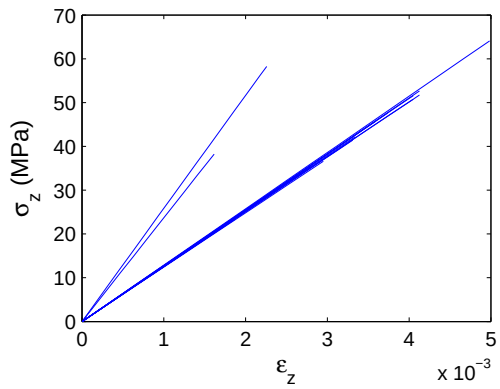

(a) Actual void models

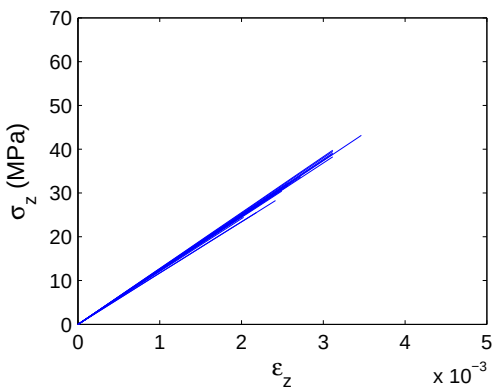

(b) Random void models with mix design

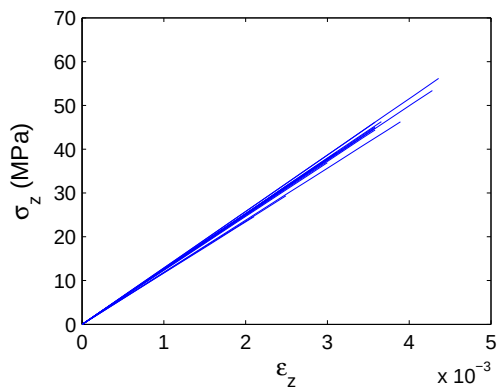

(c) Random void models without mix design

Figure 7.5. Comparison of actual and random void models under uniaxial tensile loading in L direction

and just the lengths parallel to the direction of loading changed. For uniaxial tensile loading along T direction, the dimensions of cross section of models are always TT=15mm and L=38mm; while these three transverse lengths were selected for the models: 38mm, 51mm, 76mm. The dimensions of cross section of thru thickness models are T=15mm and L=38mm and the selected lengths are 38mm, 51mm and 76mm. For longitudinal models, cross sections are T=24mm and TT=15mm and lengths are 51mm, 102mm and 152mm.

For each size, 15 actual and 15 random models were simulated. Based on the findings explained in the previous section, the transverse and thru thickness random models are mix designed, but the longitudinal random models are not.

Figures 7.6,7.7, 7.8, 7.9 and Tables 7.4, 7.5 show clearly that: 1) the mechanical statistics of random models match that of actual models; and more crucially 2) both actual and random models are able to simulate the size effect, i.e. as the length of model increases, its strength and ultimate strain decreases.

Table 7.4. Mean tensile strength (in MPa) and ultimate strain (in %) of three different sizes of actual and random void models loaded in different material directions

Loading Direction	Length (mm)	Strength (MPa)		Ultimate Strain (%)	
		Actual	Random	Actual	Random
T	38	0.91	0.90	0.28	0.28
T	51	0.82	0.86	0.25	0.26
T	76	0.73	0.71	0.22	0.22
TT	38	1.05	1.00	0.78	0.76
TT	51	0.94	0.95	0.70	0.74
TT	76	0.81	0.89	0.60	0.67
L	51	47.2	50.7	0.38	0.41
L	102	44.2	41.3	0.32	0.33
L	152	33.4	36.4	0.27	0.29

Table 7.5. Standard deviation of tensile strength (in MPa) and ultimate strain (in %) of three different sizes of actual and random void models loaded in different material directions

Loading Direction	Length (mm)	Strength (MPa)		Ultimate Strain (%)	
		Actual	Random	Actual	Random
T	38	0.30	0.15	0.08	0.04
T	51	0.18	0.14	0.05	0.04
T	76	0.17	0.17	0.04	0.05
TT	38	0.30	0.25	0.21	0.18
TT	51	0.31	0.25	0.22	0.18
TT	76	0.34	0.28	0.22	0.21
L	51	10.3	10.5	0.08	0.08
L	102	11.6	8.6	0.10	0.06
L	152	11.7	5.0	0.09	0.04

Since the mechanical properties of these models are not calibrated with the available experimental data, we can just compare the rate of change of strength in numerical and experimental data. In other words, while the absolute values of numerically calculated strengths are not comparable to the measured values, one can still find linear relation between specimen's (or model's) strength and length for similar loading conditions and compare the numerically and experimentally obtained slopes.

The linear relationship between length and tensile strength in the natural logarithmic space is defined by the following equation:

$$Ln(S) = A - MLn(L) \tag{7.3}$$

where S, L, A and -M are respectively tensile strength, specimen (or model) length, y-intercept (constant) and slope (M is positive, therefore slope is always negative which makes sense).

If two specimens (or models) with lengths L_1 and L_2 and measured (or calculated) tensile strengths S_1 and S_2 are taken into consideration, the absolute value of linear slope is:

$$M = -\frac{Ln(\frac{S_1}{S_2})}{Ln(\frac{L_1}{L_2})} \tag{7.4}$$

The values of M (absolute values of slopes) were calculated for numerical data and compared to the experimental values reported in the literature [38, 21]. For each loading scenario, the strengths of all actual and random numerical models were considered as a dataset, and the regression line of their strengths versus lengths in logarithmic space was drawn (Fig.7.10). The slopes of these regression lines (M) were calculated and reported in Table 7.6. Numerical random models successfully simulated the size effect in transverse and thru thickness models. But random longitudinal models showed different pattern of size effect comparing to the experimental data.

Perhaps ADINA's "element's death upon rupture" option cannot precisely simulate the brittle behavior of PSL material (especially when the material is loaded along L direction). On the other hand, whether the method of element removal can do its job successfully or not, we should not forget that there are other features in PSL material (e.g. the strand angles or the defects within the strand) that can drive the brittle failure. These features have not been considerd in our models; therefore, it is difficult to find a certain reason for the difference in the slopes of regression lines under longitudinal loading.

Table 7.6. Absolute value of the slope of the line that relates PSL tensile strength and length

Loading Direction	Absolute Value of Slope	
	Experimental	Numerical
T	0.36	0.32
TT	0.30	0.32
L	0.09	0.21

7.6 Calibration of PSL models for tensile simulation

Although a calibration study has been already done for tensile simulations in section 5.3, as the number of simulations of actual models rose, the results of analyses (presented in the previous two sections) showed that the tensile strengths of numerical models do not match that of experimental models yet. Therefore, the mechanical properties which were selected for the numerical tensile models should be calibrated again. As mentioned before, there is no experimental data available about the tensile stiffness of PSL; so, it is reasonable to keep the stiffness properties which were measured by compressive tests. But there is sufficient experimental information for calibrating the tensile strength properties [38, 21]. Table 7.7 suggests appropriate tensile properties obtained from the comparison of numerical and experimental data.

Table 7.7. Suggested material properties for the calibration of numerical tensile models

Class	Property	Value
Stiffness	E_T	375 MPa
	E_{TT}	150 MPa
	E_L	13000 MPa
	ν_{LT}	0.15
	ν_{LTT}	0.15
	ν_{TTT}	0.09
Strength	S_T	1.65 MPa
	S_{TT}	1.05 MPa
	S_L	100 MPa
	$(EPA)_T$	$0.5 \times \epsilon_{yield,T}$=0.0022
	$(EPA)_{TT}$	$0.5 \times \epsilon_{yield,TT}$=0.0035
	$(EPA)_L$	$4 \times \epsilon_{yield,L}$=0.0308

Figure 7.11 shows the results of Monte Carlo simulations on random void models with the input of calibrated material properties. Also, Table 7.8 compares the numerical calibrated mechanical statistics with the experimental statistics and confirms that the statistical data acceptably match and, this time, the calibration process has been successful.

Table 7.8. Statistical comparison of strength (in MPa) of calibrated random void models loaded under tension in different material directions with the corresponding experimentally measured values

Loading Direction	Length (mm)	Mean Strength (MPa)		St. Dev. of Strength (MPa)		COV (%)	
		Exp.	Num.	Exp.	Num.	Exp.	Num.
T	51	0.94	0.97	0.42	0.20	44.7	20.6
TT	51	0.62	0.64	0.15	0.21	24.2	32.8
L	102	52.1	57.6	9.3	10.6	17.9	18.4

To conclude, because of inability of ellipsoidal voids to simulate mechanical behavior of the mesostructure of PSL under tensile uniaxial loading, it was decided to make a library of actual voids detected experimentally and use the same voids in simulations. Numerical models were made choosing the voids randomly from the void library. The random selection of voids were done in two ways: 1) based on the

statistics of void volumes in the parent billet (mix design method) which was shown to be practical for transverse and thru thickness models; and 2) fully randomly without any constraint which worked better for longitudinal models. Under all loading scenarios, the mechanical behavior of this new void model was consistent with the actual void model. Regarding the size effect, and compared to the experimental data, the random void model performed properly as the loading was along T and TT directions, but it was not sufficiently good under L direction uniaxial loading. Finally, a calibration study was conducted and appropriate tensile properties were proposed for the numerical models of PSL.

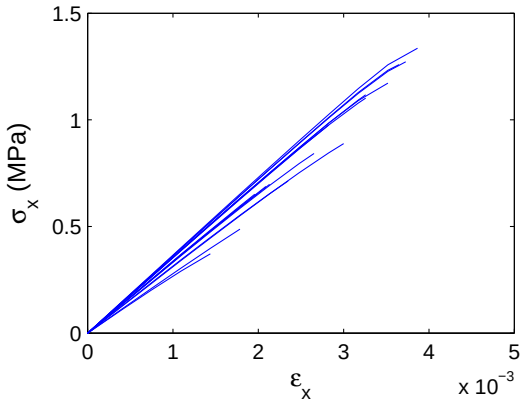

(a) Actual, Length=38mm

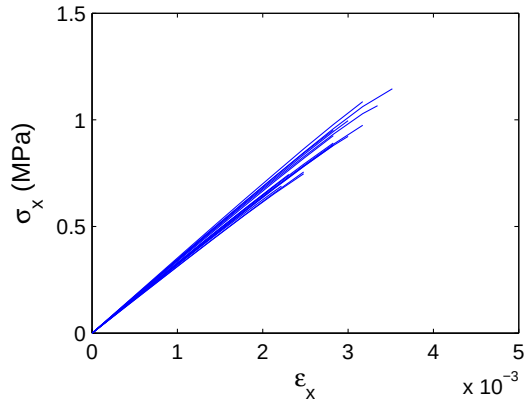

(b) Random, Length=38mm

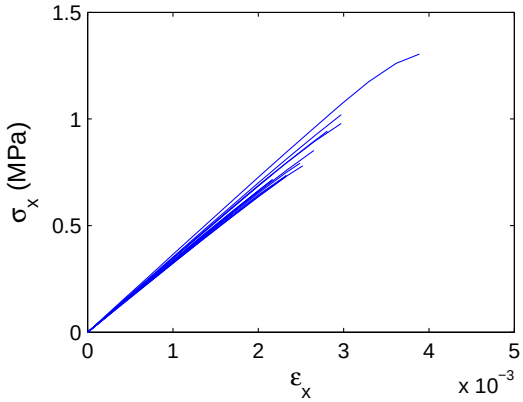

(c) Actual, Length=51mm

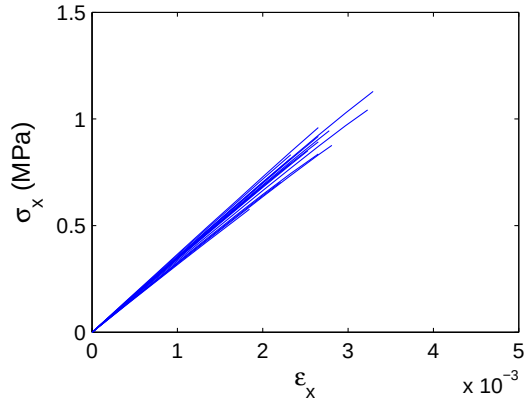

(d) Random, Length=51mm

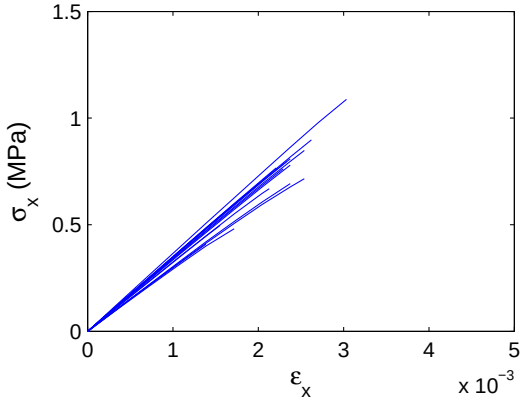

(e) Actual, Length=76mm

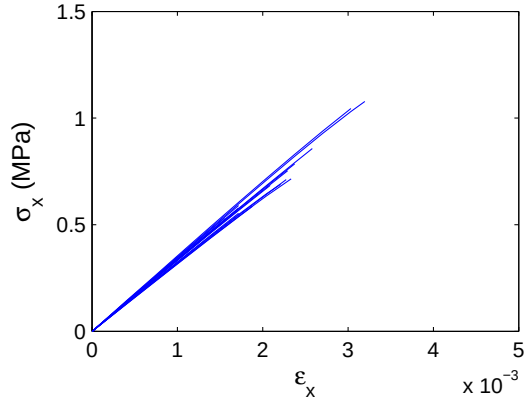

(f) Random, Length=76mm

Figure 7.6. Comparison of three different sizes of actual and random void models under uniaxial tensile loading in T direction

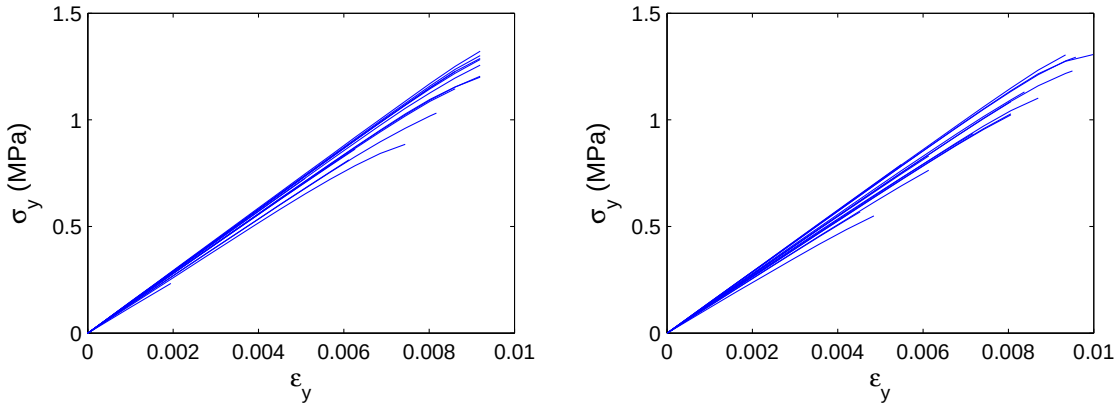

(a) Actual, Length=38mm

(b) Random, Length=38mm

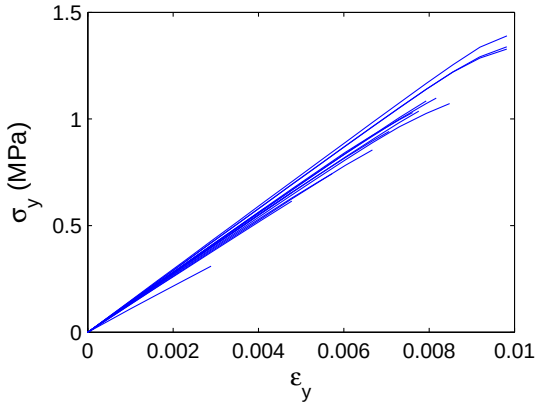

(c) Actual, Length=51mm

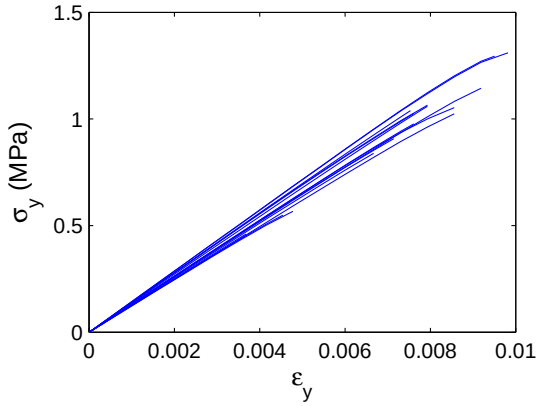

(d) Random, Length=51mm

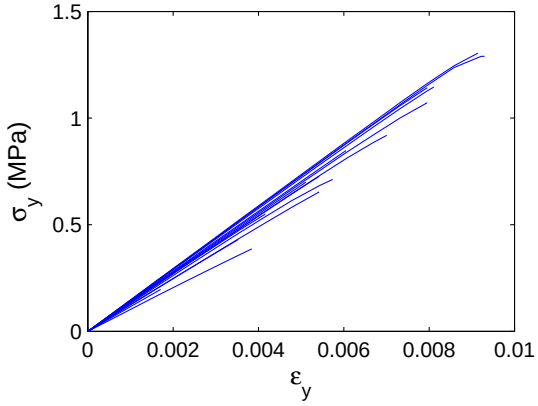

(e) Actual, Length=76mm

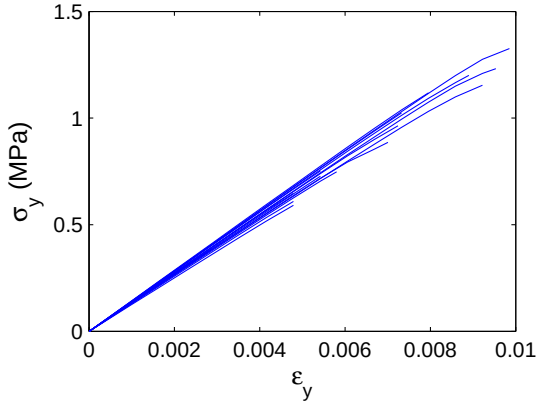

(f) Random, Length=76mm

Figure 7.7. Comparison of three different sizes of actual and random void models under uniaxial tensile loading in TT direction

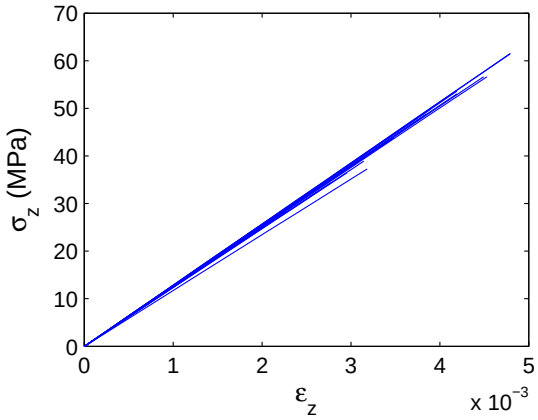

(a) Actual, Length=51mm

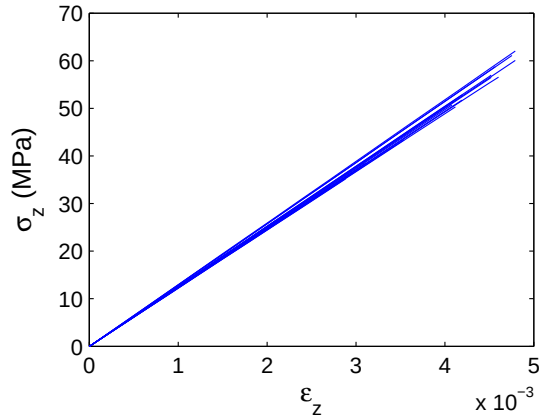

(b) Random, Length=51mm

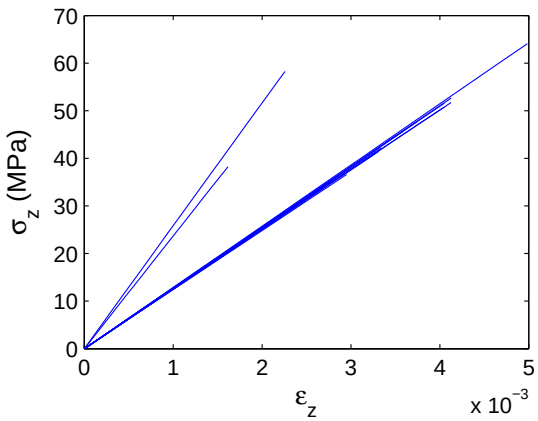

(c) Actual, Length=102mm

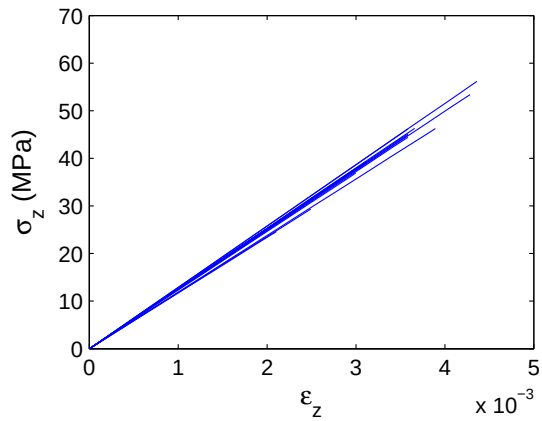

(d) Random, Length=102mm

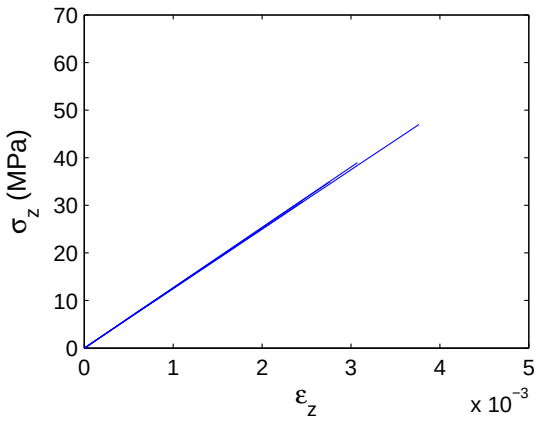

(e) Actual, Length=152mm

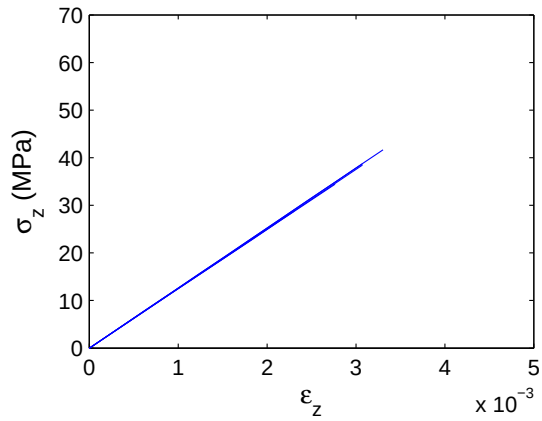

(f) Random, Length=152mm

Figure 7.8. Comparison of three different sizes of actual and random void models under uniaxial tensile loading in L direction

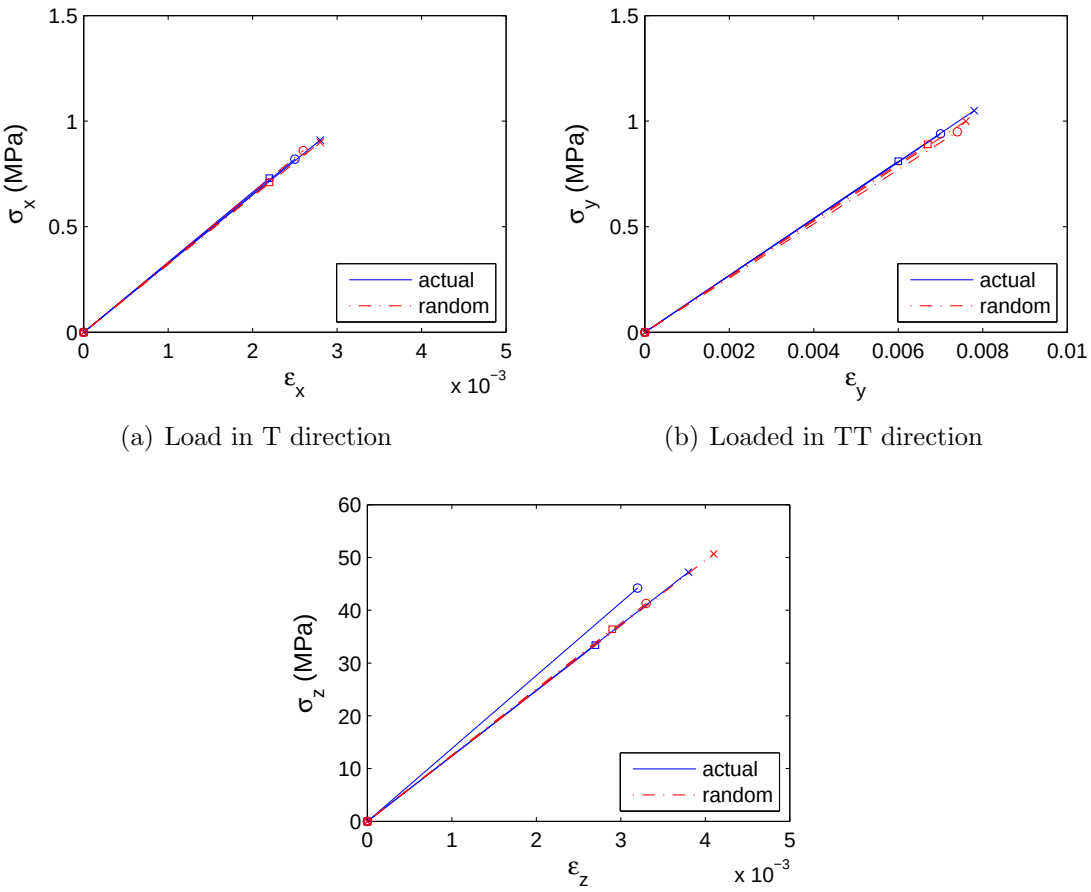

(a) Load in T direction

(b) Loaded in TT direction

(c) Loaded in L direction

Figure 7.9. Effect of size of actual and random void models on uniaxial tensile strength of PSL (×:small size, ○:medium size, □:large size). All stresses and strains are the mean values obtained from Monte Carlo simulations.

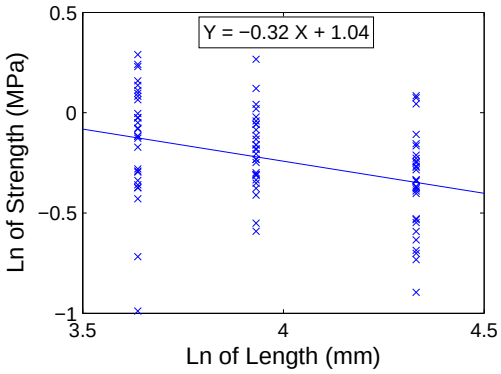

(a) T direction

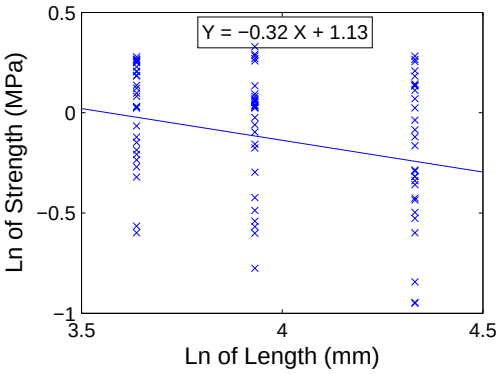

(b) TT direction

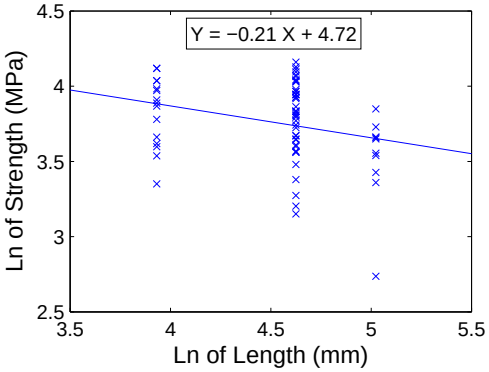

(c) L Direction

Figure 7.10. Size effect in numerical models in different material directions

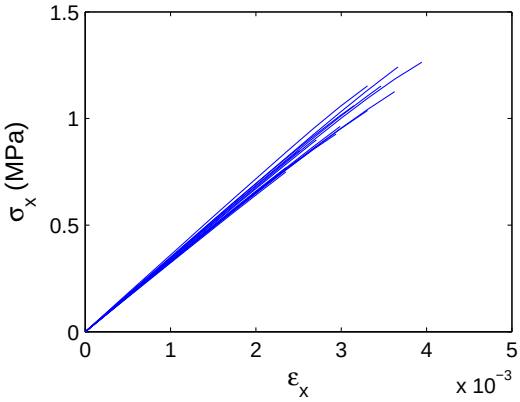

(a) T direction

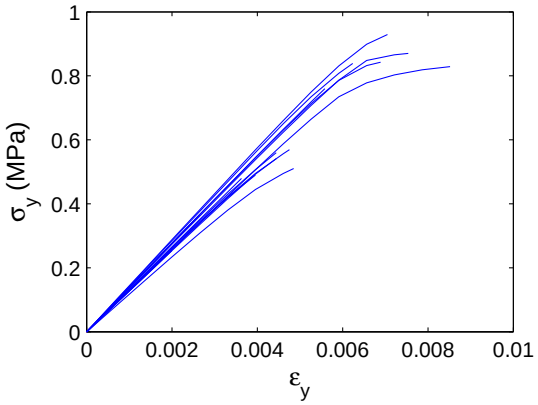

(b) TT direction

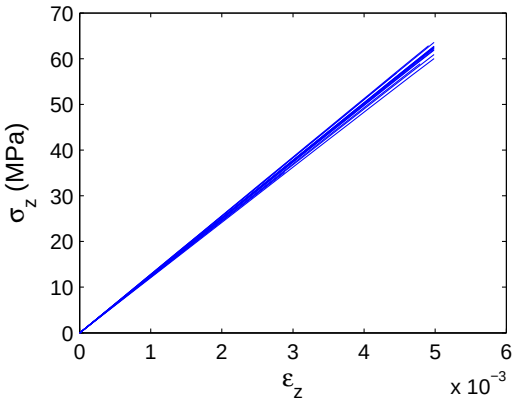

(c) L Direction

Figure 7.11. Stress-strain relationship of calibrated random void models under uniaxial tension

CHAPTER 8

CONCLUSION

The main objective of this dissertation was to characterize and model the mesostructure of 2.0 E Eastern Species Parallel Strand Lumber (PSL). This model is supposed to be used for a more comprehensive goal which is to generate a probabilistic constitutive model for PSL material. The mesostructure of PSL consists of wood strands, adhesive and voids. This project focused just on voids. PSL is both orthotropic and heterogeneous. In addition, even along each material direction, the tensile and compressive behaviors are fundamentally different; the former is brittle and the latter is ductile. These complicated properties make this material difficult to be modeled. Tensile, compressive and shearing behaviors must be investigated for each material direction separately. Also, the influence of sources of uncertainty (i.e. voids, adhesive and strength variability of wood) on the mechanical behavior must be taken into consideration. The compressive and tensile behaviors of this material were investigated in this project, while the shearing behavior was left for future work. The most important conclusions of this study are listed below:

1. This study shows that voids are important sources of uncertainty in mechanical behavior of PSL. With the assumption that the wood phase is continuum, homogeneous and orthotropic and by defining an appropriate void phase, we managed to make numerical models of PSL that, under unaxial loadings in different material directions, have approximately similar statistics of mechanical behavior that experiments have shown. A decent match between mean (and sometimes standard deviation of) mechanical behavior of numerical models and experiments has been obtained by

including models of the voids, and neglecting strand-to-strand variation and other defects. Nevertheless, there was much calibration that had to be done to get the agreement. Therefore, it is hard to conclude that the other sources of uncertainty (especially strand property variation) are unimportant. This characterization study is probably good for the PSL products made of other softwoods, but it may not be transferable to the products of hardwoods, because the void characteristics are highly dependent on density, strand dimensions, and manufacturing variables like pressure and heat.

2. There is no significant stress multiaxiality at the tips of voids (Let us emphasize again that this is under the assumption that grain angle of all strands are the same). This conclusion is important, because PSL is an orthotropic material and stress mutiaxiality could make the behavior of this material even more complicated. Now, understanding and predicting the behavior of this material under different loading scenarios are easier.

3. Voids' shape is much more influential on PSL's tensile brittle behavior than on its compressive ductile behavior. Under the compressive loading, ellipsoidal voids can represent actual voids to ease the simulation. But the actual shapes of voids should be maintained to simulate the brittle behavior of material under tension.

4. In case that the simulation of mesostructure of PSL is of interest, this dissertation has presented good methods for the modeling of voids and appropriate mechanical properties for the assumed continuum homogeneous wood phase. As stated before, a PSL model including continuum wood with calibrated mechanical properties and a properly characterized void set can acceptably simulate the mean mechanical behavior of real material. For the compressive simulation, ellipsoidal voids can replace actual void shapes to ease the simulation. One can generate a set of virtual ellipsoidal voids following the geometrical distributions of actual voids presented in section 2.3 and make PSL models with any size. For the tensile simulation, the actual shape of

voids should be used. The easiest way is to make a library of the geometrical characteristics of actual voids, select the voids randomly from the library and put them in random locations in the model. The details of this method have been explained in section 7.3. If the proposed methods for void representation are employed, the calibrated material properties introduced in Tables 6.1 and 7.7 will be applicable for the continuum wood phase.

5. Most of the voids are considerably small with respect to the size of PSL structural members. Therefore, modeling the mesostructure of PSL for a real member size is very expensive (more than 200000 finite elements were used to model the mesostructure of a 25×25×76 mm PSL specimen). Consequently, it is not practical to model the mesostructure of PSL when a large structural PSL member is simulated. Instead, PSL member should be considered continuum with this condition that the statistical properties of PSL material (mean, standard deviation and correlation coefficient of all mechanical properties) are applied as input. There is experimental statistical data generated by Winans [6, 7], Krupka [38, 21] and Amini (section 4.2 of this dissertation) available for such simulation. The data includes means and standard deviations of compressive yield stresses, tensile strengths and moduli of elasticity in different material directions of Eastern Species PSL. Note that the spatial variation of material properties in a large model has not yet been investigated.

CHAPTER 9

FUTURE RESEARCH

The subject of this research is broad enough to offer many other topics to be studied. Some important topics that can complete this research are listed below:

1. As mentioned in the conclusions, to scale up this work to a commercial product and model a large PSL member, the spatial variation of average material properties must be known. In other words, we should investigate whether the different points in a PSL member have correlated material properties; and if so, how we can introduce this correlation to models. Of course, one should also be very careful with finite elements' size and size effect. The size effect study presented in section 7.5 will be helpful for this purpose.

2. The probabilistic constitutive properties proposed in this study are for uniaxial tension and compression. But they can also be used for pure bending. The material properties in the finite element software should be defined in such a way that when each element is under either tension or compression, it obeys the appropriate constitutive model. A code should be developed to define such constitutive model for commercial software.

3. Regarding material heterogeneity, the focus of this research was on voids. The other important source of heterogeneity is the mechanical property variation of the wood phase. The strength and stiffness of wood strands may vary from point to point due to grain angle variation and wood heterogeneity, and this fact should be taken into consideration in constitutive modeling of PSL. The research done by Clouston on the effect of strand properties variation [18, 22] along with the data presented in

this study about void characterization (section2.3) could form a good baseline for a more complete study of PSL heterogeneity.

4. One important issue which was not investigated in this project is buckling. What if the buckling load of PSL (for a certain specimen/model size) is less than the yielding load? Of course, no sign of buckling was seen or detected in the experiments, and also, a short analytical study in section 4.4 showed that buckling was unlikely in our models. But since buckling is really of potential importance and it may be sensitive to the mesostructure (especially voids), it is worth to make some effort to discover the details about the buckling behavior of PSL in meso scale.

5. To complete the constitutive modeling of PSL, it is required to investigate the probabilistic shearing behavior of material. For sure the material orthotropy and heterogeneity affect the shearing behavior. Yang [54] has recently conducted an experimental research to find the statistics of PSL's torsional properties. These results are very useful for the verification and calibration of numerical PSL models under shear or torsional loadings.

BIBLIOGRAPHY

[1] "ADINA Structures-Theory and Modeling Guide, 3.4: Isothermal plasticity material models", ADINA R&D, Inc.

[2] "ADINA Structures-Theory and Modeling Guide, 11.5: Element death upon rupture", ADINA R&D, Inc.

[3] "LVL in North America: the decade ahead", Leonard Guss Associates, Forest Products Industry Research, 2010.

[4] "Wood handbook: Wood as an engineering material", Forest Products Laboratory, U.S. Department of Agriculture, Madison, Wis., 1999.

[5] Adair C., McKeever D.B., "2006: wood products used in new residential construction in U.S. and Canada,with comparisons to 1995, 1998 and 2003", The Engineered Wood Association, 2009.

[6] Arwade S.R., Clouston P.L., Winans R., "Measurement and stochastic computational modeling of the elastic properties of parallel strand lumber", Journal of Engineering Mechanics, 135(9) : 897-905, 2009.

[7] Arwade S.R., Winans R., Clouston P.L., "Variability of compressive strength of parallel strand lumber", Journal of Engineering Mechanics, 136(4) : 405-412, 2010.

[8] Arwade S.R., "Translation vectors with non-identically distributed components", Probabilistic Engineering Mechanics, 20:158-167, 2005.

[9] Barret J.D., Lam F., Lau W., "Size effects in visually graded softwood structural lumber", Journal of Materials in Civil Engineering, 7(1):19-30, 1995.

[10] Bejo L., Lang E.M., "Simulation based modeling of the elastic properties of structural composite lumber", Wood and Fiber Science, 36(3): 395-410, 2004.

[11] Bentz D.P., Garboczi E.J., Snyder K.A., "A hard-core/soft-shell microstructural model for studying percolation and transport in three dimensional composite media", Technical Report NISTIR 6265, National Institute of Science and Technology, 1999.

[12] Bullard J.W., Garboczi E.J., "A model investigation of the influence of particle shape on Portland cement hydration", Cement and Concrete Research, 36: 1007-1015, 2006.

[13] Bystrzycki J., Perzetakiewicz W., "3 dimensional reconstruction of annealing twins shape in FCC metals by serial sectioning", Scripta Metallurgica et Materialia, 27: 893-896, 1992.

[14] Chaudhuri C.R., Jana M., Bandopadhyay N.R., "Impedance measurement for microstructure characterization and internal surface estimation of macroporous silicon", Physica Status Solidi, A207(9): 2137-2143, 2010.

[15] Chen W.F., "Plasticity in reinforced concrete", McGraw Hill Book Company, 1982.

[16] Chen W.F., Han D.J., "Plasticity for Structural Engineers", Springer-Verlag, 1988.

[17] Clair B., Despaux G., Chanson B., Thibaut B., "Utilisation de la microscopie acoustique pour l'etude des proprietes locales du bois: etude preliminaire de parametres experimentaux", Annals of Forest Science, 57: 335-343, 2000.

[18] Clouston P.L., Lam F., "Computational modeling of strand-based wood composites", Journal of Engineering Mechanics,127(8): 844-851, 2001.

[19] Clouston P.L., "Characterization and strength modeling of parallel strand lumber", Holzforschung, 61: 392-399, 2006.

[20] Clouston P., Liu S., "Predicting the influence of macro-void distribution in parallel wood strand composites", World Conference of Timber Engineering, Portland, Oregon, 2006.

[21] Clouston P.L., Arwade S.R., Krupka M.T., Rattanaserikiat S., Amini A., "Microstructure and size effect in structural composite lumber", Proceedings of 2011 NSF Engineering Research and Innovation Conference, Atlanta, Georgia.

[22] Clouston P.L., Lam F., "A stochastic plasticity approach to strength modeling of strand-based wood composites", Composites Science And Technology, 62(10-11):1381-1395, 2002.

[23] Cramer M., Sevostianov I., "Effect of pore distribution on elastic stiffness and fracture toughness of porous materials", International Journal of Fracture, 160: 189-196, 2009.

[24] Ellis S., Dubois J., Avramidis S., "Determination of Parallam ®macroporosity by two optical techniques", Wood and Fiber Science, 26: 70-77, 1994.

[25] Garboczi E.J., "Three-dimensional mathematical analysis of particle shape using X-ray tomography and spherical harmonics: application to aggregates used in concrete", Cement and Concrete Research, 32: 16211638, 2002.

[26] Ghadbeigi H., Pinna C., Celloto S., Yates J.R., "Local plastic strain evolution in a high strength dual-phase steel", Materials Science and Engineering, A527: 5026-5032, 2010.

[27] Gonella S., Greene M.S., Liu W.K., "Characterization of heterogeneous solids via wave methods in computational microelasticity", Journal of Mechanics and Physics of Solids, 59: 959-974, 2011.

[28] Graham L., Gurely K., Masters F., Baxter S., "Analysis of random composite materials using non-Gaussian simulation", Proceedings of the Fourth International Conference on Computational Stochastic Mechanics, Greece 2002: 225-234.

[29] Grigoriu M., Garboczi E., Kafali C., "Spherical harmonic-based random fields for aggregates used in concrete", Powder Technology, 166: 123138, 2006.

[30] Gupta R., Siller T.S., "Stress distribution in structural composite lumber under torsion", Forest Product Journal, 55(2):51-56, 2005.

[31] Hibbeler R.C., "Mechanics of Materials, 3.3: StressStrain Behavior of Ductile and Brittle Materials", Prentice Hall, Ed. 8, 2011.

[32] Ishikawa M., Yoshikawa H., Tanabe T., "The constitutive model in terms of damage tensor", Proceeding, Finite Element Analysis of Reinforced Concrete Structures, ASCE, Reston, Virginia 1986, 93-104.

[33] Janowiak J.J., Hindman D.P., Manbeck H.B., "Orthotropic behavior of lumber composite materials", Wood and Fiber Science, 33(4): 580-594, 2001.

[34] Jennings H.M., Bullard J.W., Thomas J.J., Andrade J.E., Chen J.J., Scherer G.W., "Characterization and modeling of pores and surfaces in cement paste: correlations to processing and properties", Journal of Advanced Concrete Technology, 6(1): 5-29, 2008.

[35] Jones R.M., "Mechanics of composite materials", Scripta Book Co., Washington D.C., 1975.

[36] Knauss D., Bennink D.D., Martin J.W., Briggs J.A.D., Zhai T., "Three dimensional measurement of short fatigue cracks using scanning acoustic microscopy", Materials Science and Technology, 9: 1086-1093, 1993.

[37] Labeas G., Kermanidis T., "Stress multiaxiality factor for crack growth prediction using the strain energy density theory", Theoretical and Applied Fracture Mechanics, 45: 100-107, 2006.

[38] Krupka MT, Arwade SR, Clouston PL, "Length effects in tensile strength in the orthogonal directions of structural composite lumber" Journal of Testing and Evaluation vol. 39: DOI: 10.1520/JTE10326119.

[39] Madsen B., Tomoi M.,"Size effects occurring in defect-free spruce pine fir bending specimens", Canadian Journal of Civil Engineering, 18(4):637-643, 1991.

[40] Matzke H.J., Warren R., "Hertzian crack growth in ThO2 observed by serial sectioning", Journal of Materials Science, 1:441-444, 1982.

[41] Mindlin R.D., "Microstructure in linear elasticity", Archive for Rational Mechanics and Analysis, 16(1): 51-78, 1964.

[42] Qing H., Mishnaevsky L., "Moisture-related mechanical properties of softwood: 3D micromechanical model", Computational Materials Science, 46: 310-320, 2009.

[43] Sadd M.H., Dai Q., Parameswaran V., Shukla A., "Microstructural simulation of asphalt materials: modeling and experimental studies", Journal of Materials in Civil Engineering, 16(2): 107-115, 2004.

[44] Sedighi-Gilani M., Navi P., "Micromechanical approach to wood fracture by three dimensional mixed lattice-continuum model at fiber level", Wood Science and Technology, 41: 619-634, 2007.

[45] Sugimori M., Lam F.,"Macro-void distribution analysis in strand-based wood composites using an X-ray computer tomography technique", Journal of Wood Science, 45(3): 254-257, 1999.

[46] Tashman L., Wang L., Thyagarajan S., "Microstructure characterization for modeling HMA behavior using imaging technology", Models and Methods for Bituminous Materials, 8: 207-238, 2008.

[47] Torquato S., "Random heterogeneous materials: microstructure and macroscopic properties", Springer-Verlag, New York, 2002.

[48] Triche M.H., Hunt M.O., "Modeling of parallel-alligned wood strand composites", Forest Products Journal, 43(11-12):33-44, 1993.

[49] Vasic S., Smith I., Landis E., "Finite element techniques and models for wood fracture mechanics", Wood Science and Technology, 39: 3-17, 2005.

[50] Wang Y.T., Lam F. "Computational modeling of material failure for parallel-aligned strand based wood composites", computational Material Science, 11(3):157165, 1998.

[51] Weib S., Schnauber T., Fischer A., "Microstructure characterization of thin structures after deformation", Material and Devices for Smart Systems Symposium, Boston 2008, 1129-V11-19.

[52] Wu Q., Lee J.N., Han G., "The influence of voids on the engineering constants of oriented strand board: a finite element model", Wood and Fiber Science, 36: 71-83, 2004.

[53] Wu Q., Zhang B., Han G., "The application of 3D x-ray tomography with finite element analysis for engineering properties of strand-based composites", Proceedings of the 8th Pacific Rim Bio-Based Composites Symposium, 2006.

[54] Yang, Z., "Torsional Shear Strength and Size Effect in Structural Composite Lumber", M.S. Thesis, Department of Environmental Conservation, University of Massachusetts Amherst, 2012.

[55] Ye G., Hu J., van Breugel K., Stroven P., "Characterization of the development of microstructure and porosity of cement-based materials by numerical simulation and ESEM image analysis", Materials and Structures, 35: 603-613, 2002.